RESEARCH ON FAST FEM SIMULATION OF RF SAW/BAW DEVICES USING HIERARCHICAL CASCADING TECHNIQUE

階層的縦続法に基づく高周波 SAW/BAW デバイスの高速有限要素解析に関する研究

2019 年 7 月

千葉大学大学院工学研究科
人工システム科学専攻電気電子系コース

李 昕熠

（千葉大学審査学位論文）

RESEARCH ON FAST FEM SIMULATION OF RF SAW/BAW DEVICES USING HIERARCHICAL CASCADING TECHNIQUE

階層的縦続法に基づく高周波 SAW/BAW デバイスの高速有限要素解析に関する研究

2019 年 7 月

千葉大学大学院工学研究科
人工システム科学専攻電気電子系コース

李 昕熠

Ph.D. thesis submitted in partial fulfillment of the requirements for the degree of Ph.D. in Science, Graduate School of Chiba University, Japan.

Affiliation:

Graduate School of Engineering

Department of Electrical and Electronic Engineering

Chiba University

1-33 Yayoi-cho, Inage-ku, Chiba-shi 263-8522 Japan

Supervisor:

Prof. Ken-ya Hashimoto, Dep. Elec. and Electronic Engineering, Graduate School of Engineering, Chiba University

Examiners:

Prof. Ken-ya Hashimoto, Dep. Elec. and Electronic Engineering, Graduate School of Engineering, Chiba University

Prof. Toshiaki Takano, Dep. Elec. and Electronic Engineering, Graduate School of Engineering, Chiba University

Prof. Kazuhiro Kudo, Dep. Elec. and Electronic Engineering, Graduate School of Engineering, Chiba University

Prof. Tatsuya Omori, Dep. Elec. and Electronic Engineering, Graduate School of Engineering, Chiba University

DECLARATION

I hereby declare that this submission is my own work and that, to the best of my knowledge and belief, it contains no material which to a substantial extent has been accepted for the award of any other degree or diploma of the university or other institute of higher learning, except where due acknowledgment has been made in the text.

Xinyi Li, Chiba, June 2019

ACKNOWLEDGEMENT

This thesis was prepared during my 3-year stay in the Electro-Communications Laboratory of Chiba University. I would like to express my gratitude to those who help me in the Ph. D. period.

First, I would like to extend my utmost gratitude to my supervisor, Professor Ken-ya Hashimoto, who has offered me valuable suggestions in my academic studies. His incisive comments and constructive criticism helped me to solve the countless problems in my research. I do appreciate his patience, encouragement, and professional instructions for both my academic work and daily life. It is my great honor to be a member of his dynamic and diligent team. The academic rigor that he always insists will engrave in my mind forever. Also, I will cherish the memory of the beautiful melody in his office.

I also would like to sincerely thank Prof. Jingfu Bao of University of Electronic Science and Technology of China (UESTC), who provided me the opportunity to join the double Ph. D. degrees program between UESTC and Chiba University. He is my first mentor in micro-electro-mechanical system and always encourages me to broaden my vision. I really appreciate the encouragement he gave which boosts my motivation.

The work in this thesis is done on the basis of the hierarchical cascading theory proposed by Julius Koskela and Vector Plessky. Their published researches enlighten me a lot, and catching up with their progress is one of my motive power during the Ph.D. period. I much express my great respects to them.

I gratefully acknowledge the scholarship received from Ministry of Education, Culture, Sports, Science and Technology (MEXT) of Japanese government, which supported me during the whole doctoral program. I cannot put my heart and soul into scientific research without it. I do enjoy the three-years' quiet and comfortable life in Japan. Polite and friendly Japanese people impress me a lot.

The efforts for reviewing the dissertation by Prof. Toshiaki Takano, Prof. Kazuhiro Kudo, Prof. Tatsuya Omori are appreciated. I am also grateful to Prof. Tatsuya Omori, and Prof. Hao Liu for the rich knowledge I got from their lectures. Thanks should be given to Mrs. Hideko Tamura for her kind help, support and celebrating my birthday every year.

I appreciate all the friends in the Electro-Communications Laboratory of Chiba University. They are Yulin Huang, Benfeng Zhang, Gongbin Tang, Luyan Qiu, and Naoto Matsuoka. I will remember the days and nights we spend in the office together. I miss the fruitful discussion we had together.

Last but not least, I would like to express my deepest appreciation to my family. This dissertation would not have been possible without their warm love, continued patience, and endless support. I want to express my gratitude with love to Yaqi Ji, my darling wife. I married the best person out there for me. Her companion in all these years has made them the most precious years of my life. Finally, my dear son, Yanye Li (Ken-ya Li in Japanese), you are my most precious gift. I hope you grow up healthily and be as erudite and noble as Prof. Hashimoto.

ABSTRACT

Fast and accurate simulation methods are strongly demanded to reduce the cost of developing high-performance surface and bulk acoustic wave (SAW/BAW) devices. This thesis deals with the development of fast and accurate simulation techniques for RF SAW/BAW devices. They are based on the hierarchical cascading technique (HCT) proposed recently, and several extensions are proposed for its skillful use in addition to further speed up and memory saving. The extended HCT is applied to various acoustic problems, and its effectiveness is demonstrated.

First, the basic algorithm of the overall process of HCT is discussed step by step. Relating matrix operations are presented in detail. It is demonstrated that extremely huge FEM model with periodic units can be assembled and solved at a fast speed. It is also shown that HCT is quite effective for the structural design using the parameter sweep because a small portion of the FEM model is changed while the remaining portion is unchanged. Mirror cascading method is proposed to accelerate the HCT when the structure under concern possesses symmetry. It halves the time consumption and memory usage compared with the traditional HCT. After the introduction, behaviors of SAW resonators are analyzed by the HCT as a demonstration.

Next, HCT is applied to obtain a unique kind of energy-absorbing boundary condition called infinite long damping boundary (ILDB). The perfect matching layer (PML) giving the same functionality is widely used, but it does not work properly when one of the wave components possesses negative group velocity. In contrast, ILDB works properly anytime. As a trade-off, execution times become long. HCT and ILDB are implemented into traveling-wave excitation sources model for scattering analysis at side edges of both BAW and SAW devices. It is shown that both execution time and memory consumption of HCT are much less than those of full FEM analysis. Owing to the developed HCT implemented traveling wave source(TWS) model, the computation time shrinks from days to less than 1 hour for designing the optimal side edge structure in SAW devices. Furthermore, scattering caused by the discontinuity between two periodic gratings in the longitudinal direction is also investigated.

Finally, HCT is implemented into 3D FEM simulation for practical SAW devices. The general-purpose graphics processing units (GPGPU) is introduced to accelerate matrix processing. With the help of GPGPU, extremely large full 3D SAW model can be simulated at a surprising speed. Acceleration more than ten times is achievable. The obtained electrical frequency response includes all kinds of effects in the SAW device. Moreover, the acquired displacement field is quite helpful in diagnosing spurious responses and scattering in real SAW device structures.

階層的縦続法に基づく高周波**SAW/BAW**デバイスの高速有限要素解析に関する研究

概要

本論文では、近年提案された階層的縦続法(HCT)を基にして、高周波SAW/BAW デバイスの有限要素法(FEM)解析に対する様々な高速化並びに高機能化手法を提案し、その有効性を明らかにしている。

まず、HCTの基本的な流れを解説すると共に、基本構造が鏡像対称を含む場合に有効な新たな縦続手法を提案している。また、素子設計の場で頻繁に遭遇する、構造の大部分は変わらず、構造の一部変更と特性変化の関係を調べる場合等に、HCTが極めて有効であることを示している。

次に、HCTを利用した吸収境界条件を提案している。これは僅かな損失を持つ微小セルを数多く縦続することで、無反射吸収端を実現するもので、どの様な材料構造でも完全な吸収特性を保証する。これと筆者が提案している進行波励振源を組み合わせることにより、SAW/BAW素子における構造端部での散乱特性解析に適用し、この手法がSAW/BAW素子構造の設計に対して如何に有効であるかを明らかにしている。また、吸収境界条件と進行波励振源を利用して、2つの非常に長い周期的構造に挟まれた不連続部における散乱特性の解析にも成功している。

最後に、HCTにおける行列演算を汎用グラフィック処理装置(GPGPU)で実行させることにより、1000万以上の自由度を持つ非常に大規模のSAW素子の

フル3次元FEMが、周波数一点当たり2分程度という短時間で実行可能であることを示している。さらに、計算結果を利用したSAW素子における不要応答発生機構の解析手法についても述べている。

Contents

List of Figures

List of Tables

Chapter 1

Introduction

1.1 Background

Nowadays, wireless communication is replacing fixed-line services as the most popular way for people to access the Internet. There are more than 7.9 billion mobile subscriptions in the world until 2018 [1]. It is expected that the market will keep increasing rapidly as the Fifth-Generation (5G) wireless technology is arriving [2, 3]. Filters have become a significant part in the radio frequency (RF) front-end system due to the spectrum fragmentation [4]. More than 60 filters are installed in one state of the art smart phones supporting 30 bands [5], while more new bands for 5G is on the way. The vast majority of these filters in hand-held wireless devices are acoustic filters based on the piezoelectric effect [6]. Since acoustic wave owns a velocity five orders smaller than the speed of the electromagnetic wave, its typical wavelength at GHz range is in the order of μm. Thus, high quality factor (Q) filters can be packaged in a small size [7].

There are two basic types of acoustic waves applied in piezoelectric devices: surface acoustic wave (SAW) and bulk acoustic wave (BAW). In 1885, Lord Rayleigh firstly described SAW in solids in theory [8], which is now well-known as Rayleigh wave. In 1965, 80 years after SAW proposed, R. M. White and F. W. Voltmer successfully generated and detected SAW in a piezoelectric substrate with an interdigital transducer (IDT) [9]. From then on, SAW devices went into a rapid development and applied in various fields [10–13].

Figure 1.1 shows the typical structure of a SAW resonator. Lithium niobate ($LiNbO_3$, LN) [14, 15], lithium tantalate ($LiTaO_3$, LT) [16], and quartz [17] are common materials for the substrate. The metal layer on the piezoelectric substrate is prepared and patter-

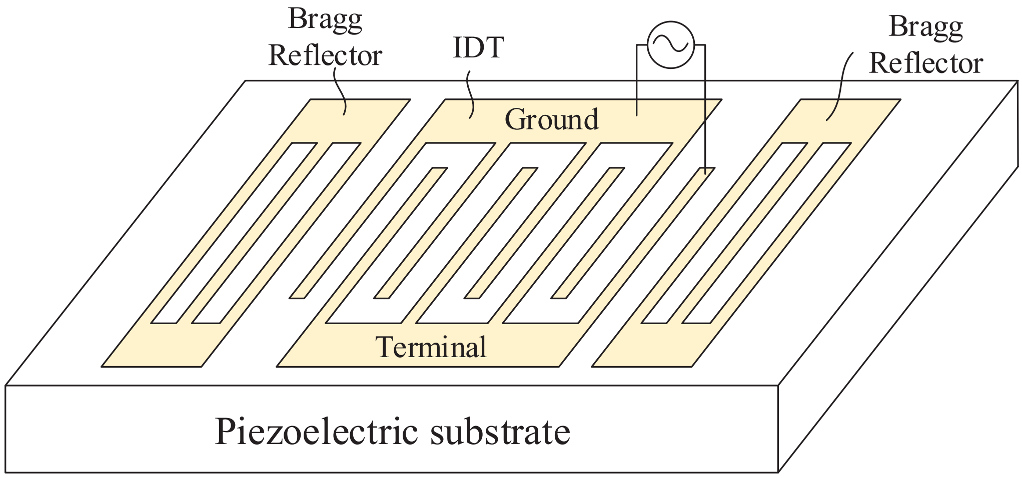

Figure 1.1: Typical structure of SAW resonator.

ned into gratings. SAW is excited by the central IDT, and two Bragg reflectors confine the energy from lateral dissipating.

Comparing with SAW, RF application of BAW devices based on the piezoelectric thin film started late. Three research groups of Lakin [18], Nakamura [19], and Grudkowski [20] published their papers on fabricated BAW devices using Zinc Oxide (ZnO) almost simultaneously in 1980. Later, the development of BAW devices separated into two technical routes: film bulk acoustic resonator (FBAR) [21–23] and solidly mounted resonators (SMR) [24–26]. Their typical structures are shown in Figure 1.2. Both of them operate in the thickness extensional (TE1) mode. At present, Aluminum Nitride (AlN) has replaced ZnO as the piezoelectric material in all commercial BAW devices, due to its perfect balance in performance and reliable deposition [27–29]. Metal with high acoustic impedance and low resistivity, such as ruthenium (Ru) and molybdenum (Mo), are suitable for electrodes [30,31]. The major difference between FBAR and SMR is the way of reflecting acoustic energy from the bottom. The free surface is selected in FBAR, while SMR uses the Bragg reflector (alternating layers of materials with high and low acoustic impedances). Since the acoustic wave can be better reflected by the interface between metal and air than the Bragg reflector, the FBAR establishes higher Q factor than SMR. Meanwhile, BAW resonators own advantages in energy loss than SAW resonators due to the same reason.

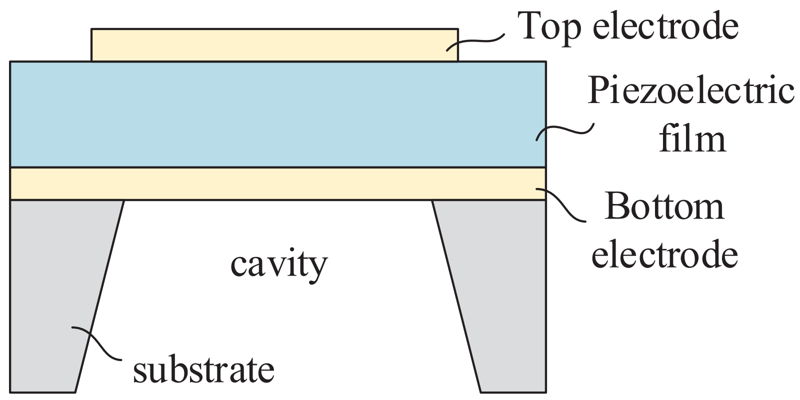

(a)

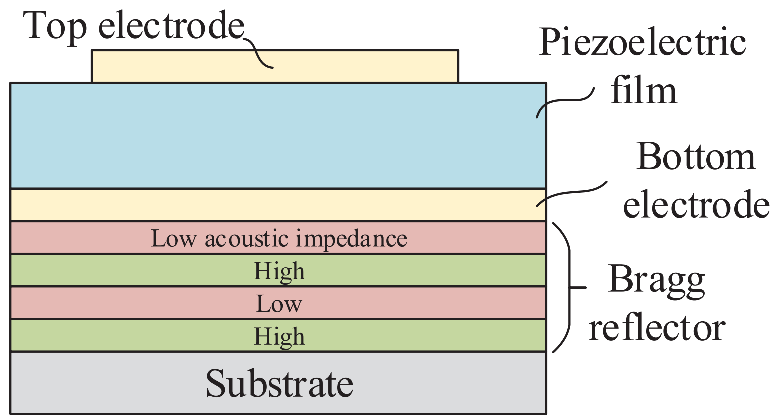

(b)

Figure 1.2: Typical structures of BAW devices (a) FBAR (b) SMR.

To satisfy the developing high demands of modern communication system, the performance of SAW/BAW filters are required to be enhanced every year. Innumerable researchers in SAW/BAW society have proposed and is still looking for novel ideas to improve the performance of SAW/BAW filters [32, 33]. As the fundamental unit in the filter, an ideal resonator based on both SAW and BAW should satisfy the following requirements:

a) High Q factor;

b) Weak spurious responses;

c) Large coupling coefficient;

d) Large power durability;

e) Weak nonlinearity;

f) Good thermal stability;

g) Small in size, weight and price.

The Q decides the filter's insertion loss (IL) in the passband and the steepness of skirt [34, 35]. The definition of Q value is expressed as [36]:

$$Q = 2\pi \frac{E_{\text{stored}}}{E_{\text{loss}}}, \tag{1.1}$$

where E_{stored} is the total stored energy in the resonator in peak, and E_{loss} is energy dissipated per cycle. Giving all kinds of energy loss mechanisms is known, the total quality factor of the resonator can be expressed as

$$Q_{\text{total}} = \left(\sum \frac{1}{Q_i} \right)^{-1}, \tag{1.2}$$

where $1/Q_i$ corresponds to each loss component. Numerous researches have been published aiming at improving each Q_i.

As to FBAR, since surrounding tether is expected to be its major origin of acoustic losses (Figure 1.3 (a)), structure designs such as just-etched edge [37], thin bottom electrode [38] and raised frame border [39] were proposed. In SAW cases, special layout could be placed in all directions to avoid energy losses in various ways (as shown in Figure 1.3 (b)). An optimized cut angle of LT substrate is found to reduce the leakage to the bottom substrate [16]. Side radiation of leaky waves into the busbars can be restrained by narrowing the gap region [40, 41]. In temperature compensated SAW (TC-SAW), several strategies have been applied to minimize the side radiation [42, 43]. Recently, great progress has been made by the so-called incredible high performance SAW resonator (IHP SAW) proposed by Takai et al. from Murata [44]. Thinned $LiTaO_3$ is bonded on a hard wafer to prevent bulk wave leakage.

It is also known that acoustic waves reflected at the side edges will cause unnecessary resonances called transverse mode resonances (shown in Figure 1.4). Spurious responses occur in the electrical response (see Figure 1.5), and their ultimate suppres-

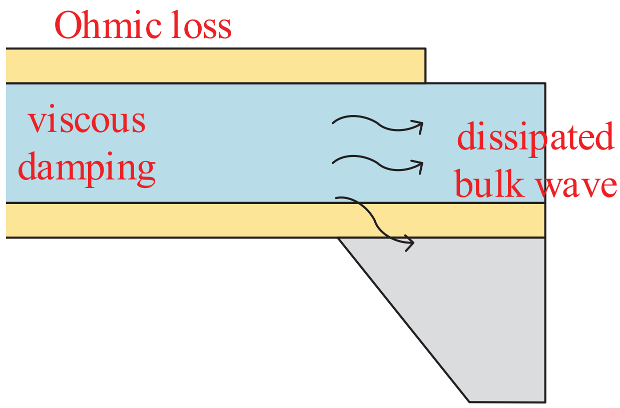

(a)

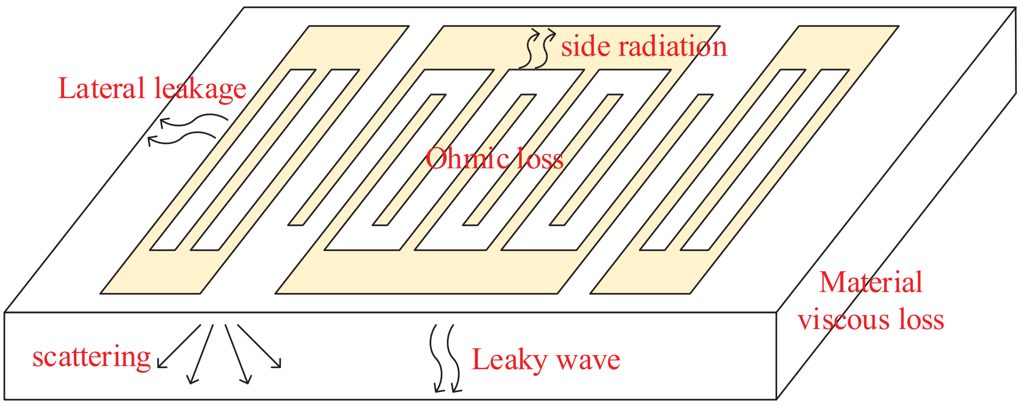

(b)

Figure 1.3: Various loss mechanism in acoustic devices. (a) FBAR, (b) SAW resonator.

sion is also necessary to obtain a flat passband in the filter response. Thus, the design of side edges is critical to realize high-performance SAW/BAW resonators [45, 46].

A famous strategy is the piston mode structure proposed by Kaitila et at., for BAW devices [47]. By adding a fast phase shifting region in the outside of the central active region and giving an appropriate width, the boundaries with the active region will behave as if mechanically free boundaries. This configuration allows only the lowest order TE1 mode (n=0 in Figure 1.6) to be excited, while the other spurious lateral modes (n>0 in Figure 1.6) are neither electrically driven nor sensed in the active region. Although its operating mechanism is explained by the dispersion characteristics of laterally pro-

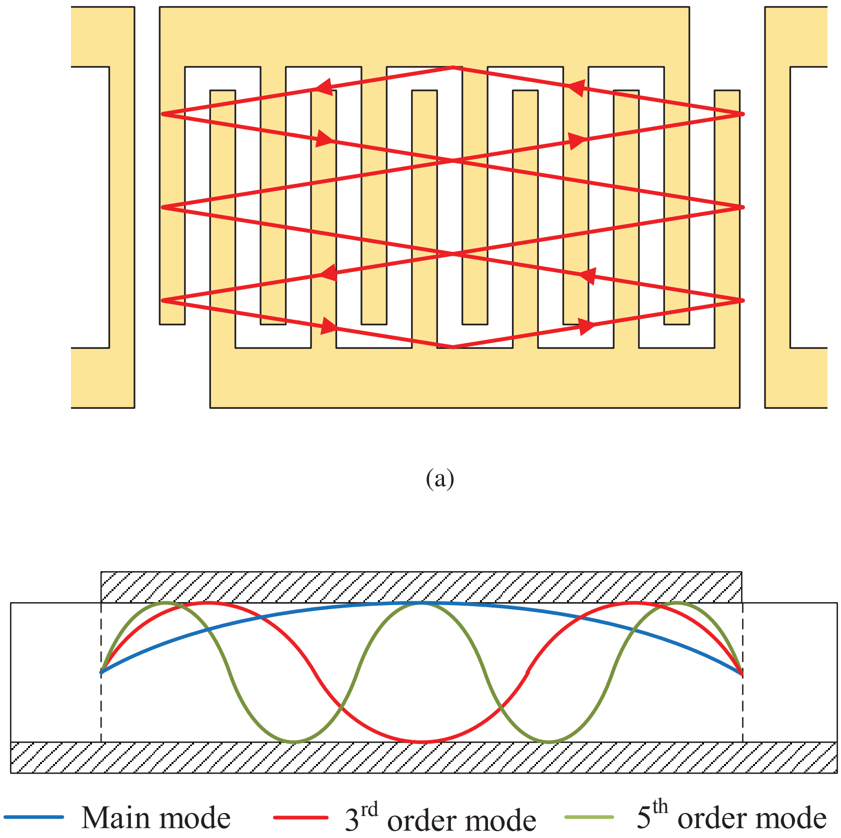

(a)

(b)

Figure 1.4: Modal shapes of transverse modes. (a) SAW resonator, (b) FBAR.

pagating modes, their mode conversion and additional phase shift at the reflection must be taken into account during the implementation of designed side edges to the physical layout. With a delicate design of the border region, suppressed spurious responses and improved Q at the anti-resonant frequency can coexist [48].

Piston mode design is also introduced to SAW devices [49]. Besides, it is interesting that transverse-mode responses in SAW resonators can be suppressed even without the slow region (worked as phase shifter) [50], which is believed indispensable from Kaitila's theory. This phenomenon is explained by the special coupling between multiple SAW modes when the structure is intelligently designed [51,52].

Other methods to suppress spurious responses include apodization in SAW [53] and BAW [54,55], tilted resonator in SAW [56]. However, these kinds of design will worsen

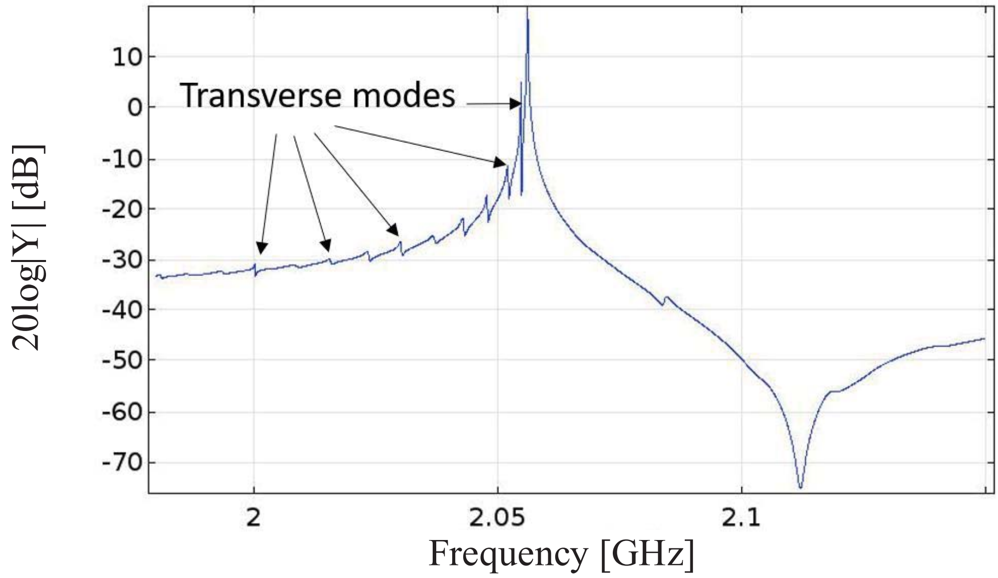

Figure 1.5: Spurious peaks caused by transverse modes in admittance curve of FBAR.

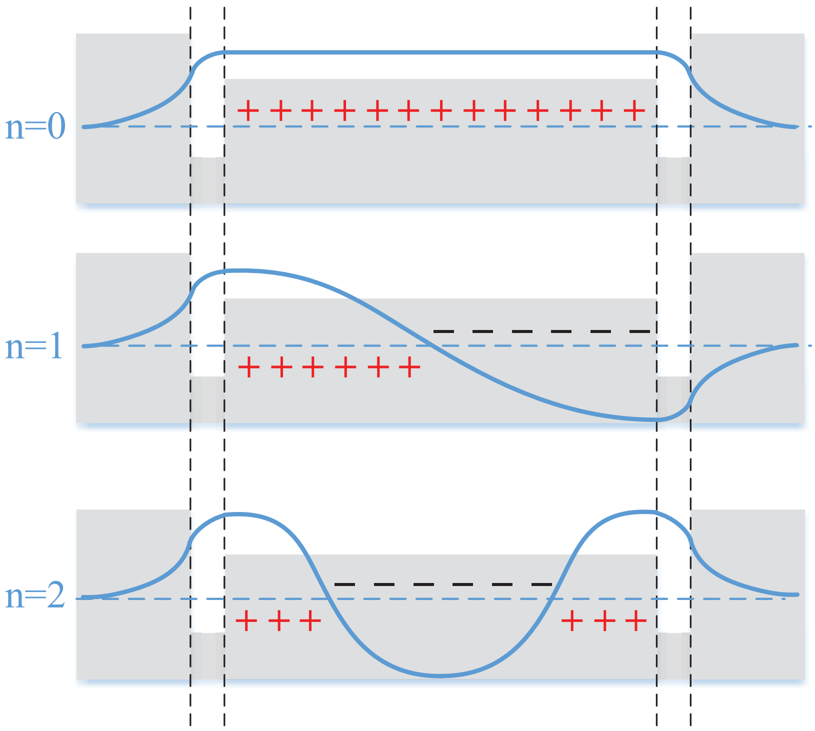

Figure 1.6: Modal shapes of high order modes in piston mode design.

the Q factor at anti-resonance frequency [57].

All these considerations mentioned above makes designing SAW/BAW resonators quite complicated. To avoid wasting time and money in fabricating devices, fast and accurate simulation tools are greatly needed. Behavior models like coupling-of-modes theory [58–60] are widely used for SAW device design. The equivalent circuit for the physical models can be derived by the Mason model [61, 62]. On the other hand, full wave analyses are used for extraction of parameters necessary for behavior models. The finite element method (FEM) [63, 64] and its combination with the spectral domain analysis (SDA) [65] or the boundary element method (BEM) [66] are representatives.

All these tools developed for SAW/BAW simulation are based on certain simplification and assumption. Information in one or two dimensions are lost inevitably and cannot include all kinds of effects in the structure. Even though IHP SAW resonators attained a remarkable performance [44], it is still believed that there is still certain room to enhance the Q factor further. And this further improvement calls for better understanding of the overall acoustic wave leakage.

Because of its simplicity and flexibility, FEM is also widely used for finding optimal structures [67–70]. In 2017, the author's group proposed the traveling wave source (TWS) which bases on the FEM simulation as a straight forward approach for analyzing scattering quantitatively [71]. Its model setting is exhibited in Figure 1.7.

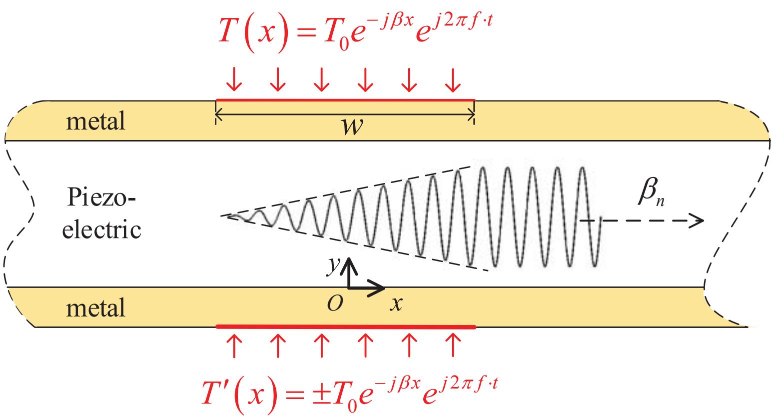

Figure 1.7: Operation principle of TWS in waveguide.

A wave source $T(x)$ is placed to the top surface and is driven by a sinusoidal signal with the frequency f. TWS enables selective excitation of one specific propagating mode. Because of single mode excitation, scattering coefficients at the structural discontinuity under concern can be evaluated directly and accurately from obtained field distribution. Even though it is much easier to implement than the method proposed by Florian, et al. previously [72], further accelerating speed is still required to apply this method for structural optimization through parameter sweep analyses.

Meanwhile, although FEM has a capability to simulate practical three dimensional (3D) SAW/BAW device including all details in the structure [73, 74], its applicability was believed to be limited because of required computing power and memory size.

Another problem in FEM is simulating problems with open boundaries. One possible way is applying a coordinate scaling to a layer of finite domains surrounding. In the Perfectly Matched Layer (PML) [75, 76], a complex coordinate is stretched along a direction. The stretching function requires a predefined typical wavelength λ [77]. Furthermore, the PML will not work properly when multiple acoustic waves with largely different velocities exist simultaneously (multiple λ in different order of magnitude) and/or the group velocity of at least one mode is opposite to its phase velocity (wrong decay direction).

Normalized dispersion relations of Lamb modes in ZnO and AlN plates are shown in Figure 1.8. The branches of first-order symmetric (S1) Lamb mode are marked as red. It is called type II dispersion curve in Figure 1.8(b), where the S1 branch is evanescent at frequencies above the main resonance [47, 78]. The group velocity of S1 wave at the beginning part is opposite to its phase velocity. Meanwhile, A0 Lamb wave has a much shorter wavelength than S1 Lamb wave. Both these two conditions lead to a bad absorbing performance of PML, although Lamb mode characteristics must be understood well in this frequency region for designing FBAR side edges to suppress transverse mode resonances.

SAW resonators include multiple periodic gratings, and sometimes discontinuities are embedded between two gratings (Figure 1.9) for special usage [79,80]. For instance,

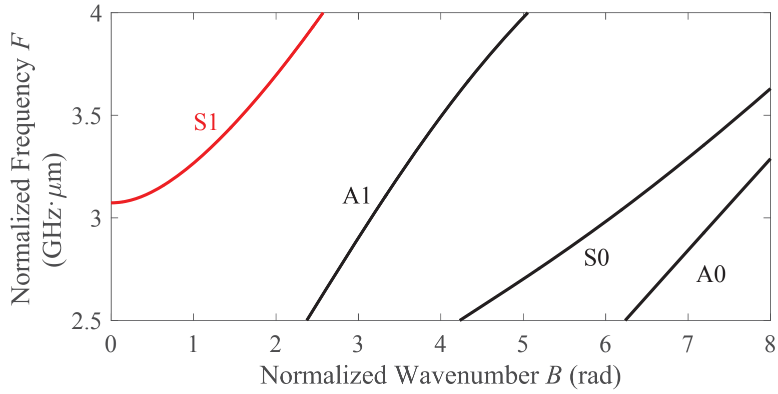

(a)

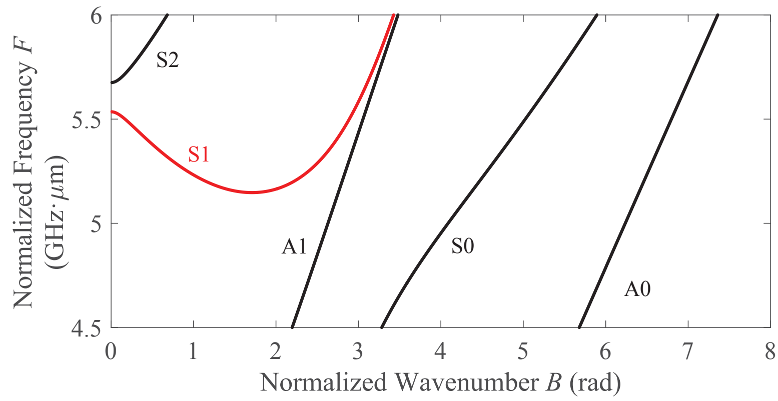

(b)

Figure 1.8: Normalized dispersion relation of Lamb modes in thin plates. (a) type I of ZnO plate, (b) type II of AlN plate.

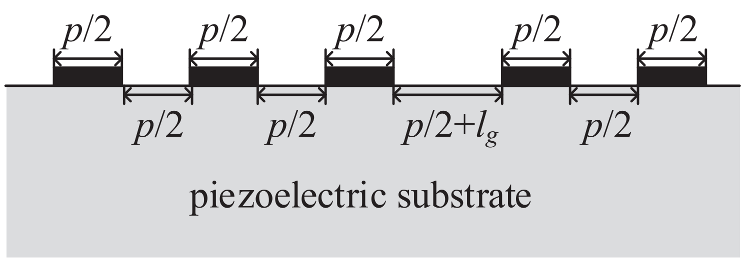

Figure 1.9: Multi-electrode grating structure with discontinuous gap.

it is indispensable in a double mode SAW (DMS) filter [81, 82]. Many researchers paid attention to understand the SAW scattering behaviors at this discontinuities because they may give a significant discrepancy in the electrical response. Even though some progress have been made based on the coupling-of-modes (COM) theory with empirical modification by fitting with experiments [83–85], the strategy is quite uncertain because of lack of its theoretical background. The proposed TWS model provides a potential way to analyze it. But it requires a special absorbing mechanism to avoid new scattering at the interface between the absorbing region and periodic grating.

In 2016, Koskela, et al. proposed the hierarchical cascading technique (HCT) for fast FEM simulation of SAW devices [86]. The similar idea was once published by Hofer, et al. to calculate eigenvalue of wavenumber at a specific frequency [87]. Several unit cells are enough to assemble the whole large FEM model when it is composed of many identical structures as shown in Figure 1.10. The mechanism of HCT will be discussed in details later. It is quite powerful when the device structure under concern is mainly composed of identical cells [88, 89]. Its time consumption is almost in proportion to the logarithm of the number of cell units, while the required memory is almost independent

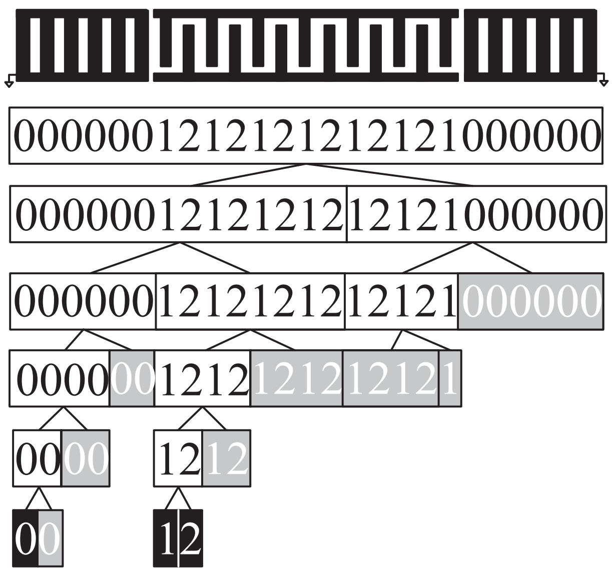

Figure 1.10: Hierarchical cascading tree of a synchronous SAW resonator (cited from Ref. [86]).

of the number of cells. In comparison, the computing time and required memory of conventional FEM are almost proportional to the number of DOFs in the model.

Provided that material constants are accurate enough, the FEM simulation of a full 3D SAW model offers a very accurate electrical response. Solal, et al. verified that 3D FEM simulation of whole SAW device structures is possible by the use of HCT. High accuracy of this simulation result was verified by its comparison with the measured result. Nevertheless, calculation time reported in Ref. 90 was enormous even high-end workstation was used for the calculation.

1.2 Motivation

Based on the background mentioned above, the following problems should be solved to design SAW/BAW devices more efficiently.

1) PML has some disadvantages in simulating SAW/BAW devices in some cases;

2) TWS model is good at quantitative analysis of wave scattering at edges, but its simulation will be quite slow when the frequency is close to the resonance;

3) HCT based FEM simulation is not fast enough for full 3D SAW problems.

1.3 Purpose

In order to solve the problems listed above, this thesis proposes the following solutions.

1) HCT is introduced into constructing energy absorbing boundary condition. The obtained infinite long waveguide with little damping offers better absorbing property than PML as a trade-off with the computational time;

2) HCT is implemented with TWS model. This improved the calculation speed significantly;

3) Mirror cascading method and general-purpose graphics processing unit (GPGPU) are introduced for further acceleration of HCT FEM. The acceleration is significant for large problems, and full 3D SAW simulation becomes practical.

1.4 Organization of This Thesis

This thesis is organized as following:

Chapter 2 starts from basics of the hierarchical cascading algorithm. Various know-hows are also introduced. Next, HCT-FEM simulation is implemented in the platforms of COMSOL and MATLAB. As a demonstration, 2.5D simulation is performed for a SAW synchronous resonator based on the proposed processing flow.

Chapter 3 discusses the implementation of the HCT into the TWS model. An absorbing boundary condition named ILDB is developed using HCT. It is shown that unwanted reflections are suppressed well by the ILDB. HCT based TWS model is applied to analyze various scattering problems related to the FBAR design, and its effectiveness is demonstrated. Then, it is also demonstrated how the combination of HCT and TWS can be used for designing side edges in of SAW devices for the piston mode operation.

Chapter 4 investigates fast simulation of full 3D SAW resonator structure. Use of the GPGPU is proposed for further acceleration of HCT based FEM. It is shown that practical SAW resonator models with 30 million DOFs can be simulated in 2.5 minutes for each frequency point. SAW scattering is also investigated by the wavenumber domain analysis of the calculated field distribution, and its usefulness is also demonstrated.

The conclusion and outlook are drawn in the last Chapter 5.

Chapter 2

Theory of Hierarchical Cascading Technique

2.1 Introduction

Even though the hierarchical cascading technique (HCT) is a tool emerged recently, the HCT has already brought a revolutionary impact on the design of SAW/BAW devices [86, 88, 90–93]. HCT based FEM software called "Layers" was released recently by Plessky's group which proposed HCT. It specializes in simulating any 2D SAW device with many hundreds of electrodes [91]. Meanwhile, there is no doubt that HCT is applicable not only to piezoelectric devices, but also to many other scenarios. For example, optical fiber transmission [94], medical ultrasound imaging [95] and electromagnetic waveguide cavity [96] all include long uniform structures.

This chapter details the overall processes of this significant technique in both algorithm and practical implementation. Some specific modifications are also introduced.

First, all matrix operations related to HCT are presented. The overall process is separated into three steps:

1) Obtaining $\boldsymbol{B}$ matrices from the original FEM matrices where the degrees-of-freedoms (DOFs) remain only in boundaries;

2) Cascading $\boldsymbol{B}$ matrices repeatedly to build the whole structure;

3) Solving out the final equation and tracing back the eliminated inner DOFs.

Next, a special cascading method, mirror cascading, is introduced. When a unit cell possesses mirror symmetry, some relations hold among $\boldsymbol{B}$ matrix elements. This characteristic can accelerate the cascading calculation of symmetrical unit cells.

Then, one feasible practical process flow is presented to realize HCT FEM simulation, using commercial software. It may allow followers to extend and/or enhance the HCT calculation for their own purposes. Finally, the HCT simulation is demonstrated for a 2.5D model of SAW synchronous resonator, following the introduced process flow.

2.2 Basic Algorithm

2.2.1 Derive *B* matrix from FEM equation

The HCT starts from the decomposition of the whole structure into small cells. Meshed 2D FEM model of fundamental cell A in a SAW device is shown in Figure 2.1. It consists of a substrate and an electrode. PML is placed at the bottom. The whole problem domain is subdivided into a number of finite elements (grids in Figure 2.1). DOFs (unknown variables) are located at the nodes (black dots in Figure 2.1). The process of building the FEM equation from constitutive equations (Newton's second law of motion, Maxwell's equation and piezoelectric equation) is not treated here, and they are introduced well in Refs. 97–99.

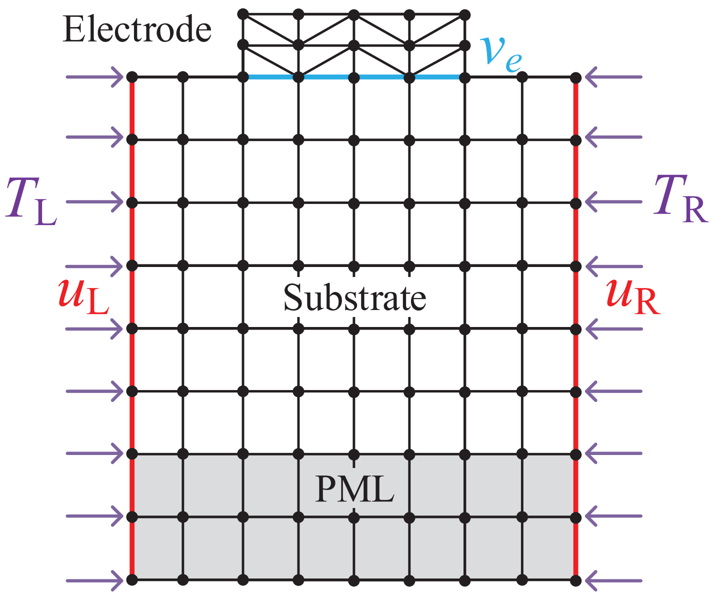

Figure 2.1: A meshed FEM model: unit cell A.

The resulting linear partial differential equation can be expressed as

$$\left(\boldsymbol{K} + i\omega\,\boldsymbol{D} - \omega^2\boldsymbol{M}\right)\boldsymbol{U} = \boldsymbol{L}, \tag{2.1}$$

where $\omega = 2\pi f$ is the angular frequency, $\boldsymbol{K}$, $\boldsymbol{D}$ and $\boldsymbol{M}$ represent the stiffness, damping and mass matrices, respectively, $\boldsymbol{U}$ is the vector of DOFs and $\boldsymbol{L}$ on the right side is the load the vector. In a piezoelectric FEM model, there are two types of DOFs: mechanical displacement variables $\vec{u}$ and electric potential variables ϕ. On the other hands, loads are applied forces F and charges q.

Let us express the linear partial differential equation of a unit cell A as

$$\begin{bmatrix} \boldsymbol{A}_{\mathrm{LL}} & \boldsymbol{A}_{\mathrm{LC}} & \boldsymbol{0} & \boldsymbol{A}_{\mathrm{Le}} \\ \boldsymbol{A}_{\mathrm{CL}} & \boldsymbol{A}_{\mathrm{CC}} & \boldsymbol{A}_{\mathrm{CR}} & \boldsymbol{A}_{\mathrm{Ce}} \\ \boldsymbol{0} & \boldsymbol{A}_{\mathrm{RC}} & \boldsymbol{A}_{\mathrm{RR}} & \boldsymbol{A}_{\mathrm{Re}} \\ \boldsymbol{A}_{\mathrm{eL}} & \boldsymbol{A}_{\mathrm{eC}} & \boldsymbol{A}_{\mathrm{eR}} & \boldsymbol{A}_{\mathrm{ee}} \end{bmatrix} \begin{bmatrix} \boldsymbol{u}_{\mathrm{L}} \\ \boldsymbol{u}_{\mathrm{C}} \\ \boldsymbol{u}_{\mathrm{R}} \\ \boldsymbol{v}_{\mathrm{e}} \end{bmatrix} = \begin{bmatrix} \boldsymbol{T}_{\mathrm{L}} + \boldsymbol{F}_{\mathrm{L}} \\ \boldsymbol{F}_{\mathrm{C}} \\ \boldsymbol{T}_{\mathrm{R}} + \boldsymbol{F}_{\mathrm{R}} \\ -\boldsymbol{q}_{\mathrm{e}} \end{bmatrix}, \tag{2.2}$$

where $\boldsymbol{A}_{ij}$ are sub-matrices of the FEM matrix, the subscripts R, L, e and C indicate values at right and left boundaries (red lines in Figure 2.1), in the electrode (blue line in Figure 2.1) and elsewhere, respectively. $\boldsymbol{T}$ is the stress given from neighboring units. For DOFs located in the interior or on the free boundary, corresponding elements of $\boldsymbol{T}$ should be zero. It is worth to notice that usually $\boldsymbol{F}$ is zero in SAW/BAW models and the voltage applied in electrode should be regarded as the power source. In fact, $\boldsymbol{v}_e$ is a given constant. To make it simple, it is left along with other unknowns for now.

The next is to eliminate the internal DOFs $\boldsymbol{u}_{\mathrm{C}}$ from the equation by establishing the Schur-complement [100], and the following $\boldsymbol{B}$ matrix equation is obtained:

$$\begin{bmatrix} \boldsymbol{B}_{\mathrm{LL}} & \boldsymbol{B}_{\mathrm{LR}} & \boldsymbol{B}_{\mathrm{Le}} \\ \boldsymbol{B}_{\mathrm{RL}} & \boldsymbol{B}_{\mathrm{RR}} & \boldsymbol{B}_{\mathrm{Re}} \\ \boldsymbol{B}_{\mathrm{eL}} & \boldsymbol{B}_{\mathrm{eR}} & \boldsymbol{B}_{\mathrm{ee}} \end{bmatrix} \begin{bmatrix} \boldsymbol{u}_{\mathrm{L}} \\ \boldsymbol{u}_{\mathrm{R}} \\ \boldsymbol{v}_{\mathrm{e}} \end{bmatrix} = \begin{bmatrix} \boldsymbol{F}'_{\mathrm{L}} + \boldsymbol{T}_{\mathrm{L}} \\ \boldsymbol{F}'_{\mathrm{R}} + \boldsymbol{T}_{\mathrm{R}} \\ -\boldsymbol{q}'_{\mathrm{e}} \end{bmatrix}, \tag{2.3}$$

where

$$\boldsymbol{B}_{ij} = \boldsymbol{A}_{ij} - \boldsymbol{A}_{i\mathrm{C}}\boldsymbol{A}_{\mathrm{CC}}^{-1}\boldsymbol{A}_{\mathrm{C}j}, \quad i, j \in \{\mathrm{L}, \mathrm{R}, \mathrm{e}\}, \tag{2.4}$$

and

$$\begin{bmatrix} \boldsymbol{F}'_{\mathrm{L}} \\ \boldsymbol{F}'_{\mathrm{R}} \\ \boldsymbol{q}'_{\mathrm{e}} \end{bmatrix} = \begin{bmatrix} \boldsymbol{F}_{\mathrm{L}} - \boldsymbol{A}_{\mathrm{LC}}\boldsymbol{A}_{\mathrm{CC}}^{-1}\boldsymbol{F}_{\mathrm{C}} \\ \boldsymbol{F}_{\mathrm{R}} - \boldsymbol{A}_{\mathrm{RC}}\boldsymbol{A}_{\mathrm{CC}}^{-1}\boldsymbol{F}_{\mathrm{C}} \\ \boldsymbol{q}_{\mathrm{e}} + \boldsymbol{A}_{\mathrm{eC}}\boldsymbol{A}_{\mathrm{CC}}^{-1}\boldsymbol{F}_{\mathrm{C}} \end{bmatrix}. \tag{2.5}$$

Comparing with the original $\boldsymbol{A}$ matrix equation, the size of $\boldsymbol{B}$ matrix is much smaller since the proportion of DOFs at boundaries is less than 1 of 10 in many cases. Another significant difference is the fact that $\boldsymbol{B}$ matrix is dense while the original FEM matrix is sparse. Solving the $\boldsymbol{B}$ equation could acquire the same values of $\boldsymbol{u}_{\mathrm{L}}$ and $\boldsymbol{u}_{\mathrm{R}}$ as solving $\boldsymbol{A}$ matrix when the same load is given in the right-hand side.

It should be noted that deriving the $\boldsymbol{B}$ matrix costs much more time than solving Eq. (2.2) directly. This is because the Gauss elimination method can be applied in solving Eq. (2.2), whereas the calculation of the inverse matrix $\boldsymbol{A}_{\mathrm{CC}}^{-1}$ is inevitable in deriving the $\boldsymbol{B}$ matrix. The procedure of hierarchical cascading in the next section will compensate for this time consumption.

2.2.2 Cascading *B* matrices

The second step is to cascade $\boldsymbol{B}$ matrices of two identical unit cells A and B into a new unit C (see Figure 2.2). Since $\boldsymbol{u}_{\mathrm{L}}^{\mathrm{A}} = \boldsymbol{u}_{\mathrm{R}}^{\mathrm{B}}$ and $\boldsymbol{T}_{\mathrm{L}}^{\mathrm{A}} + \boldsymbol{T}_{\mathrm{R}}^{\mathrm{B}} = 0$ at the attached boundary, where the superscripts A and B indicate values in the cells A and B, one obtains the

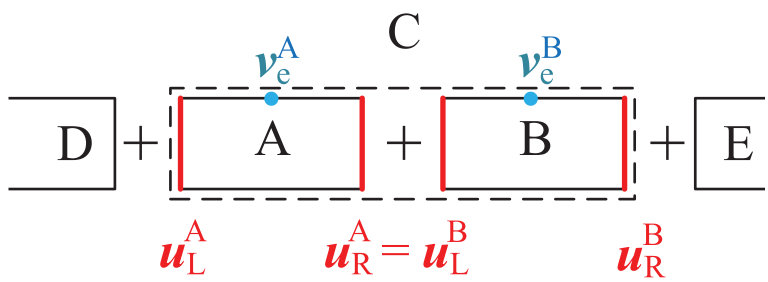

Figure 2.2: Cascading two units A and B into C.

following combined equation:

$$\begin{bmatrix} \boldsymbol{B}_{\mathrm{LL}} & \boldsymbol{B}_{\mathrm{LR}} & \boldsymbol{0} & \boldsymbol{B}_{\mathrm{Le}} \\ \boldsymbol{B}_{\mathrm{RL}} & \boldsymbol{B}_{\mathrm{RR}} + \boldsymbol{B}_{\mathrm{LL}} & \boldsymbol{B}_{\mathrm{LR}} & \boldsymbol{B}_{\mathrm{Re}} \\ \boldsymbol{0} & \boldsymbol{B}_{\mathrm{RL}} & \boldsymbol{B}_{\mathrm{RR}} & \boldsymbol{B}_{\mathrm{Re}} \\ \boldsymbol{B}_{\mathrm{eL}} & \boldsymbol{B}_{\mathrm{eR}} & \boldsymbol{B}_{\mathrm{eR}} & 2\boldsymbol{B}_{\mathrm{ee}} \end{bmatrix} \begin{bmatrix} \boldsymbol{u}_{\mathrm{L}}^{\mathrm{A}} \\ \boldsymbol{u}_{\mathrm{R}}^{\mathrm{A}} \left(= \boldsymbol{u}_{\mathrm{L}}^{\mathrm{B}}\right) \\ \boldsymbol{u}_{\mathrm{R}}^{\mathrm{B}} \\ \boldsymbol{v}_{\mathrm{e}}^{\mathrm{A}} \left(= \boldsymbol{v}_{\mathrm{e}}^{\mathrm{B}}\right) \end{bmatrix} = \begin{bmatrix} \boldsymbol{F'}_{\mathrm{L}} + \boldsymbol{T}_{\mathrm{L}}^{\mathrm{A}} \\ \boldsymbol{F'}_{\mathrm{R}} + \boldsymbol{F'}_{\mathrm{L}} \\ \boldsymbol{F'}_{\mathrm{R}} + \boldsymbol{T}_{\mathrm{R}}^{\mathrm{B}} \\ -2\boldsymbol{q'}_{\mathrm{e}} \end{bmatrix}, \tag{2.6}$$

when electrodes in A and B are conductive, or

$$\begin{bmatrix} \boldsymbol{B}_{\mathrm{LL}} & \boldsymbol{B}_{\mathrm{LR}} & \boldsymbol{0} & \boldsymbol{B}_{\mathrm{Le}} & \boldsymbol{0} \\ \boldsymbol{B}_{\mathrm{RL}} & \boldsymbol{B}_{\mathrm{RR}} + \boldsymbol{B}_{\mathrm{LL}} & \boldsymbol{B}_{\mathrm{LR}} & \boldsymbol{B}_{\mathrm{Re}} & \boldsymbol{B}_{\mathrm{Le}} \\ \boldsymbol{0} & \boldsymbol{B}_{\mathrm{RL}} & \boldsymbol{B}_{\mathrm{RR}} & \boldsymbol{0} & \boldsymbol{B}_{\mathrm{Re}} \\ \boldsymbol{B}_{\mathrm{eL}} & \boldsymbol{B}_{\mathrm{eR}} & \boldsymbol{0} & \boldsymbol{B}_{\mathrm{ee}} & \boldsymbol{0} \\ \boldsymbol{0} & \boldsymbol{B}_{\mathrm{eL}} & \boldsymbol{B}_{\mathrm{eR}} & \boldsymbol{0} & \boldsymbol{B}_{\mathrm{ee}} \end{bmatrix} \begin{bmatrix} \boldsymbol{u}_{\mathrm{L}}^{\mathrm{A}} \\ \boldsymbol{u}_{\mathrm{R}}^{\mathrm{A}} \left(= \boldsymbol{u}_{\mathrm{L}}^{\mathrm{B}}\right) \\ \boldsymbol{u}_{\mathrm{R}}^{\mathrm{B}} \\ \boldsymbol{v}_{\mathrm{e}}^{\mathrm{A}} \\ \boldsymbol{v}_{\mathrm{e}}^{\mathrm{B}} \end{bmatrix} = \begin{bmatrix} \boldsymbol{F'}_{\mathrm{L}} + \boldsymbol{T}_{\mathrm{L}}^{\mathrm{A}} \\ \boldsymbol{F'}_{\mathrm{R}} + \boldsymbol{F'}_{\mathrm{L}} \\ \boldsymbol{F'}_{\mathrm{R}} + \boldsymbol{T}_{\mathrm{R}}^{\mathrm{B}} \\ -\boldsymbol{q'}_{\mathrm{e}} \\ -\boldsymbol{q'}_{\mathrm{e}} \end{bmatrix}, \tag{2.7}$$

when they are electrically isolated. When there are several electrical terminals coexist in A and B, a hybrid equation of Eqs. (2.6) and (2.7) should be applied.

Since Eq. (2.6) and/or Eq. (2.7) have the same form as Eq. (2.2), elimination of $\boldsymbol{u}_{\mathrm{R}}^{\mathrm{A}}$ results in the same form of Eq. (2.3). This means that when identical 2^N blocks are cascaded, the whole $\boldsymbol{B}$ matrix can be assembled by successive application of this algorithm N times (see Figure 2.3).

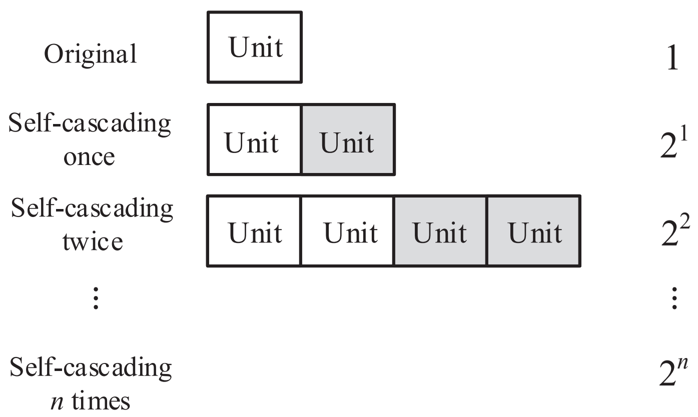

Figure 2.3: Algorithm of hierarchical cascading.

Besides the main periodic structure, the remaining $\boldsymbol{B}$ matrices of some additional non-periodic structures are also cascaded.

As mentioned in the last section, building $\boldsymbol{B}$ matrix itself has no advantage over solving $\boldsymbol{A}$ matrix directly. The exponential growth of the model size is the key to the acceleration the simulation of hierarchical cascading. Therefore, it is important to check whether the target structure is composed of quite a large number of identical units. If not, HCT based simulation may not be appropriate.

2.2.3 Solving and Traceback

The final result will be expressed in the form of

$$\begin{bmatrix} \boldsymbol{B}^{\mathrm{f}}_{\mathrm{LL}} & \boldsymbol{B}^{\mathrm{f}}_{\mathrm{LR}} & \boldsymbol{B}^{\mathrm{f}}_{\mathrm{Le}} \\ \boldsymbol{B}^{\mathrm{f}}_{\mathrm{RL}} & \boldsymbol{B}^{\mathrm{f}}_{\mathrm{RR}} & \boldsymbol{B}^{\mathrm{f}}_{\mathrm{Re}} \\ \boldsymbol{B}^{\mathrm{f}}_{\mathrm{eL}} & \boldsymbol{B}^{\mathrm{f}}_{\mathrm{eR}} & \boldsymbol{B}^{\mathrm{f}}_{\mathrm{ee}} \end{bmatrix} \begin{bmatrix} \boldsymbol{u}^{\mathrm{f}}_{\mathrm{L}} \\ \boldsymbol{u}^{\mathrm{f}}_{\mathrm{R}} \\ \boldsymbol{v}^{\mathrm{f}}_{\mathrm{e}} \end{bmatrix} = \begin{bmatrix} \boldsymbol{F}^{\mathrm{f}}_{\mathrm{L}} \\ \boldsymbol{F}^{\mathrm{f}}_{\mathrm{R}} \\ -\boldsymbol{q}^{\mathrm{f}}_{\mathrm{e}} \end{bmatrix}, \tag{2.8}$$

where $\boldsymbol{B}^{\mathrm{f}}$ is the final $\boldsymbol{B}$ matrix, $\boldsymbol{u}^{\mathrm{f}}_{\mathrm{L}}$ and $\boldsymbol{u}^{\mathrm{f}}_{\mathrm{R}}$ are DOFs located at the final left and right boundaries, and $\boldsymbol{v}^{\mathrm{f}}_{\mathrm{e}}$ is the vector includes all electrical terminals in the model.

It should be noted that all the elements of $\boldsymbol{F}^{\mathrm{f}}_{\mathrm{L}}$ and $\boldsymbol{F}^{\mathrm{f}}_{\mathrm{R}}$ are given because $\boldsymbol{F}_{\mathrm{R}}$ and/or $\boldsymbol{F}_{\mathrm{L}}$ are zero for stress-free boundaries. For clamped boundaries, we can eliminate unknown elements in $\boldsymbol{F}^{\mathrm{f}}_{\mathrm{L}}$ and $\boldsymbol{F}^{\mathrm{f}}_{\mathrm{R}}$ using the condition that corresponding elements in $\boldsymbol{u}_{\mathrm{R}}$ and/or $\boldsymbol{u}_{\mathrm{L}}$ are zero.

Since the voltages applied in all terminals are determined, $\boldsymbol{u}^{\mathrm{f}}_{\mathrm{R}}$ and $\boldsymbol{u}^{\mathrm{f}}_{\mathrm{L}}$ are obtained from

$$\begin{bmatrix} \boldsymbol{u}^{\mathrm{f}}_{\mathrm{L}} \\ \boldsymbol{u}^{\mathrm{f}}_{\mathrm{R}} \end{bmatrix} = \begin{bmatrix} \boldsymbol{B}^{\mathrm{f}}_{\mathrm{LL}} & \boldsymbol{B}^{\mathrm{f}}_{\mathrm{LR}} \\ \boldsymbol{B}^{\mathrm{f}}_{\mathrm{RL}} & \boldsymbol{B}^{\mathrm{f}}_{\mathrm{RR}} \end{bmatrix}^{-1} \left(\begin{bmatrix} \boldsymbol{F}^{\mathrm{f}}_{\mathrm{L}} \\ \boldsymbol{F}^{\mathrm{f}}_{\mathrm{R}} \end{bmatrix} - \begin{bmatrix} \boldsymbol{B}^{\mathrm{f}}_{\mathrm{Le}} \\ \boldsymbol{B}^{\mathrm{f}}_{\mathrm{Re}} \end{bmatrix} \boldsymbol{v}^{\mathrm{f}}_{\mathrm{e}} \right). \tag{2.9}$$

Meanwhile, after the values of $\boldsymbol{u}^{\mathrm{f}}_{\mathrm{R}}$ and $\boldsymbol{u}^{\mathrm{f}}_{\mathrm{L}}$ are determined, the charges corresponding to each terminal can be calculated with

$$\boldsymbol{q}_{\mathrm{e}}^{\mathrm{f}} = -\begin{bmatrix} \boldsymbol{B}_{\mathrm{eL}}^{\mathrm{f}} & \boldsymbol{B}_{\mathrm{eR}}^{\mathrm{f}} & \boldsymbol{B}_{\mathrm{ee}}^{\mathrm{f}} \end{bmatrix} \begin{bmatrix} \boldsymbol{u}_{\mathrm{L}}^{\mathrm{f}} \\ \boldsymbol{u}_{\mathrm{R}}^{\mathrm{f}} \\ \boldsymbol{v}_{\mathrm{e}}^{\mathrm{f}} \end{bmatrix}. \tag{2.10}$$

Then, the electric currents through terminals can be directly calculated as

$$\boldsymbol{I}_{\mathrm{e}} = \frac{\partial \boldsymbol{q}_{\mathrm{e}}^{\mathrm{f}}}{\partial t} = i\omega \boldsymbol{q}_{\mathrm{e}}^{\mathrm{f}}. \tag{2.11}$$

In some cases, data of those eliminated internal DOFs are also useful, and one additional procedure named traceback is given for data recovery.

To explain the algorithm of traceback step, let's turn back to Eq. (2.2). With some determinant transformation, the second line in this equation can be expressed as

$$\boldsymbol{u}_{\mathrm{C}} = \boldsymbol{A}_{\mathrm{CC}}^{-1} \left(\boldsymbol{F}_{\mathrm{C}} - \begin{bmatrix} \boldsymbol{A}_{\mathrm{CL}} & \boldsymbol{A}_{\mathrm{CR}} & \boldsymbol{A}_{\mathrm{Ce}} \end{bmatrix} \begin{bmatrix} \boldsymbol{u}_{\mathrm{L}} \\ \boldsymbol{u}_{\mathrm{R}} \\ \boldsymbol{v}_{\mathrm{e}} \end{bmatrix} \right). \tag{2.12}$$

This means those eliminated internal DOFs ($\boldsymbol{u}_{\mathrm{C}}$) could be calculated provided that $\boldsymbol{u}_{\mathrm{L}}$, $\boldsymbol{u}_{\mathrm{R}}$ and $\boldsymbol{v}_{\mathrm{e}}$ are given. Since $\boldsymbol{u}_{\mathrm{L}}$ and $\boldsymbol{u}_{\mathrm{R}}$ have become new $\boldsymbol{u}_{\mathrm{C}}$ in the next level of cascading, the traceback procedure should start from the final boundaries where $\boldsymbol{u}_{\mathrm{L}}^{\mathrm{f}}$ and $\boldsymbol{u}_{\mathrm{R}}^{\mathrm{f}}$ are determined, and reverse along the cascading tree as shown in Figure 2.4.

Tracing back all the DOFs in the region under concern requires additional computing time and memory to store the inverse matrices generated during the cascading. In the following chapters, the traceback will be used to observe bulk wave leakage in SAW devices and evaluate mode components in BAW devices.

It is obvious that $\boldsymbol{B}$ matrix is a symmetrical dense matrix. Furthermore, when the unit model is lossless, the matrices in Eq. (2.1) are real, and its $\boldsymbol{B}$ matrix is positive definite. In this case, the Cholesky decomposition offers a faster speed in matrix inversion than LU decomposition [101]. However, in most situation, the inclusion of energy loss (PML, thermoelastic damping, Ohmic loss) is inevitable to the model.

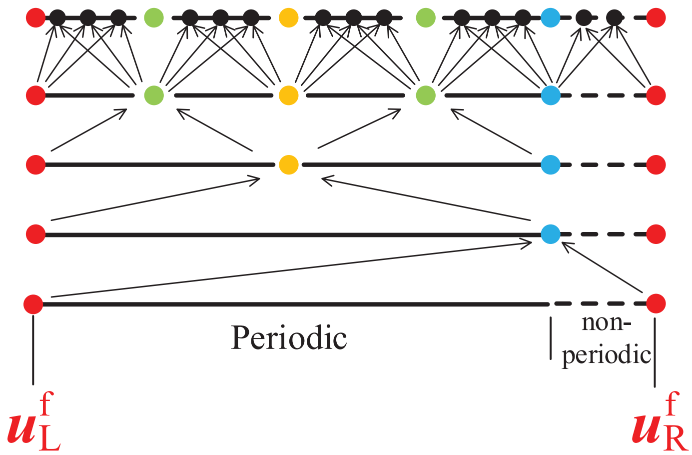

Figure 2.4: Algorithm solution of traceback step.

2.3 Mirror Cascading

When two unit cells possess mirror symmetry as shown in Figure 2.5, inner DOFs in both units can be eliminated. This allows for reducing the number of DOFs.

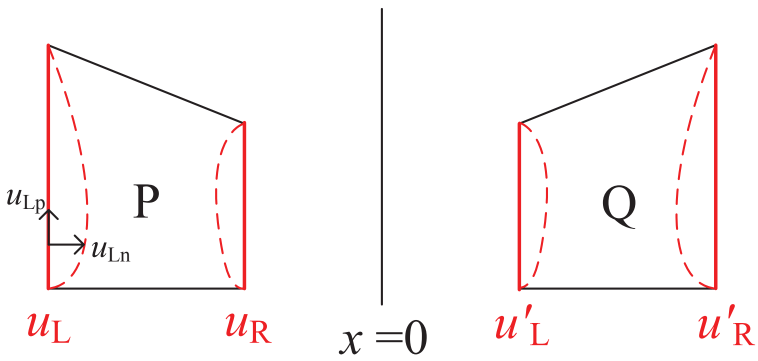

Figure 2.5: Units P and Q in mirror symmetry.

In FEM, the movement of each node is decomposed into two components in two orthogonal directions. Therefore, the DOFs at boundaries are classified into two types based on the direction of its movement which is normal to x=0 ($\boldsymbol{u}_{\mathrm{n}}$), or parallel ($\boldsymbol{u}_{\mathrm{p}}$). The B matrix of the unit P can be expressed as:

$$\begin{bmatrix} \boldsymbol{B}_{11} & \boldsymbol{B}_{12} & \boldsymbol{B}_{13} & \boldsymbol{B}_{14} \\ \boldsymbol{B}_{21} & \boldsymbol{B}_{22} & \boldsymbol{B}_{23} & \boldsymbol{B}_{24} \\ \boldsymbol{B}_{31} & \boldsymbol{B}_{32} & \boldsymbol{B}_{33} & \boldsymbol{B}_{34} \\ \boldsymbol{B}_{41} & \boldsymbol{B}_{42} & \boldsymbol{B}_{43} & \boldsymbol{B}_{44} \end{bmatrix} \begin{bmatrix} \boldsymbol{u}_{\mathrm{L_n}} \\ \boldsymbol{u}_{\mathrm{L_p}} \\ \boldsymbol{u}_{\mathrm{R_n}} \\ \boldsymbol{u}_{\mathrm{R_p}} \end{bmatrix} = \begin{bmatrix} \boldsymbol{T}_{\mathrm{L_n}} \\ \boldsymbol{T}_{\mathrm{L_p}} \\ \boldsymbol{T}_{\mathrm{R_p}} \\ \boldsymbol{T}_{\mathrm{R_p}} \end{bmatrix}. \tag{2.13}$$

Let us indicates the DOFs of the unit Q by giving a prime mark. The symmetrical relation along $x = 0$ are given by

$$\begin{cases} \boldsymbol{u}_{\mathrm{L_n}} = -\boldsymbol{u}'_{\mathrm{R_n}} \\ \boldsymbol{u}_{\mathrm{L_p}} = \boldsymbol{u}'_{\mathrm{R_p}} \\ \boldsymbol{u}_{\mathrm{R_n}} = -\boldsymbol{u}'_{\mathrm{L_n}} \\ \boldsymbol{u}_{\mathrm{R_p}} = \boldsymbol{u}'_{\mathrm{L_p}} \end{cases}, \tag{2.14}$$

and

$$\begin{cases} \boldsymbol{T}_{\mathrm{L_n}} = -\boldsymbol{T}'_{\mathrm{R_n}} \\ \boldsymbol{T}_{\mathrm{L_p}} = \boldsymbol{T}'_{\mathrm{R_p}} \\ \boldsymbol{T}_{\mathrm{R_n}} = -\boldsymbol{T}'_{\mathrm{L_n}} \\ \boldsymbol{T}_{\mathrm{R_p}} = \boldsymbol{T}'_{\mathrm{L_p}} \end{cases}. \tag{2.15}$$

Then the B matrix of the unit Q can be expressed as:

$$\begin{bmatrix} \boldsymbol{B}_{33} & -\boldsymbol{B}_{34} & \boldsymbol{B}_{31} & -\boldsymbol{B}_{32} \\ -\boldsymbol{B}_{43} & \boldsymbol{B}_{44} & -\boldsymbol{B}_{41} & \boldsymbol{B}_{42} \\ \boldsymbol{B}_{13} & -\boldsymbol{B}_{14} & \boldsymbol{B}_{11} & -\boldsymbol{B}_{12} \\ -\boldsymbol{B}_{23} & \boldsymbol{B}_{24} & -\boldsymbol{B}_{21} & \boldsymbol{B}_{22} \end{bmatrix} \begin{bmatrix} \boldsymbol{u}'_{\mathrm{L_n}} \\ \boldsymbol{u}'_{\mathrm{L_p}} \\ \boldsymbol{u}'_{\mathrm{R_n}} \\ \boldsymbol{u}'_{\mathrm{R_p}} \end{bmatrix} = \begin{bmatrix} \boldsymbol{T}'_{\mathrm{L_n}} \\ \boldsymbol{T}'_{\mathrm{L_p}} \\ \boldsymbol{T}'_{\mathrm{R_n}} \\ \boldsymbol{T}'_{\mathrm{R_p}} \end{bmatrix}. \tag{2.16}$$

Next, provided that unit P itself is symmetrical regarding to not only the model structure but also the location of DOFs, the B matrix in Eq. (2.16) is identical with that given in Eq. (2.13). Therefore, the following relations should be hold:

$$\begin{bmatrix} \boldsymbol{B}_{13} & \boldsymbol{B}_{14} \\ \boldsymbol{B}_{23} & \boldsymbol{B}_{24} \\ \boldsymbol{B}_{33} & \boldsymbol{B}_{34} \\ \boldsymbol{B}_{43} & \boldsymbol{B}_{44} \end{bmatrix} = \begin{bmatrix} \boldsymbol{B}_{31} & -\boldsymbol{B}_{32} \\ -\boldsymbol{B}_{41} & \boldsymbol{B}_{42} \\ \boldsymbol{B}_{11} & -\boldsymbol{B}_{12} \\ -\boldsymbol{B}_{21} & \boldsymbol{B}_{22} \end{bmatrix}. \tag{2.17}$$

This relation can also be used for lossless compression of $\boldsymbol{B}$ matrices in memory.

When the mirror symmetry holds, the cascading shown in Figure 2.6(b) can be more efficient because the structure is always symmetrical after the cascading. It is clear that the relations given by Eq. (2.17) can be used to reduce the resulting data size. Furthermore, since the relations are preserved after the cascading, we can skip redundant calculation steps and speed up the cascade operation.

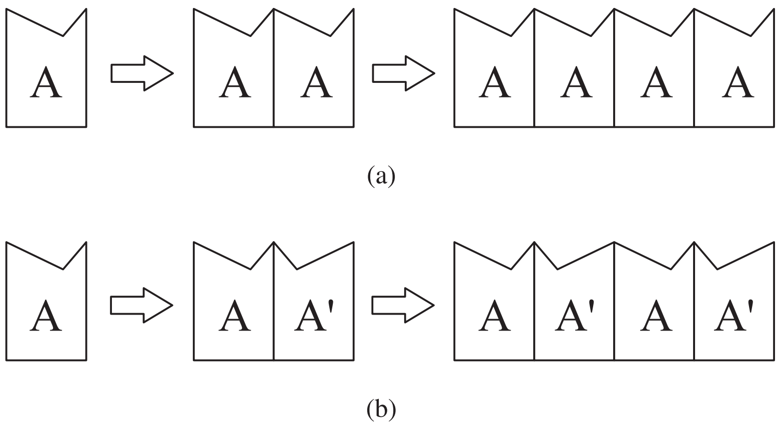

Figure 2.6: Two cascading techniques. (a) Shift cascading, (b) Mirror cascading.

Now there are two kinds of cascading ways. One is special for the symmetrical structure at a higher speed; the other is universal for any cases but slower. The design principle of constructing a cascading tree (such as Figure 1.10) should be somewhat changed due to the introduction of mirror cascading. To optimize the calculating speed further, symmetrical structures in each level of the cascading tree should be placed as many as possible.

2.4 Practical Process

Nowadays, many commercial FEM software, such as COMSOL and ANSYS, has friendly and convenient HMI (Human Machine Interface), and powerful modeling capability across multiple physical fields. Figure 2.7 presents the developed practical process flow for the HCT FEM simulation based on COMSOL Multiphysics 5.3a and MATLAB 2018b. [102].

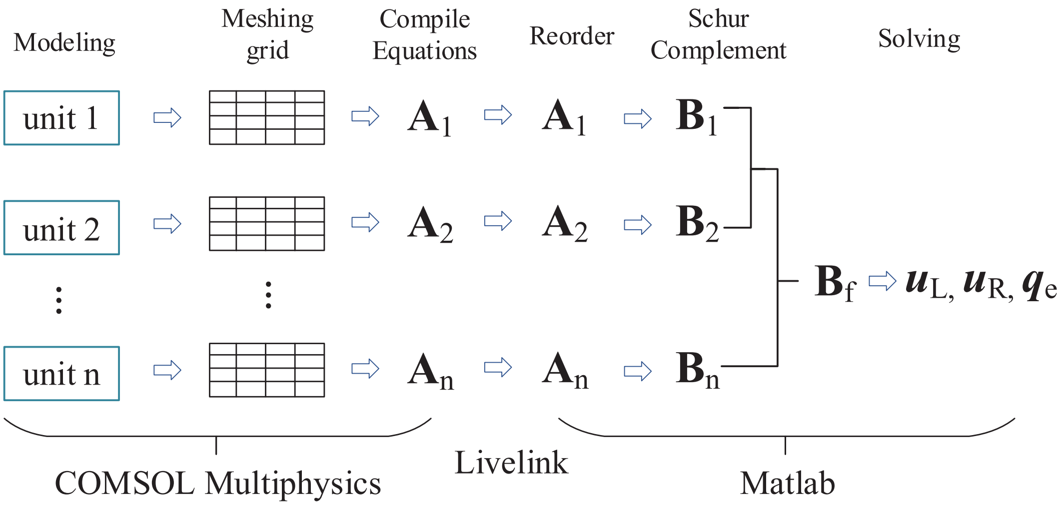

Figure 2.7: The process flow of realizing HCT FEM calculation based on COMSOL and Matlab.

The cross-platform of COMSOL allows dynamic visual operations of modeling, setting multi-factor coupling physical fields and meshing grids with multiple options conveniently. After building units, COMSOL generates their FEM equations.

The next step is to import the generated $\boldsymbol{A}$ matrices from COMSOL to MATLAB thorough COMSOL Livelink with MATLAB [103]. Another important data is the information of all DOFs. They include the coordinates and types of each DOF. Since the sequence of DOFs in the matrices generated by COMSOL are sorted in its own rules, classifying those $\boldsymbol{u}_{\mathrm{L}}$ and $\boldsymbol{u}_{\mathrm{R}}$ and then reordering the sequence of variables is necessary.

Based on my experiments, the speed of assembling $\boldsymbol{A}$ matrix at a specific frequency in COMSOL is much slower than assembling it in Matlab. The data transfer from COMSOL to Matlab will also cost additional time. One efficient way is executing computation in Matlab as much as possible. Based on Eq. (2.1), generating the $\boldsymbol{A}$ matrix in COMSOL three times at different frequencies f_1, f_2 and f_3, three components $\boldsymbol{K}$, $\boldsymbol{D}$ and $\boldsymbol{M}$ can be obtained with

$$\begin{bmatrix} \boldsymbol{K} \\ \boldsymbol{D} \\ \boldsymbol{M} \end{bmatrix} = \begin{bmatrix} 1 & i2\pi f_1 & -4\pi^2 f_1^2 \\ 1 & i2\pi f_2 & -4\pi^2 f_2^2 \\ 1 & i2\pi f_3 & -4\pi^2 f_3^2 \end{bmatrix}^{-1} \begin{bmatrix} \boldsymbol{A}(f_1) \\ \boldsymbol{A}(f_2) \\ \boldsymbol{A}(f_3) \end{bmatrix}. \tag{2.18}$$

It is also pointed that when PML region is included in model, its $\boldsymbol{A}$ matrix can be expressed a function of frequency f as [92]

$$\boldsymbol{A}(f) = \boldsymbol{a} \cdot f^{-1} + \boldsymbol{b} + \boldsymbol{c} \cdot f + \boldsymbol{d} \cdot f^2. \tag{2.19}$$

Hence, $\boldsymbol{A}$ matrices are required at four different frequencies in this case.

After transporting the necessary number of $\boldsymbol{A}$ matrices and all DOFs' information to Matlab, remaining steps of this process flow can be operated in Matlab.

2.5 Simulation of 2.5D SAW Model with HCT

Next, HCT is applied to the simulation of a large 2.5D SAW model (a plane model assuming uniformity in one (y) direction.) with the process flow given in the last section. This SAW simulation is the original purpose that HCT invented for [86]. The SAW resonator model with a wavelength of 4.0 μm has a Cu electrode (0.2 μm) on the piezoelectric $LiTaO_3$ 42° YX-cut substrate. As shown in Figure 2.8, there are 32 electrode pairs in the center interdigital transducer. Bragg reflectors on both sides have 32 electrodes. Two flat regions with a length of 32 μm are placed at the outside. The damping absorbing boundaries which will be introduced in the next chapter are applied to perform the same function as PML.

Table 2.1 shows the computation time required for the simulation. The number of DOFs in the model of Figure 2.8 is larger than 2,000,000, which is too large to

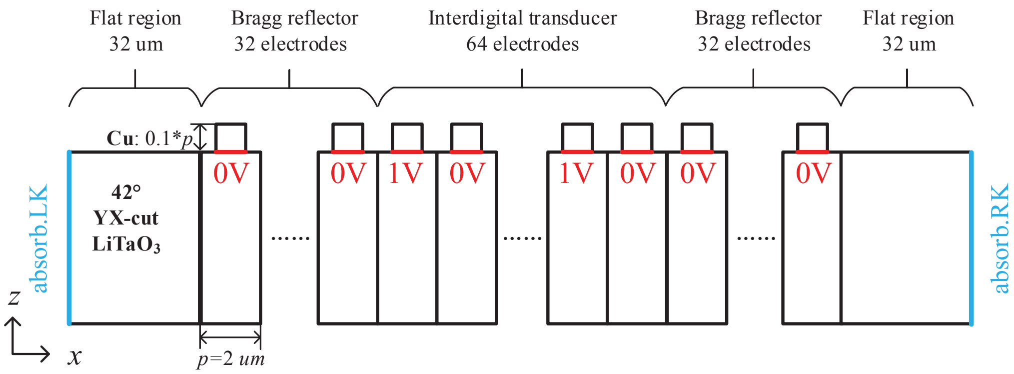

Figure 2.8: Structure of HCT SAW model of 42° YX-cut $LiTaO_3$ with Cu electrodes.

simulate it directly in a workstation using COMSOL or other commercial FEM software. Nevertheless, with the help of HCT, the simulation time is only 19.9 sec. per each frequency.

Actually, the total time can be further reduced. For example, most of the time is spent for obtaining the absorbing lines. This part of time can be shortened significantly if PML is used instead of absorbing line with sacrificing some accuracy.

Table 2.1: Time consumption in the simulation with HCT of the model in Figure 2.8.

Step	Time (sec.)
Obtain absorbing lines	12.5
A matrices to B matrices	1.6
Cascade B matrices	3.0
Solve out all the DOFs	2.8
Total time	19.9

Figure 2.9 shows the simulated admittance curve of the SAW resonator in Figure 2.8. In addition to the main resonance and anti-resonance of 925 MHz and 978 MHz, there are several spurious peaks in the admittance curve identified. To investigate the reasons for each spurious peaks, the displacement component u_y in the xz plane (sagittal plane) are also calculated at these frequencies. The results are shown in Figure 2.10.

It is obvious that the spurious peak around 1044 MHz is caused by the excitation and scattering of the bulk wave. On the other hand, standing patterns are clearly seen at 927.5 MHz and 930.5 MHz. This indicates that they are due to longitudinal mode resonances. These results coincide well with previously published work [93].

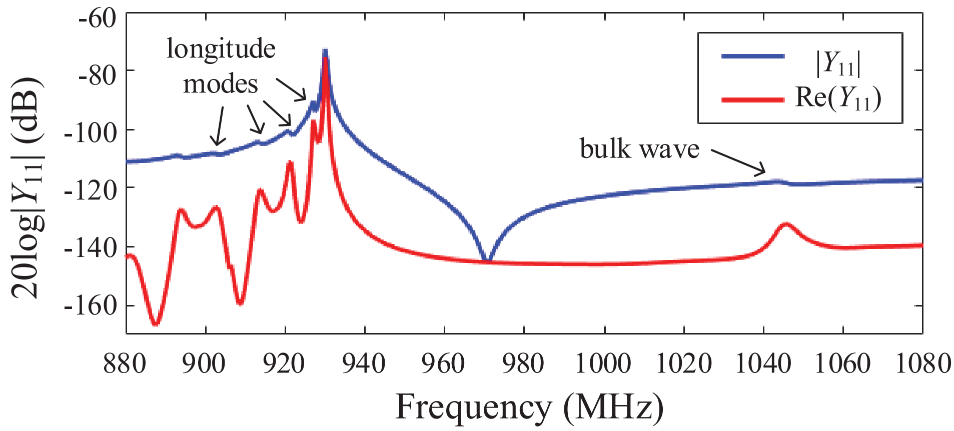

Figure 2.9: Simulated admittance Y_{11} of a 42° YX-$LiTaO_3$ resonator.

Next, an Al/128° YX-$LiNbO_3$ resonator is also simulated. It has more IDT electrodes and the number of DOFs is larger than 8 million. The obtained electrical response is shown in Figure 2.11. Spurious peaks caused by different modes are all marked by arrows in the figure. The calculation took 23 sec. for each frequency point, which is only 3 sec. longer than the simulation of Figure 2.8.

2.6 Conclusion

This chapter details the HCT algorithm.

First, the overall process of HCT in the matrix operation level was illustrated. It includes deriving the ***B*** matrix from traditional FEM equations, combining and cascading two ***B*** matrices and tracing back of eliminated DOFs after solving the ***B*** equation.

Mirror cascading was proposed as an auxiliary cascading way. Even though it is only applicable for symmetrical structures, its time consumption is at least a half of the traditional HCT for obtaining the same B matrix. This means that the hierarchical

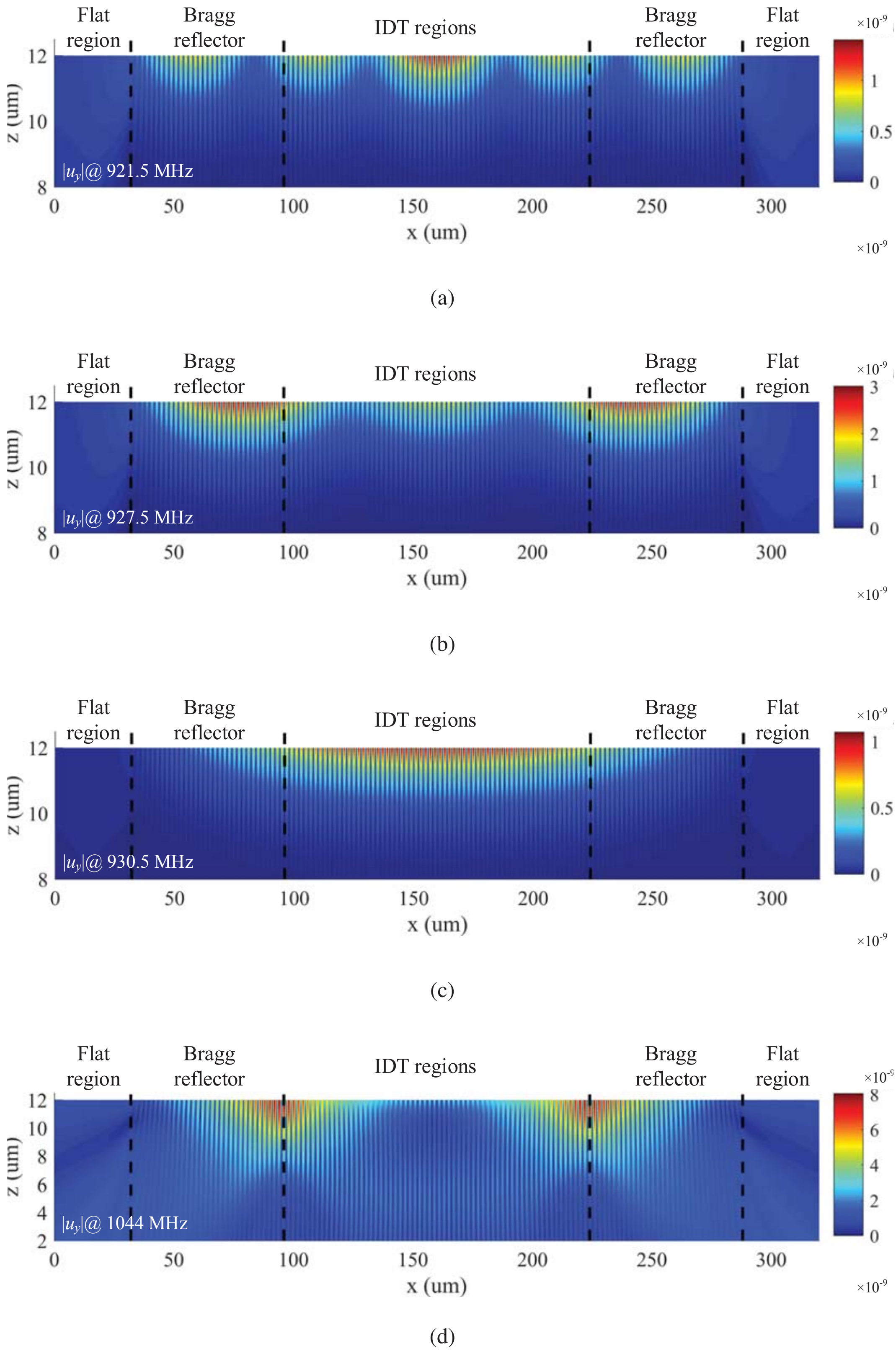

Figure 2.10: Simulated displacement fields in y direction. (a) 921.5 MHz, (b) 927.5 MHz, (c) 930.5 MHz, (d) 1044 MHz.

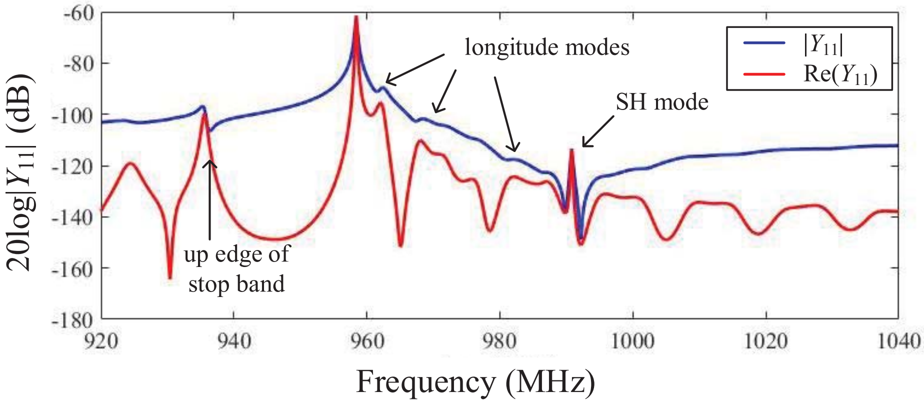

Figure 2.11: Simulated admittance Y_{11} curve of a 128° YX-LiNbO$_3$ resonator.

cascading tree should be chosen properly to take this advantage as much as possible provided that the structural symmetry exists.

Then, a process flow of HCT based on commercial software was introduced. COMSOL's GUI and Matlab's calculation environment are combined in this method.

Finally, electrical response and field distribution of a 2.5D SAW resonator model with 2 million DOFs was analyzed as a demonstration, and effectiveness of the HCT based simulation was proven.

Chapter 3

HCT Implementation in Traveling Wave Source Model

3.1 Introduction

The radiation condition plays an important role in the analysis of wave propagation in semi-infinite structures. In the FEM analysis, the PML is often used to suppress unnecessary reflections [75, 76]. As introduced in Chapter 1, the conventional PML setting is invalid when at least one of the wave components possesses negative group velocity often referred to the type-II dispersion. For the TWS application to BAW device structures, this is a serious problem because the main Lamb mode often exhibits this property.

In this chapter, a new type of absorbing setting named infinite long damping boundary (ILDB) is proposed. It is shown that various kinds of SAW/BAW scattering problems can be solved speedily and accurately when ILDB and HCT are implemented simultaneously into the TWS model.

Unlike the stretching coordinate strategy used in PML, neither typical wavelength nor stretching direction is needed to define. The next section illustrates the operation mechanism of this new absorbing boundary, and how to apply it in the model. Then, a comparison between conventional PML and ILDB will be given.

Next, HCT combined with TWS and ILDB is applied to the analysis of the Lamb wave scattering at a free end. Simulated results are compared between calculations using traditional FEM and HCT based one. Huge advantages are obtained in both simulation speed and accuracy.

Then, HCT is used to accelerate the parametric sweeping simulation for transverse mode analysis in SAW devices. The developed technique is applied for the calculation of input admittance Y of infinitely long IDTs, and also the estimation of the reflection coefficient Γ at the IDT fingertips using TWS model. It is shown that the Γ estimation is more efficient than the Y calculation for designing the piston mode structure.

Finally, HCT implemented TWS model is also applied to the analysis of scattering at the discontinuity between two periodic gratings. To the author's best knowledge, this is the first approach to analyze wave scattering phenomena at a discontinuity sandwiched between two semi-infinite long periodic structures.

3.2 Infinite Long Damping Boundary

3.2.1 Building B Matrix

HCT allows us to extend the length of the simulation target easily. For example, when a thin slice waveguide with 1 μm length is cascaded 20 times, the final waveguide is longer than 1 km. Note that the meshed grid remains the same fineness as the original mesh grid even after cascading. In this long waveguide, waves can not transmit between two ends when tiny damping is given. Furthermore, when waves are incident from another identical but loss-less waveguide, no reflection will occur at the boundary. This means that the long waveguide is ideal as a radiation boundary for the FEM analysis.

Figure 3.1 shows the composition of the proposed damping mechanism. The wave is supposed to propagate from the right side to the left. The isotropic damping factor $\eta_{\rm s}$ is introduced to each unit as an imaginary part in the mass. Its effect is the same as damping matrix $\boldsymbol{D}$. The value of $\eta_{\rm s}$ increases for the first unit (unit (a) in Figure 3.1), and becomes constant (unit (b) in Figure 3.1). The HCT enables calculating the total $\boldsymbol{B}$ matrix of the cascaded region even when the cascading number is extremely large, provided that the number is an integer power of 2. The gradual increase in $\eta_{\rm s}$ is introduced to avoid reflection caused by the variation of acoustic impedance.

As mentioned, wave injected from one end cannot reach to the other end in this waveguide when the cascading time is large enough. Namely, $\boldsymbol{u}_{\rm L}$ and $\boldsymbol{u}_{\rm R}$ will not influence

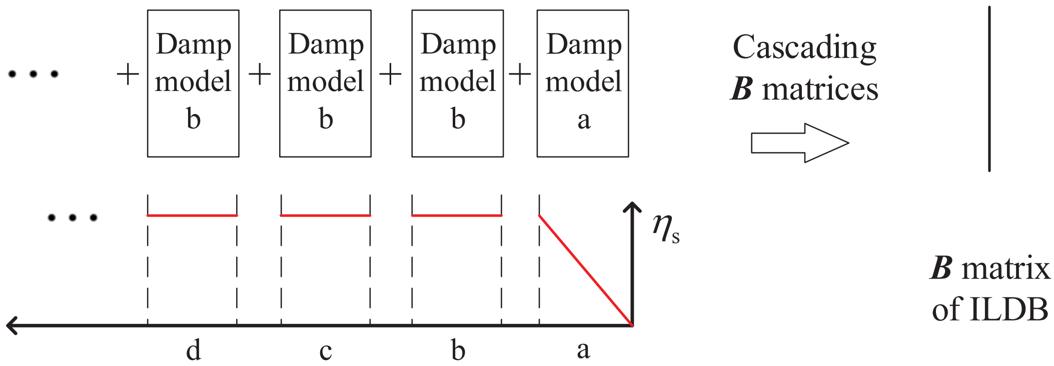

Figure 3.1: Variation of damping factor η_s in damping region where waves are incident from the right end.

each other. Then the $\boldsymbol{B}$ matrix equation for ILDB will be in the form of

$$\begin{bmatrix} \boldsymbol{B}_{\mathrm{LL}}^{\mathrm{ILDB}} & \boldsymbol{0} \\ \boldsymbol{0} & \boldsymbol{B}_{\mathrm{RR}}^{\mathrm{ILDB}} \end{bmatrix} \begin{bmatrix} \boldsymbol{u}_{\mathrm{L}}^{\mathrm{ILDB}} \\ \boldsymbol{u}_{\mathrm{R}}^{\mathrm{ILDB}} \end{bmatrix} = \begin{bmatrix} \boldsymbol{T}_{\mathrm{L}}^{\mathrm{ILDB}} \\ \boldsymbol{T}_{\mathrm{R}}^{\mathrm{ILDB}} \end{bmatrix}. \tag{3.1}$$

It can be split into two independent equations. The lower one is regarded as a restriction equation at the right boundary:

$$\boldsymbol{B}_{\mathrm{RR}}^{\mathrm{ILDB}} \boldsymbol{u}_{\mathrm{R}}^{\mathrm{ILDB}} = \boldsymbol{T}_{\mathrm{R}}^{\mathrm{ILDB}}. \tag{3.2}$$

When ILDB is placed on the left side of unit C, the cascading operation of their $\boldsymbol{B}$ matrices gives

$$\begin{bmatrix} \boldsymbol{B}_{\mathrm{LL}}^{\mathrm{C}} + \boldsymbol{B}_{\mathrm{RR}}^{\mathrm{ILDB}} & \boldsymbol{0} \\ \boldsymbol{0} & \boldsymbol{B}_{\mathrm{RR}}^{\mathrm{C}} \end{bmatrix} \begin{bmatrix} \boldsymbol{u}_{\mathrm{L}}^{\mathrm{C}} (= u_{\mathrm{R}}^{\mathrm{ILDB}}) \\ \boldsymbol{u}_{\mathrm{R}}^{\mathrm{C}} \end{bmatrix} = \begin{bmatrix} \boldsymbol{0} \\ \boldsymbol{T}_{\mathrm{R}}^{\mathrm{C}} \end{bmatrix}. \tag{3.3}$$

3.2.2 Performance of ILDB

Next, the generated ILDB is used to check with PML on the absorption performance of Lamb waves in an AlN thin plate. Figure 3.2 shows the dispersion curves of Lamb waves propagating in the plate. Horizontal and vertical axes are $B = \beta h$ and $F = fh$ where β is the wavenumber, f is the frequency, and h is the AlN thickness. Usually, F increases with B. This is called the type-I dispersion, and indicates that the group velocity is directed to the same direction as the phase velocity. In contrast, F decreases with B on one branch labeled "S1-". This is called the type-II dispersion and indicates that the directions of phase and group velocities are opposite.

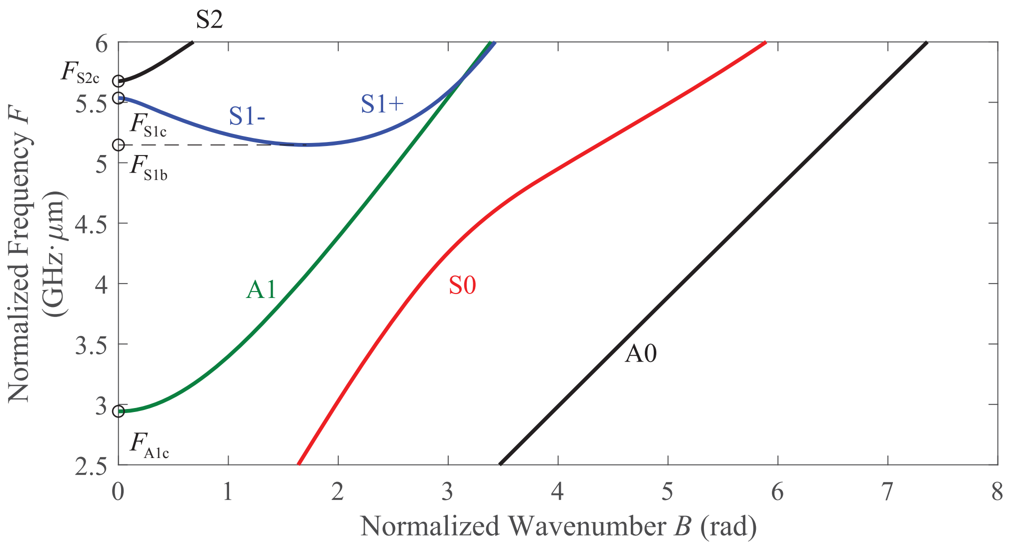

Figure 3.2: Normalized dispersion relations of Lamb modes of a AlN plate.

Figure 3.3 shows the FEM models used to check the wave absorption. Normal forces are applied in the right free end of the waveguide. Forces at the top and bottom surfaces have equi-amplitude but opposite direction. Symmetrical Lamb waves are excited selectively and propagate to the $-x$ direction. The frequency of driving force is set a little below F_{S1c} shown in Figure 3.2. The wavelength of S1- wave is hundreds of times

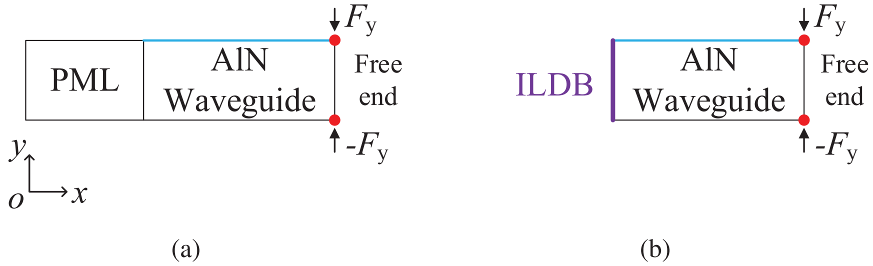

Figure 3.3: FEM models for absorption test. (a) PML, (b) ILDB.

longer than that of the S0 mode.

After the FEM calculation, displacements at the top surface (blue line) are extracted, and the fast Fourier transform (FFT) is applied to decompose into Lamb mode components. Figure 3.4(a) shows the resulting wave spectrum utilizing PML. Incident waves are labeled as (i) while reflected waves as (r). It should be noted that owing to the type-II dispersion, the direction of the group velocity of the S1- wave is opposite to that of the phase velocity, and so an incident S1- mode wave possesses a positive wavenumber.

Although various parameter settings were examined in the PML [77], it was not possible to suppress reflected waves, especially S1-(r).

Figure 3.4(b) shows the spectrum obtained when the damping boundary is applied instead of the PML region. In contrast to Figure 3.4(a), all incident waves are absorbed completely. Even the reflected S1- wave whose B is close to zero is absorbed well.

3.3 Scattering analysis of BAW

In the last section, the problem of absorbing energy in a waveguide under the peculiar condition is perfectly resolved by ILDB. In this section, HCT was implemented into the entire TWS model to accelerate the simulation for both BAW and SAW devices.

3.3.1 Model Setting

Since the main body of BAW devices is laterally uniform in general, it is clear that the HCT is more effective for BAW devices than for SAW devices. HCT and ILDB are applied to the 2D TWS BAW model shown in Figure 3.5, which is used to analyze the scattering of Lamb waves at the free plate edge of the FBAR structure. The waveguide is made of a piezoelectric material AlN, whose top and bottom surfaces are metallized.

Phase variation of the TWS is set so that either S1+ or S0 Lamb wave with the wavenumber β is predominantly excited at the active area. The relationship between frequency f and corresponding β in the active region can be referred to normalized

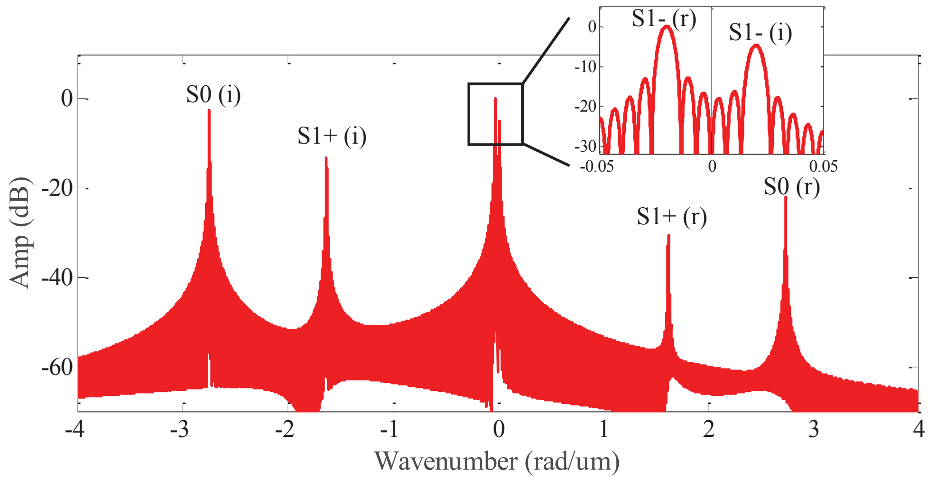

(a)

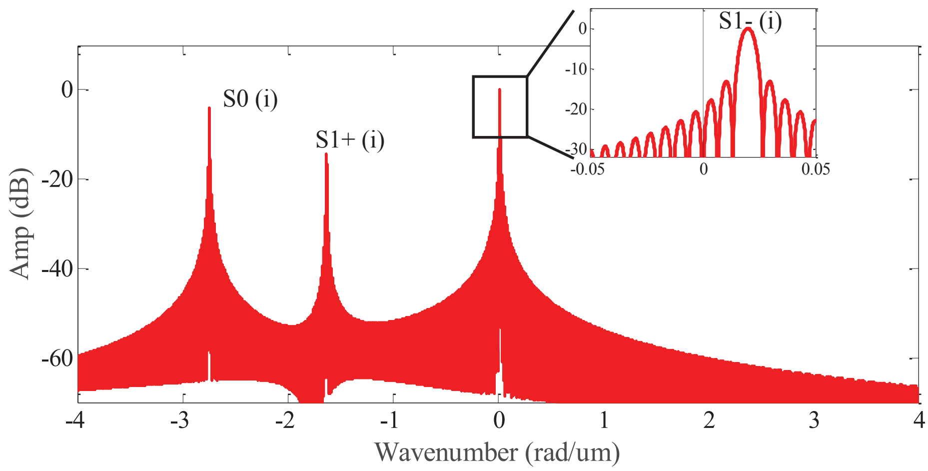

(b)

Figure 3.4: Wave spectrum of the waveguide. (a) PML, (b) ILDB.

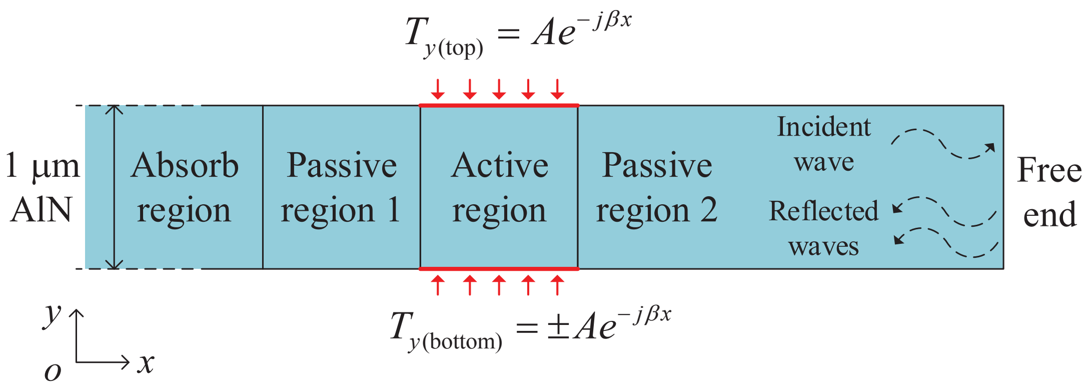

Figure 3.5: Schematic TWS BAW model.

dispersion curves of Lamb modes in Figure 3.2. The excited Lamb wave will reach the free end boundary, and scattered waves are sensed at the passive region 2. Those reflected waves are finally absorbed in the absorbing region.

The $\boldsymbol{B}$ matrix of the active area is assembled by the HCT using a number of thin slices. The traveling wave sources require a phase shift $\phi = -\beta\Delta$ per unit slice in $\boldsymbol{F}$. This requires slight modification of the original HCT.

Here, expressing the $\boldsymbol{B}$ matrix after cascading n times as $\boldsymbol{B}^n$. Then the combined $\boldsymbol{B}$ matrix after cascading $n+1$ times is given by

$$\begin{pmatrix} \boldsymbol{B}_{11}^n & \boldsymbol{B}_{12}^n & \boldsymbol{0} \\ \boldsymbol{B}_{21}^n & \boldsymbol{B}_{22}^n + \boldsymbol{B}_{11}^n & \boldsymbol{B}_{12}^n \\ \boldsymbol{0} & \boldsymbol{B}_{21}^n & \boldsymbol{B}_{22}^n \end{pmatrix} \begin{pmatrix} \boldsymbol{u}_{\mathrm{L}}^{n+1} (= \boldsymbol{u}_{\mathrm{L}}^n) \\ \boldsymbol{u}_{\mathrm{I}}^{n+1} (= \boldsymbol{u}_{\mathrm{R}}^n) \\ \boldsymbol{u}_{\mathrm{R}}^{n+1} \end{pmatrix} = \begin{pmatrix} \boldsymbol{F}_{\mathrm{L}}^n \\ \boldsymbol{F}_{\mathrm{R}}^n + e^{jn\phi} \boldsymbol{F}_{\mathrm{L}}^n \\ e^{jn\phi} \boldsymbol{F}_{\mathrm{R}}^n \end{pmatrix}. \tag{3.4}$$

Several repetitions of hierarchical cascading are enough to build a long waveguide from a thin slice. The whole model is assembled from one thin slice, as shown in Figure 3.6. First, the $\boldsymbol{B}^{\mathrm{f}}$ matrix of the main body is calculated using the HCT. Then ILDB matrix is calculated and placed at the left end. Finally, $\boldsymbol{u}_{\mathrm{L}}^{\mathrm{f}}$ and $\boldsymbol{u}_{\mathrm{R}}^{\mathrm{f}}$ are derived by solving the linear equations, and the remaining DOFs are estimated recursively using the traceback procedure. To save time, passive regions share the same $\boldsymbol{B}$ matrix with the active region but $\boldsymbol{F} = 0$.

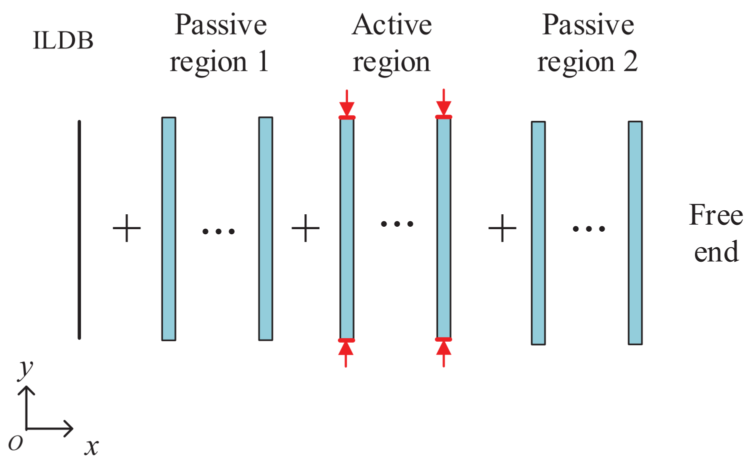

Figure 3.6: Assembled TWS BAW model.

3.3.2 Simulation result

The simulation was performed using a PC (CPU i7-5820K, 3.3 GHz, 128 GB RAM). The driving frequency was set below the cutoff frequency of the main (S1-) mode F_{S1c} owing to its type-II dispersion [78].

For comparison, the whole model was also directly analyzed by the FEM. It is worth noting that the damping area was shortened and the damping factor η_{s} was made larger for the direct FEM analysis to shrink the model size and shorten the calculation time. This change would somewhat worsen the attenuation especially when the driving frequency is close to the cutoff frequency.

Figure 3.7 shows the calculated out-of-plane displacement at the top surface in passive region 2. The displacement calculated by the conventional FEM is also shown for comparison. They show good agreement, and it is difficult to determine which method is more correct.

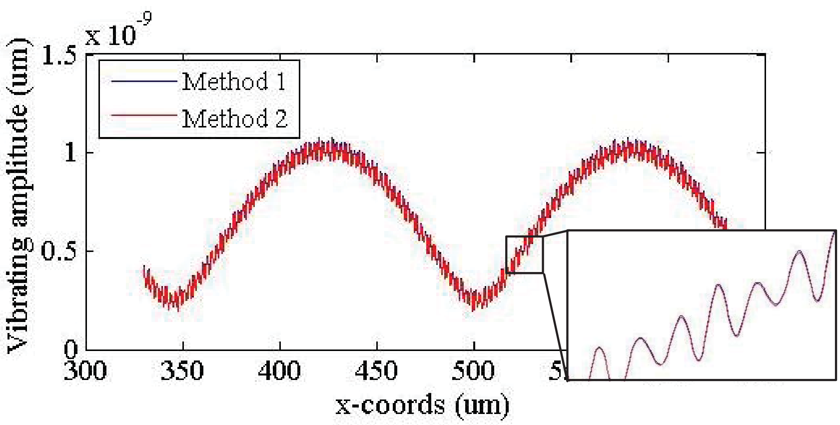

Figure 3.7: Calculated out-of-plane displacement.

In the HCT, 2.9 sec. is necessary to extract the $\boldsymbol{A}$ matrix of the thin slice from COMSOL to MATLAB, and obtaining the ILDB on both sides takes 4 sec. On the other hand, time consumption in the hierarchical cascading and recursive calculation is only 0.7 sec.

In contrast, the direct FEM calculation needs 42 sec. to solve the whole model including the damping area. Note that when more accuracy is necessary and attenuation is increased at the damping region, the execution time will increase further.

After the FEM analysis, the vibrating amplitude at the top surface was converted to carrying power using the method proposed in [104]. Since no additional loss mechanism is included, the law of power conservation requests that the total power reflection coefficient R_{p} defined by the following equation should be unity:

$$R_{\mathrm{p}} = \frac{P_{\mathrm{r,S1-}} + P_{\mathrm{r,S1+}} + P_{\mathrm{r,S0}} + P_{\mathrm{r,S2}}}{P_{\mathrm{i,S1+}} \text{ or } P_{\mathrm{i,S0}}}, \tag{3.5}$$

where P_{i} and P_{r} are incident and back-scattered power, respectively, and the second subscript specifies the mode.

Figure 3.8 shows the power scattering coefficients calculated by the TWS method. In the figure, the horizontal axis is the frequency - (AlN) thickness product F, and F_{S1b}, F_{S1c} and F_{S2c} are those at the cutoff for the S1-, S1+, and S2 modes, respectively. The deviation is quite small in Figure 3.8 even when F is close to F_{S1c}. Since the wavelength of S1- at F_{S1c} is infinite (β=0 rad./μm), the extremely long waveguide is necessary. This long model is difficult in direct FEM application, but an easy task for HCT.

3.4 Piston Mode Design of SAW

In this section, the design of piston mode structures is demonstrated with the help of HCT.

3.4.1 Parametric Sweeping with HCT

Before specifying the model for simulation, another beneficial usage of HCT needs to be introduced. One major consideration of HCT is reuse of intermediate results such as cascaded B-matrices. For optimization of SAW devices, it is common that device properties are simulated with scanning one or two parameters in the device structure, and the remaining parts are unchanged. In the conventional parametric sweeping simulation,

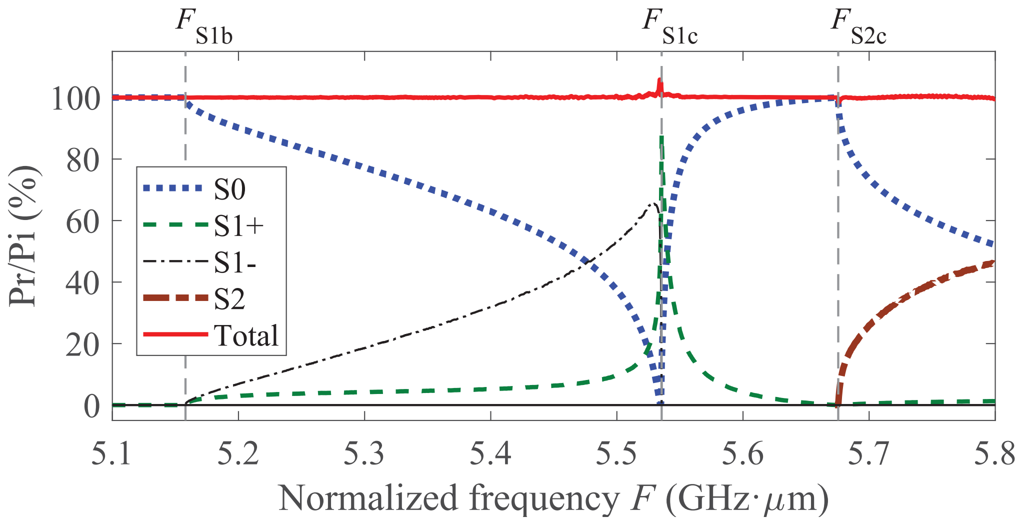

(a)

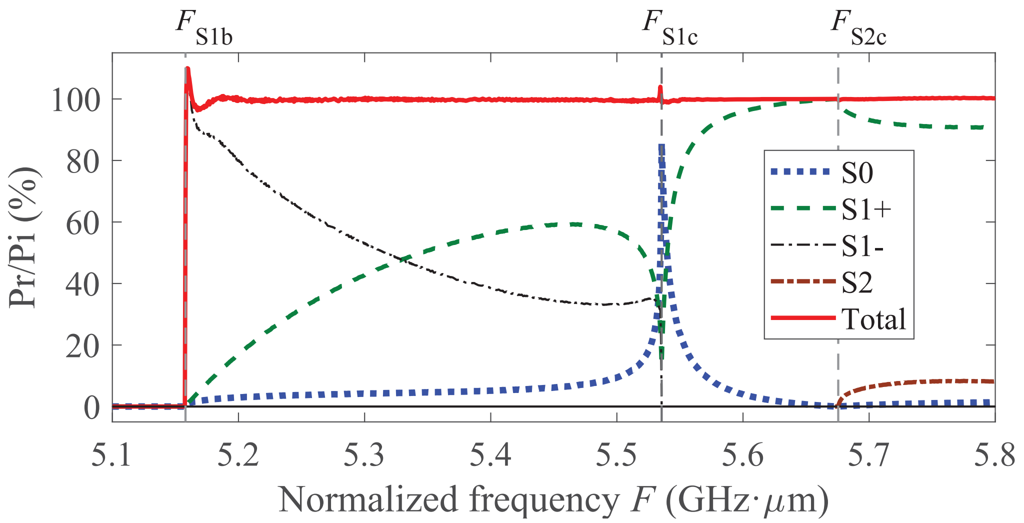

(b)

Figure 3.8: Scattering behavior at the free end calculated by the TWS-HCT method. (a) S0 mode incidence, (b) S1+ mode incidence (S1+ is evanescent at F < F_{S1b})

the FEM equation of the whole structure is built and solved for all parameter values. In HCT, on the other hand, it is possible that omitting the B-matrix calculation for the major portion, and thus the optimizing procedure can be simplified. Let us consider a model shown in Figure 3.9. The ***B*** matrix of DOFs at the interface (red lines) represents the whole static part. It can be used just like ILDB. This feature allows researchers to shorten the calculating time significantly from the second iteration.

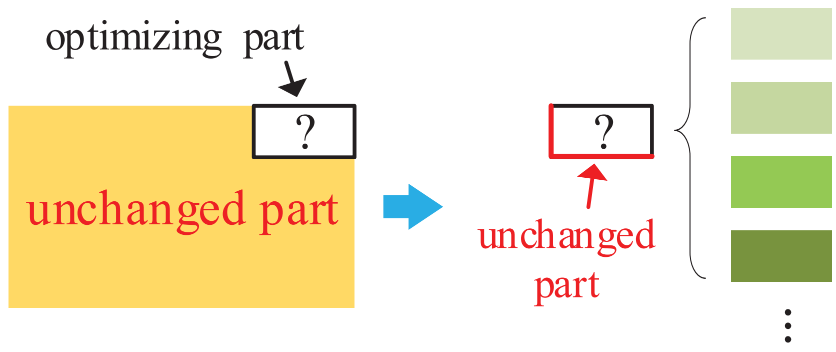

Figure 3.9: Applying HCT for optimization.

3.4.2 Transverse Mode Suppression

Next, HCT is applied to design of side edges in SAW devices. The SiO_2-overlay/Al-electrode/128°YX-$LiNbO_3$-substrate structure similar to the one in Ref. 105 is chosen as an example.

Figure 3.10 shows the border structure for piston mode operation. And Figure 3.11 shows the cross sectional ($x - z$) view of three functional regions in Figure 3.10. The first one is the Al IDT region where SAW is excited. The second one is the slow region placed for the piston mode operation [106–108], where a thin Cu layer is deposited on the top of Al electrodes. The third one is the fast region placed in the outside of the slow region. Here, the length of fast region is assumed to be semi-infinite, and the dummy electrodes and bus-bars are ignored for simplicity.

PML are placed at the bottom of three regions. A half period is chosen, and the symmetrical boundary condition is applied for the sections shown in Figure 3.11. The

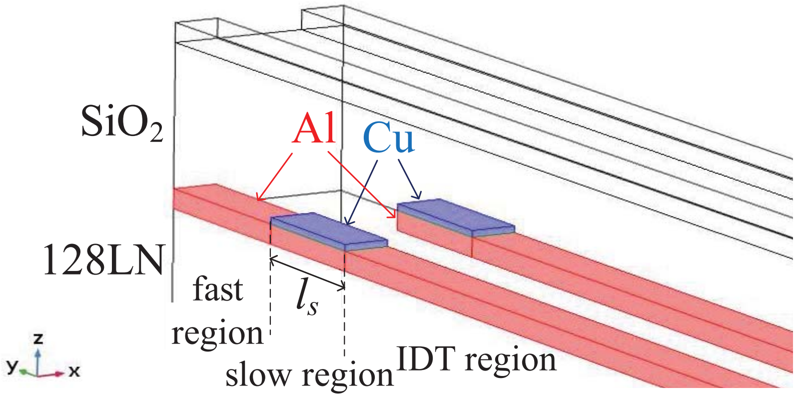

Figure 3.10: Device configuration for piston mode operation using phase-shifters.

ILDB is applied to the side edges instead of PML to obtain better suppression of acoustic reflection.

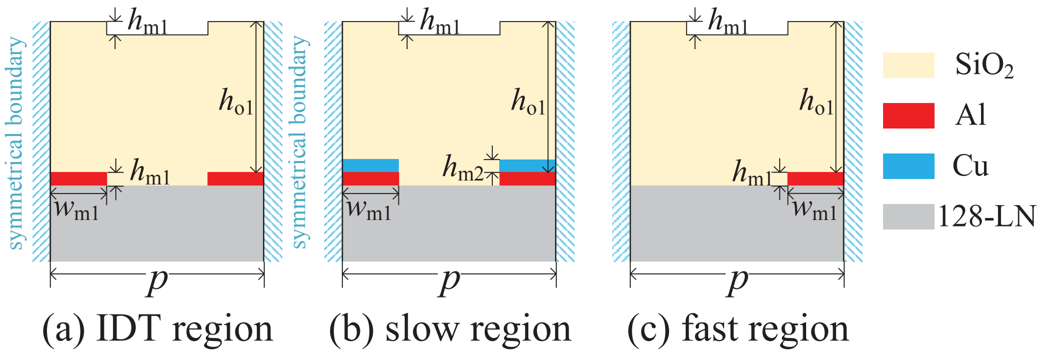

Figure 3.11: Cross sectional view of three regions.

Key parameters are the Cu thickness h_{m2} and the length of slow region l_s. Fixed parameters are listed in Table 3.1.

Figure 3.12 shows a part of the SAW device model decomposed into several units. In the figure, units b and c represent the piezoelectric substrate, while units a1 and a2 include electrodes. The structure is assumed to be periodic toward the x-direction, and the periodicity is $2p$.

Table 3.1: Fixed parameters in model.

Symbol	Value	Description
p	2 μm	grating period
h_{o1}	2 μm	SiO_2 thickness
h_{m1}	0.24 μm	Al thickness
η	0.5	metallization ratio
l_{IDT}	$51p$	length of IDT region

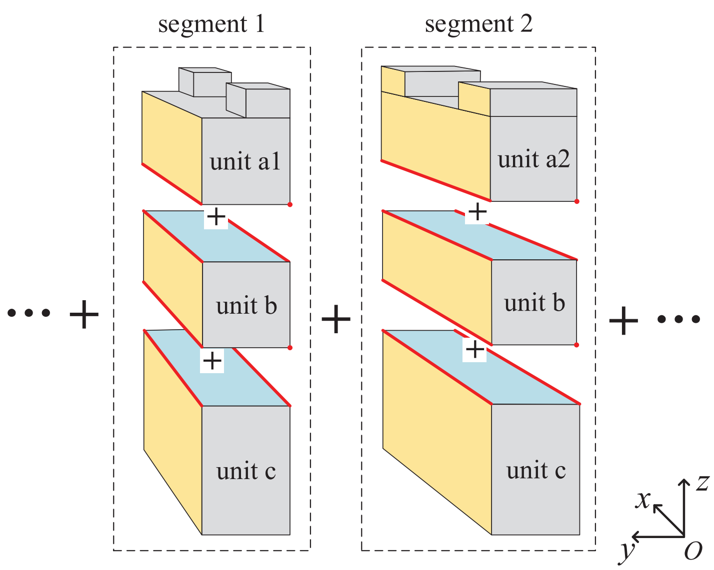

Figure 3.12: Cascading SAW model in y and z directions.

3.4.3 Parametric Sweeping in Y_{11} Model

The direct way is to calculate the input admittance (Y_{11}). The whole FEM model is decomposed into seven regions as shown in Figure 3.13. In this figure, F, S and I indicate fast, slow and IDT regions, respectively. Seven kinds of segments marked as 1-7 in Figure 3.13 are used to cascade.

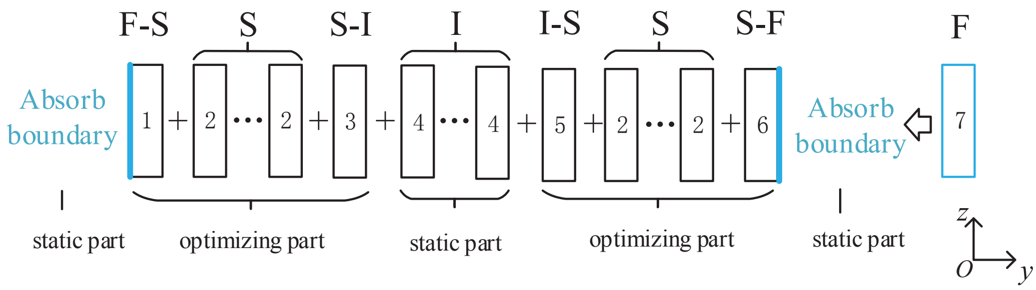

Figure 3.13: Decomposition of the whole FEM model for Y_{11} calculation.

Ideally, only the region S changes with h_{m2} and l_{s}. However, since the auto-mesh function is employed in COMSOL, change in the parameters influences location of DOFs near the region S. To avoid this problem, four transition regions F-S, S-F, S-I and I-S are added. The width of unit S can be set any value as needed, and 0.4 μm is chosen in this simulation. Mirror cascading is applied when cascading region I and S. The total number of DOFs in the model is more than 2 millions (absorb boundary is excluded).

Figure 3.14 shows variation of calculated Y_{11} with l_{s}. In this calculation, $h_{\mathrm{m2}} = 0.08\mu\mathrm{m}$. It is seen that transverse mode resonances are well suppressed when $l_{\mathrm{s}} \sim 2.4 - 2.8\mu\mathrm{m}$.

When the calculation was performed by a CPU (Intel Xeon W-2123) with 128 GB DDR4 memory, the simulation takes about 20 min. for each frequency point for the initial parameter setting while it was shortened to 2.5 min. for the following parameter settings.

The FEM analysis without HCT is also examined. Of course, no difference could be found between two calculations. It took 25 min. for each case, and no acceleration was obtained for the parameter scan.

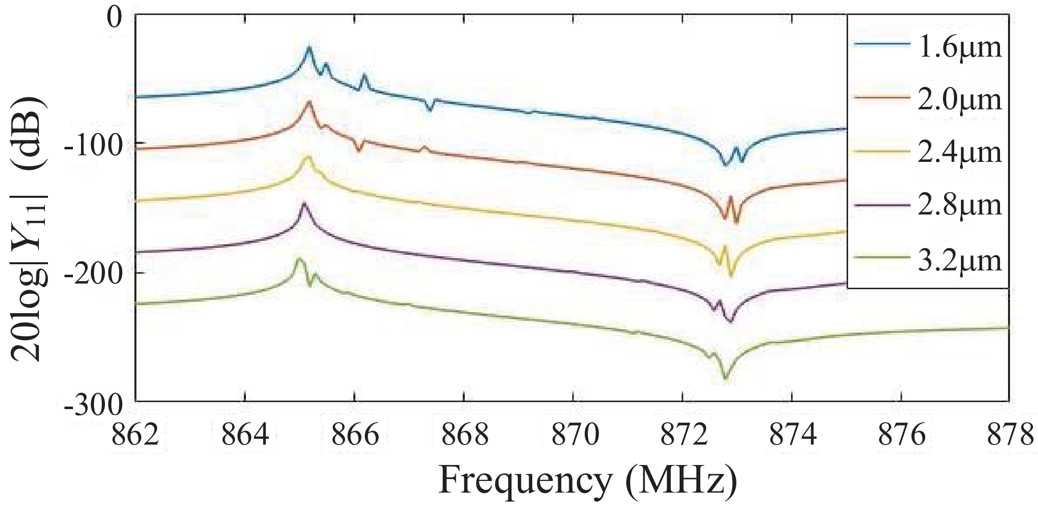

Figure 3.14: Variation of Y_{11} when $l_{\rm s}$ is chosen as a parameter.

3.4.4 Parametric Sweep with TWS Model

One drawback of the method described above is that more than one hundred frequency points are needed for the evaluation. When the frequency step is coarse, spurious peaks may be hardly visible.

By the way, the operation mechanism of the piston mode is explained as follows. The standing wave is created in the IDT region by superposition of laterally propagating forward and backward SAWs. The high-order modes occur when the following condition is satisfied:

$$-2l_{\rm IDT}\cdot\beta_y(f)+2\angle\Gamma(f)=2n\pi\quad(n=1,2,\cdots),\tag{3.6}$$

where β_y is the lateral (y) wavenumber of SAW in the IDT region and Γ is the reflection coefficient at the boundary between the IDT and slow region. The equation indicates that $\angle\Gamma$ and $l_{\rm IDT}$ determine where the resonances occur. It is known that the piston mode operation is possible provided that $\angle\Gamma=0°$ [106–108].

It should be noted that that $|\Gamma|$ should be close to unity. Or the resonance quality factor Q will be deteriorated not only for spurious resonances but also the main one.

Here HCT is combined with the TWS to estimate Γ directly. The model setup is

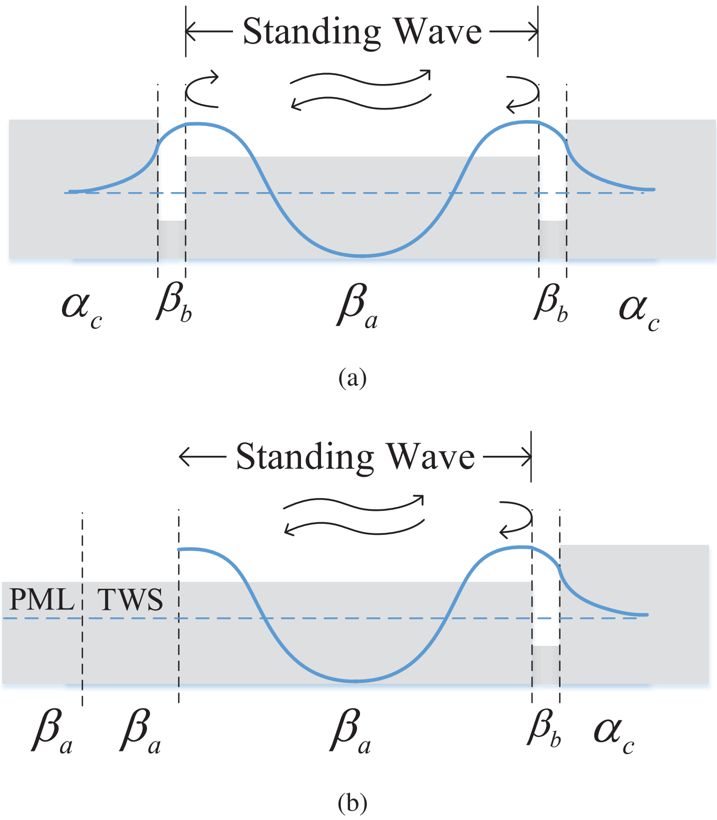

Figure 3.15: Mode setup for Y_{11} and Γ evaluation.

shown in Figure 3.16. As the TWS, external physical force $F(y)$ is given to active IDT region (red arrows), and its y dependence is given by $e^{-j\beta_y y}$, where β_y is the lateral SAW wavenumber in the IDT region. The TWS allows us to excite the particular transverse mode selectively. SAW scattering parameters at the region S can be evaluated by the fast Fourier Transform (FFT) of the surface displacements in two passive regions. The number of DOFs in TWS mode varies from 0.5 to 20 millions. It is due to the fact that the smaller β_y needs longer passive regions for accurate FFT.

The frequency dispersion of β_y can be calculated by the use of the technique given in Ref. [109]. Note β_y is almost zero at the main resonance, and decreases with f.

Figure 3.17 shows variation of estimated $\angle\Gamma$ with l_s. It is seen that $\angle\Gamma(\beta_y)$ becomes zero only when l_s is smaller than 2.8 μm. The location of β_{y0} and f_0 giving $\angle\Gamma = 0$ increase with l_s. Furthermore, $|\angle\Gamma|$ is small for a wide range of β_y and f. Therefore, it is concluded that l_s should be set around 2.4 μm for the transverse mode suppression. This

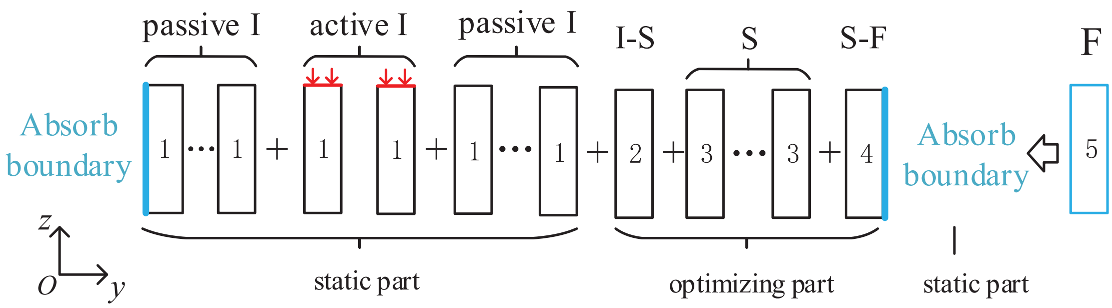

Figure 3.16: Decomposition of the whole FEM model for Γ evaluation.

is consistent with the result shown in the above subsection. It is worth to notice that Γ can be calculated when β_y is very close to 0 by setting the lengths of active and passive regions extremely long. Since Γ changes with β_y smoothly, extrapolation is effective.

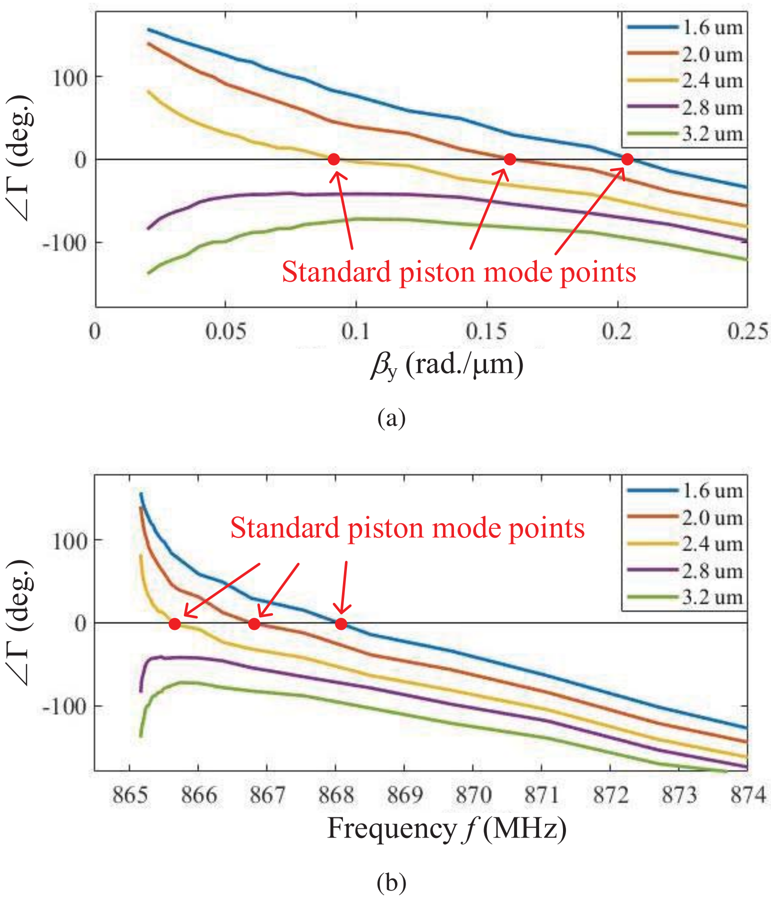

Figure 3.17: Variation of angle of Γ with l_s. (a) β_y dependence of angle of Γ, (b) f dependence of angle of Γ

When the only CPU was used, the calculation time is 30 min. for the first run and 2 min. for following runs.

Note that the curve of $\angle\Gamma$ changes smoothly with β_y and f. Therefore, twenty points in β_y or f are enough for the present purpose. Thus this approach requires much less total computation time than the Y_{11} estimation.

Table 3.2: Comparison of simulation time between different approaches.

Approach	Initial setting Time T_i	Sweeping time T_s	Freq. points N_f
CPU for Y_{11}	20 min.	20 min.	>200
CPU for Γ	30 min.	2 min.	<30
GPGPU for Y_{11}	2 min.	11 sec.	>200
GPGPU for Γ	3 min.	9 sec.	<30

Table 3.2 summaries the time consumption between different approaches. The total time for piston mode design T_{total} is given by

$$T_{\text{total}} = (T_i + T_s * N_s) * N_f, \tag{3.7}$$

where N_s is the number of trial cases. It is obvious that HCT based TWS model owns a huge advantage in the rapid design of piston mode.

The table also shows the results when the general-purpose graphic processor unit (GPGPU) is applied. It is seen that the total time is further reduced from days to several minutes when HCT, TWS model and GPGPU are applied together. Details on this topic will be given in the following chapter.

3.5 Scattering at Discontinuity Between Two Periodic Gratings

The discontinuous gap under concern in this section is shown in Figure 3.18. The space gap with length l_g is embedded into two periodic gratings. It is worth to point out that l_g could be set as a negative value which means shortening the space between two electrodes. There will be two main problems when putting it directly in FEM simulation. One is long simulation time because hundreds of gratings are included, the other is setting of absorb region. Traditional PML is not feasible here due to additional reflection is inevitable at the interface between the absorbing region and the passive region.

The TWS model is also shown in Figure 3.18. Traveling vertical forces (red arrows) are applied to generate single SAW mode.

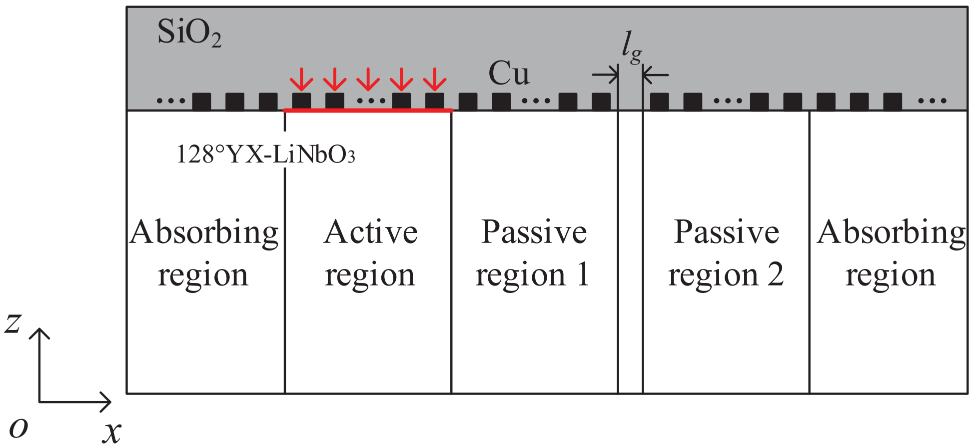

Figure 3.18: TWS model for reflection analysis at discontinuous gap.

Since ILDB is generated by HCT, almost semi-infinite periodic gratings are applicable to the absorbing regions. This characteristic of ILDB is perfect for application to the absorbing regions in Figure 3.18.

After finishing the calculation, the fast Fourier transform is applied to the obtained SAW fields at the top surface of two passive regions. The reflection and transmission coefficients S_{11} and S_{21} can be evaluated from the calculated amplitudes in their wave spectra, respectively.

Typical parameters are given in the following calculations. The grating period p is 2 μm, the thickness of SiO_2 and Cu are set as $8p$ and $0.3p$ respectively. In this condition, the SAW resonance frequency f_r (lower edge of the stop band) is 926.4 MHz. The same length of $256p$ is given in both active and passive regions.

The calculated shear vertical (z) displacement is shown in Figure 3.19. The frequency is set at 921 MHz, which is a little lower than f_r. The corresponding wavenumber of incident Rayleigh SAW is $\beta_i = 0.9821\pi/p$. The gap of $l_g = -50\%p$ is placed at $x = 512$ μm.

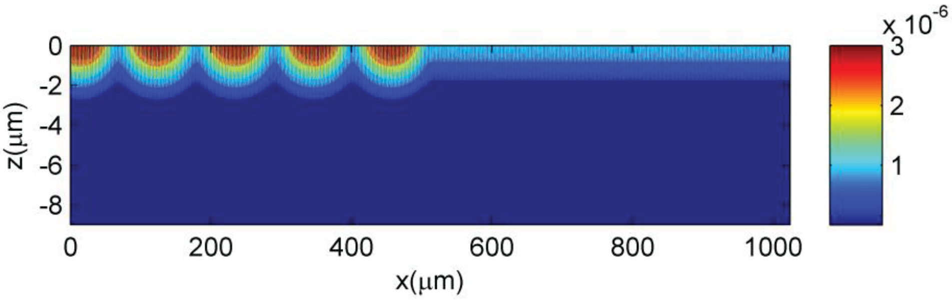

Figure 3.19: Simulated shear vertical displacement (z direction) of passive regions 1 and 2.

Figure 3.20(a) shows the wavenumber domain spectrum of evaluated vertical displacement obtained by the FFT of the surface amplitude in the passive region 1. The horizontal axis is normalized by π/p. Four peaks can be seen. Two of the peaks labeled as s_3 and s_2 correspond to main bodies of SAWs propagating toward the $\pm x$ directions while the other two peaks labeled s_1 and s_4 correspond to the field components caused by the coupling between forward and backward propagating modes in the COM theory [110]. In fact, they possess the wavenumber of (2$\pm$0.9821)π/p. Thus the ratio between s_2 and s_3 peaks gives the reflection coefficient, while that between s_1 and s_3 peaks (or s_4 and s_2 peaks) gives the coupling strength of the modes. Figure 3.20(b) shows the spectrum in the passive region 2. In this case, only two peaks appear. This means that SAW energy propagates only to the +x direction. This confirms that the ILDB works perfectly to suppress SAW back scattering in the region.

Amplitudes of these six peaks were evaluated and given in Table 3.3. The reflection and transmission coefficients S_{11} and S_{21}, respectively, can be obtained by s_2/s_3 and s_6/s_3.

Detailed discussions have been made on the influence of discontinuities for both Rayleigh and SH SAWs, and its results can be seen in Ref. 111.

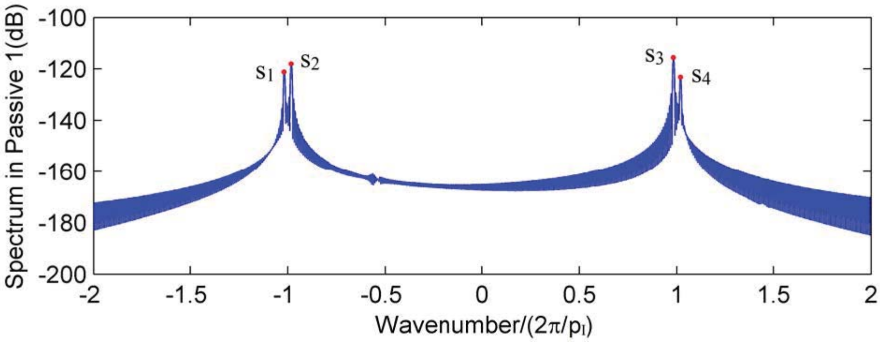

(a)

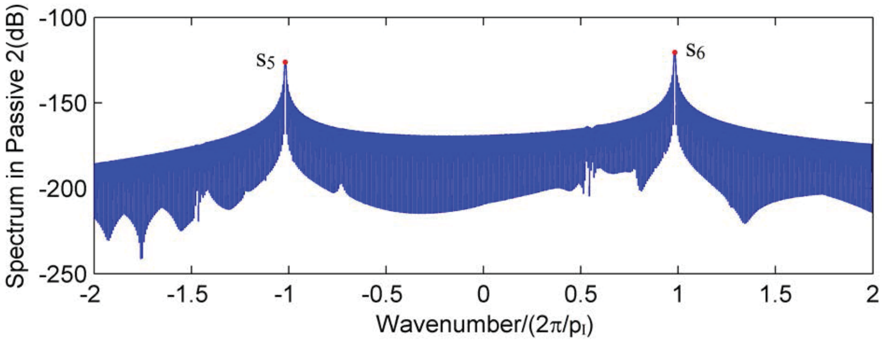

(b)

Figure 3.20: Wave spectrum of displacement at the surface using FFT. (a) Passive region 1, (b) Passive region 2.

3.6 Conclusion

In this chapter, HCT was implemented into the TWS model to deal with several tough problems in SAW/BAW devices. It was demonstrated that all these problems were solved rapidly and accurately with the help of HCT.

First, ILDB based on HCT was proposed and developed as a novel method to absorb energy as the new type of radiation condition. Without stretching coordinate, ILDB can replace PML to simulate infinite region in many cases with better performance.

Then, HCT and ILDB were implemented into the TWS model to accelerate the simulation for scattering analysis in SAW/BAW devices. In the BAW case, it was shown that the scattering behavior of Lamb modes could be extracted very quickly and accurately. For the SAW case, two models were implemented: one was the impedance calculation, and another was the calculation of scattering coefficients at discontinuities. It was

Table 3.3: Values of the peaks in Figure 3.20.

Peaks	S_1	S_2	S_3	S_4	S_5	S_6
Wavenumber (π/p)	-1.018	-0.9821	0.9821	1.018	-1.018	0.9821
Amplitude (dB)	-121.4	-118.2	-116.1	-123.3	-126.1	-120.5
Phase (deg.)	-93.99	43.18	157.68	-96.01	-22.75	-96.02

shown that although the former is straightforward and comprehensive, the latter is more efficient and accurate for the purpose.

Finally, the HCT implemented TWS was applied to analyze scattering at the discontinuity between periodic gratings of Rayleigh wave in the SiO_2/Cu/128-LN structure. ILDB worked perfectly as absorbers in this TWS model. Scattering parameter of Rayleigh wave at the discontinuity could be calculated quickly and successfully.

Chapter 4

Simulation of Full 3D SAW Model Using GPGPU

4.1 Introduction

Even though the competence of HCT has been proved in various aspects in SAW/BAW simulation, it still encountered some troubles for simulation of whole 3D device structures [90]. This problem is caused by the fact that the whole FEM model is too large. For $n \times n$ dense matrices, time consumption for their operation is known to be proportional to n^3. In the 2D cases [89, 93], required n is usually smaller than 1000. In contrast, n will be more than 5000 in the 3D case.

This chapter discusses the applicability of GPGPU to 3D FEM simulation of whole SAW devices using HCT. SAW structures on a 42°YX-$LiTaO_3$ (42-LT) substrate are chosen as an example, and variation of device performance with the electrode pattern is discussed.

First, it is shown how high-end GPGPU is effective for the present purpose. When the problem size is large, GPGPU accelerates the calculation speed more than ten times.

Next, a synchronous SAW resonator on a 42°YX-$LiTaO_3$ substrate is simulated using GPGPU. Only 153 seconds is required to compute its electrical response at one fquency point.

In the end, surface vibration fields are derived from the calculated result, and SAW scattering properties are discussed using the wavenumber domain analysis.

4.2 Cascading Using General-Purpose Graphics Processing Unit

In HCT, the computation time is mostly governed by the operation of the form of $K_1^{-1}K_2$ instead of $K_3^{-1}L$ in the traditional FEM, where K_1 and K_2 are dense complex matrices for each cell, K_3 is a sparse complex matrix for the whole model, and L is a vector. When cascading two identical units, the sizes of K_1 and K_2 are all N-by-N, where N is the number of DOFs in a unit cell. Note that since the matrices are dense, the calculation time increases rapidly with N and is known to be proportional to N^3. This tendency is not important for 2D cases because N is not so large ($< 1,000$) in general. On the other hand, it is not true for the 3D case.

The situation is different when a high-spec GPGPU like NVIDIA GV100 is applied for HCT calculation. Table 4.1 compares its catalog spec with that of Intel Xeon microprocessor which used in the previous simulation.The GPGPU possesses so many cores for the double-precision floating point (FP64) calculation and drastic acceleration is possible by parallelization. The dense matrix operation fits well with this, and has already been implemented in Matlab as parallel computing tool kit.

Figure 4.1 shows the performance comparison between Intel Xeon and GV100 in solving $K_1^{-1}K_2$ with different N. It is clear that use of GPGPU is advantageous when N is large, and the acceleration reaches to more than 10 when N is close to 10^4. When N is small, the core clock is more important than the number of cores.

Table 4.1: Catalog specs of selected CPU and GPGPU.

	Intel Xeon W-2123	NVIDIA GV100
Number of Cores	4	5,120
FP64 Performance	0.23 TFLOPS	7.4 TFLOPS
Configured Memory	128 GB DDR4	32 GB HBM2
Core clock	3.6 GHz	1.2 GHz

The figure also shows the required memory size. It is proportional to N^2, and the maximum N is limited to circa 10^4 when GV100 is employed. It should be noted that

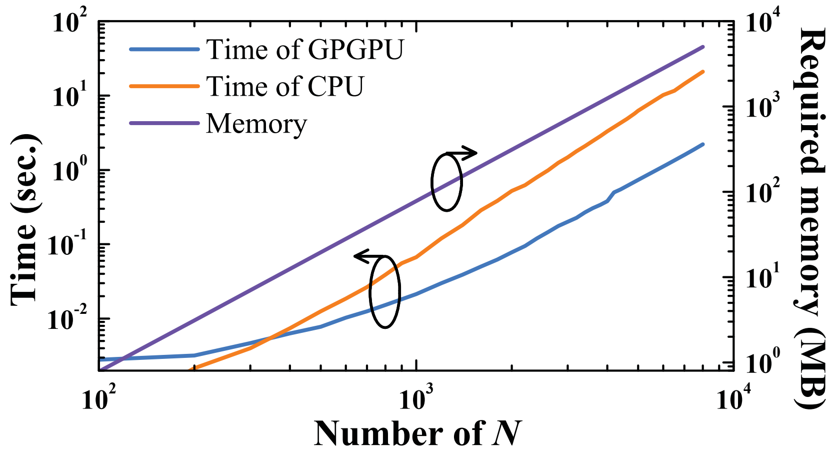

Figure 4.1: Performance comparison between selected CPU and GPGPU in calculation of $K_1^{-1}K_2$.

memory chips of GPGPU are integrated into the board and not extendable by users. Although external memories might be used, their use will result in drastic degradation of total calculation speed.

These results indicate that although the use of GPGPU is effective for the numerical calculation, limiting the required memory size is crucial.

4.3 3D Simulation of Whole SAW Devices

Here HCT is applied to the 3D simulation of SAW resonators on 42-LT, and the effectiveness of GPGPU is demonstrated.

4.3.1 Modeling Setting

Figure 4.2 shows the schematic of 3D FEM model used in this paper. The perfectly matched layers (PML) are placed in surroundings of the Cu electrode region and the bottom of the piezoelectric substrate (42-LT). Parameters in the model are listed in Table. 4.2.

One major consideration on the models of basic cells is how to construct the hierarchical cascading tree so that the efficiency of cascading can reach maximum. In other

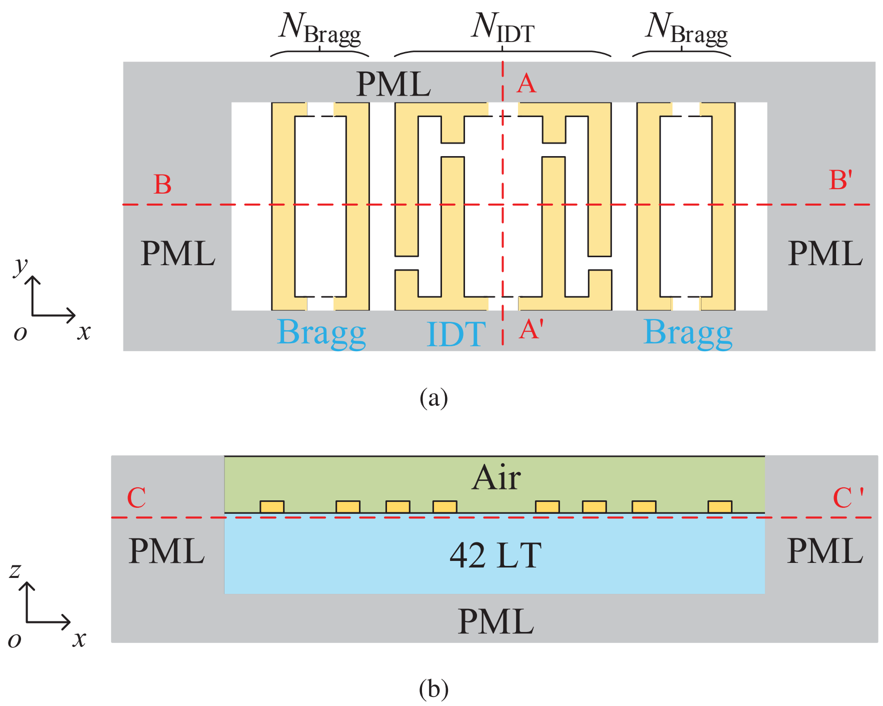

Figure 4.2: Schematic of the final 3D FEM model. (a) Top view, (b) Cross section in the middle.

Table 4.2: Parameters in the full 3D model.

Symbol	Value	Description
λ	5.854 μm	length of lambda
h_{m}	0.3 μm	thickness of electrodes
h_{a}	0.5*λ	thickness of air
l_{IDT}	15*λ	length of IDT region
l_{d}	1*λ	length of dummy region
l_{g}	0.5*λ	length of gap
N_{Bragg}	-	reflector number
N_{IDT}	-	number of electrodes

words, obtained ***B*** matrices should have as high repetitive rate as possible. In Solal's work [90], the unit cells for cascading were divided as shown in Figure 4.3. Since the nodes included in each unit is at least 19,000 [90], the time cost for building ***B*** matrix from each ***A*** matrix could be huge.

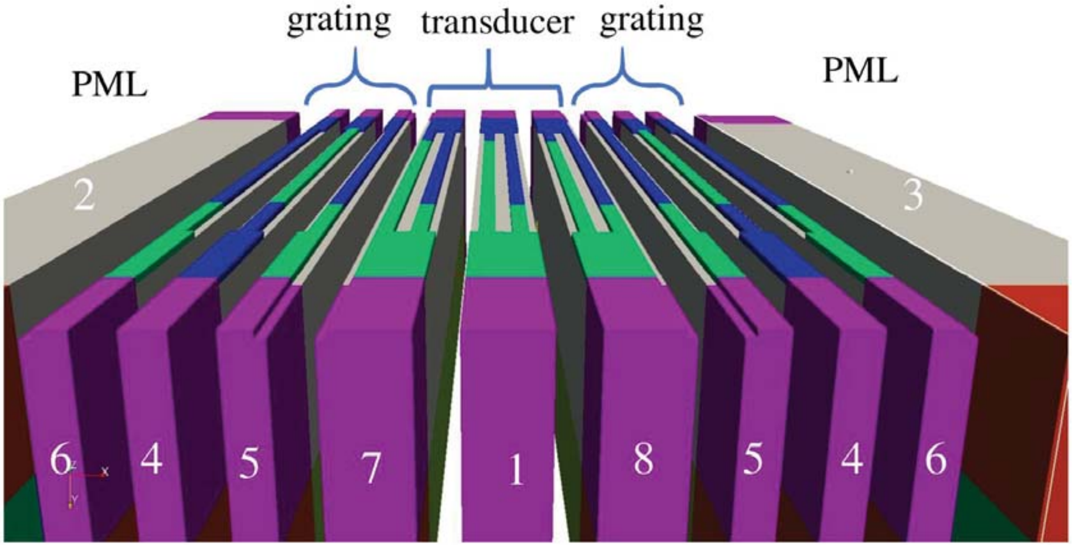

Figure 4.3: Organizational structure of hierarchical cascading full 3D SAW model in Marc Solal's research (cited from Ref. [90]).

As mentioned in Section 2.3, the proposed mirror cascading changes the rule of setting a hierarchical cascading tree. Use of symmetric properties in every layer is important for saving simulation time. In this work, the FEM model of unit cells for full 3D SAW simulation is demonstrated in Figure 4.4. Here, PML is selected as surrounding absorbers instead of ILDB. It is because building ILDB for a large surface is not an easy task. Utilization of mirror cascading is maximized during the model design. The slice width to the x direction is uniform for all regions as $\lambda/4$. Therefore, all slices to be cascaded share the same ***B*** matrix. Meanwhile, the mirror cascading is applied to the substrate region for both x and y directions. Five kinds of basic unit cells are enough to assemble the core structure. Units A, B, C and D are shown in Figure 4.5, and one more unit for PML at the ends (see Figure 4.2).

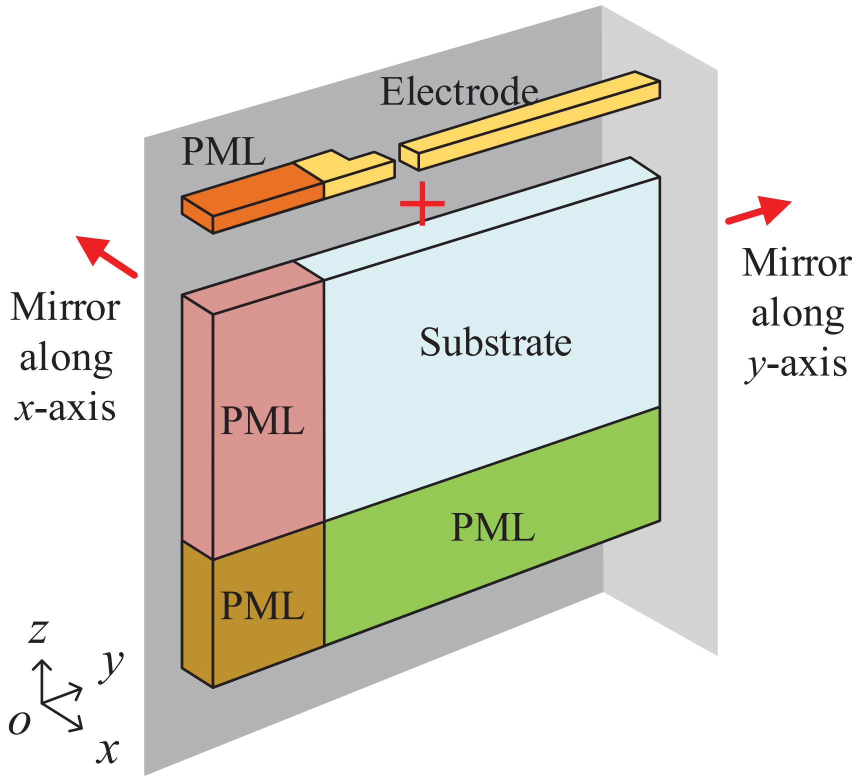

Figure 4.4: Unit cell used in this full 3D hierarchical cascading SAW device.

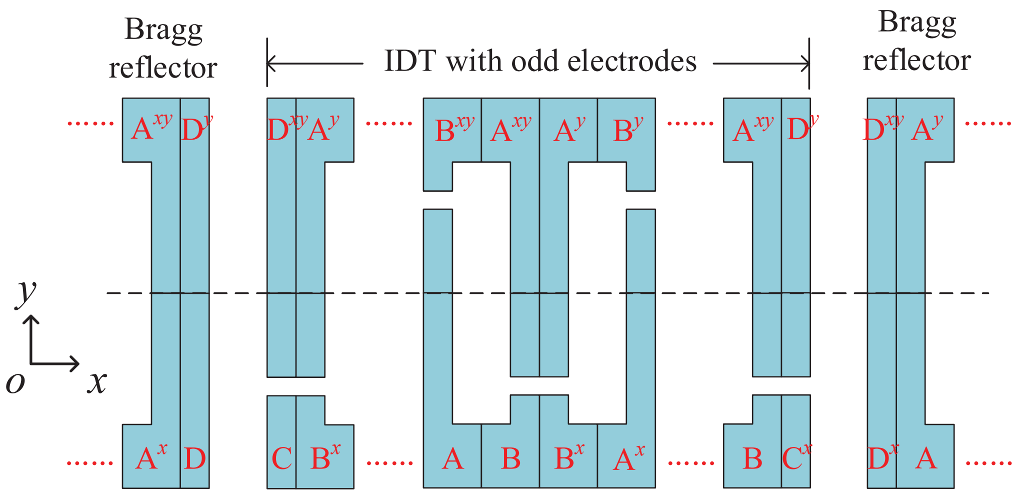

Figure 4.5: Cascading tree for a 3D Symmetrical SAW Model.

4.3.2 Simulation of Synchronous Resonators

First, $N_{\rm IDT}$ and $N_{\rm Bragg}$ were set at 5 and 2, respectively. Results obtained by the CPU/GPGPU-based HCT and traditional FEM were compared. Although $N_{\rm IDT}$ and $N_{\rm Bragg}$ are so small, total DOFs are more than 0.9 million, which is almost the upper limit for the traditional FEM in workstation.

Table 4.3 compares the required memory size and computation time. In this case, the time consumption of CPU-HCT is even longer than that of the traditional FEM because the cascading time is small. However, GPGPU-HCT enables to reduce these values significantly even though $N_{\rm IDT}$ and $N_{\rm Bragg}$ are small. Of course, the obtained frequency responses by these methods are identical till 14th decimal place. This indicates that errors caused by the hierarchical cascading are negligible.

Table 4.3: Simulation result of FEM model with and without GPGPU based HCT.

Method	Without HCT	CPU-HCT	GPGPU-HCT
Time	745 s	1000 s	133 s
Memory	110 GB	30 GB	2 GB(CPU)+28 GB(GPGPU)

Next, $N_{\rm IDT}$ and $N_{\rm Bragg}$ were set at 257 and 33, respectively. In this case, the traditional FEM is not applicable due to the required memory size. Figure 4.6 show the simulated responses obtained for the resonators with different values of l_g. In addition to main and various spurious responses, the influence of lateral leakage is seen. The result coincides well with previously published experimental results [112]. Although the number of DOFs reached 30 million, the computational time was 153 sec. for one frequency point, which is only 20 sec. longer than the value shown in Table 4.3. Note that more than 20 min. is necessary if GPGPU is not used.

Figure 4.7 and Figure 4.8 show the calculated shear horizontal component of three cross-sections (A-A’, B-B’ and C-C’ in Figure 4.2) at 630 MHz and 642 MHz. We can identify them as the 3rd-order longitudinal mode and 5th-order transverse mode, respectively, from the field distributions. It is seen that SAW energy is well confined in the IDT region at 630 MHz (Figure 4.7(c)). On the other hand, lateral leakage and

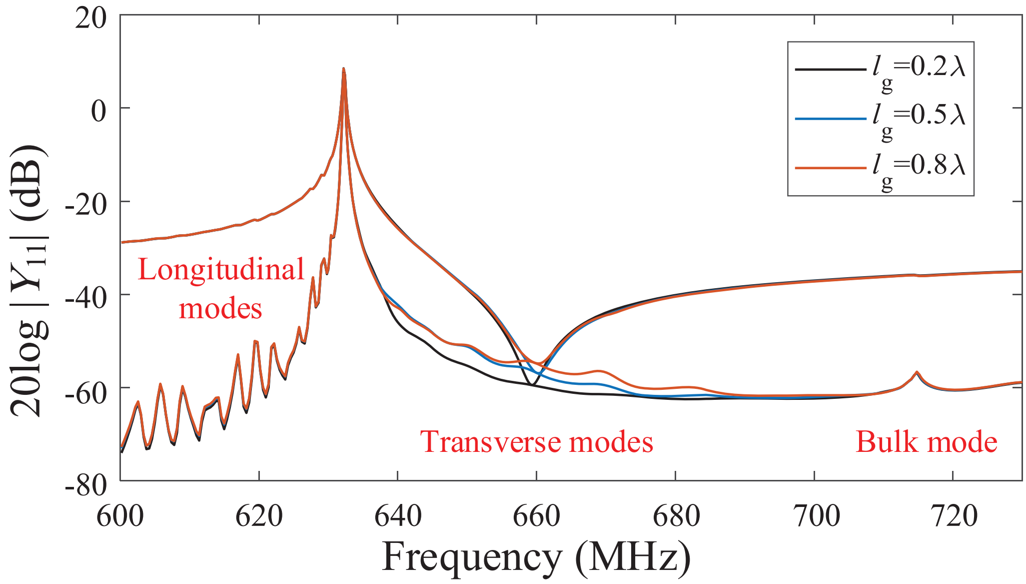

Figure 4.6: Simulated Y_{11} curves of SAW synchronous resonators.

transverse mode pattern are clearly seen in Figure 4.8(c).

4.3.3 Wavenumber Domain Analysis

Figure 4.9 shows the spectrum in the wavenumber (β_x, β_y) domain obtained by the 2-D FFT of the calculated field distribution at 642 MHz. Bright spots exist at $(\beta_x, \beta_y) = (\pm 1.07, 0)$ [rad./μm]. They represent the contribution of the main SH SAW. There are also spots at $(\beta_x, \beta_y) = (\pm 1.07, \pm 0.4)$ [rad./μm]. They represent lateral propagation of the Rayleigh SAW coupled with the SH SAW.

Two elliptic traces are seen in Figure 4.9(a). They represent scattered wave components [113]. Their velocities coincide well with calculated velocities of uncoupled bulk acoustic waves along the top surface as marked in Figure 4.9(b). The inner one is due to the longitudinal BAW in 42-LT while the outer one is due to the shear BAWs. Note velocities of shear horizontal (SH) and shear vertical (SV) BAWs are close to each other in 42-LT, and their traces are overlapped. It is clear that multiple waves are coupled around $\beta_x = \pm 1.07$ [rad./μm]. This makes it difficult to distinguish their complex influence.

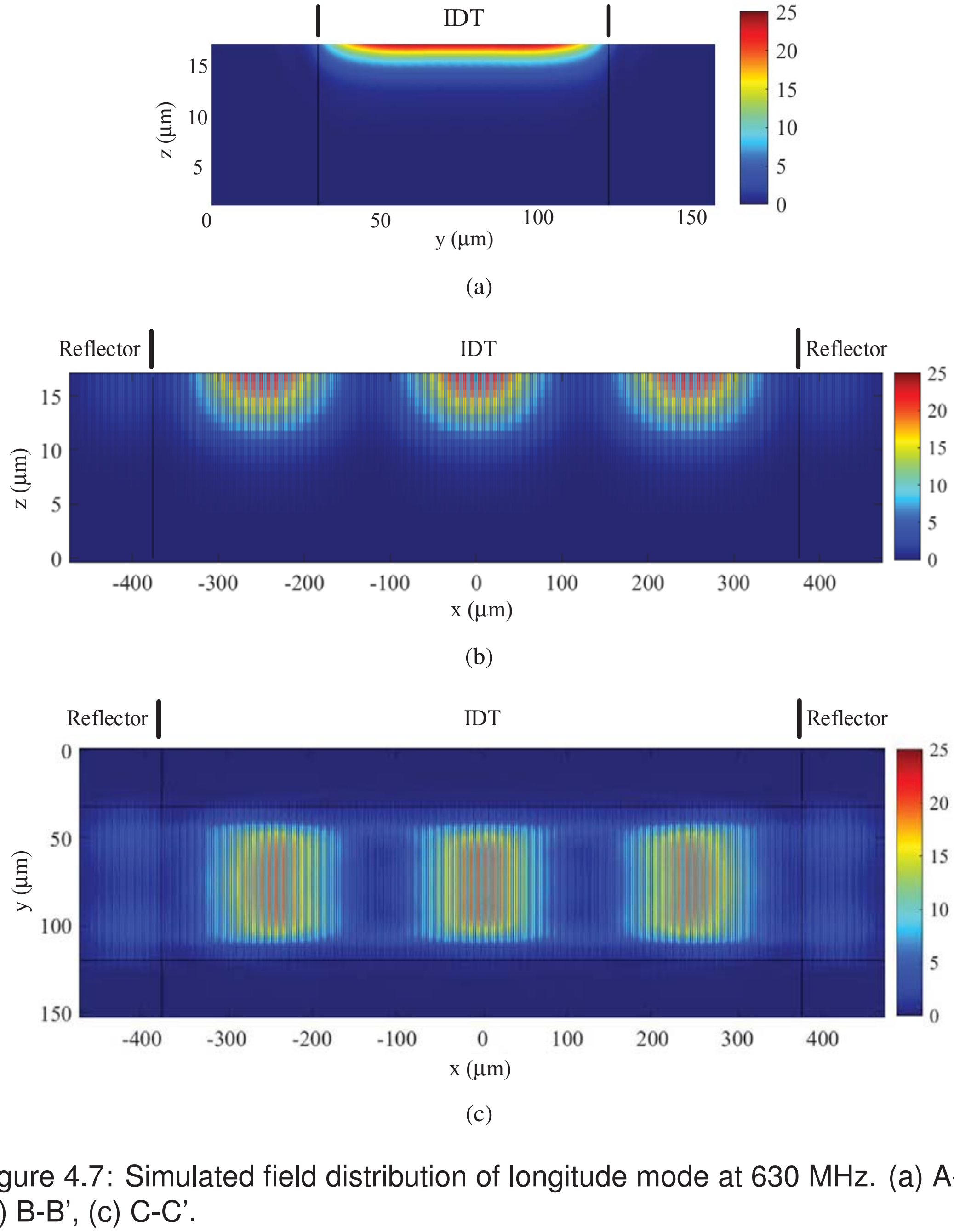

Figure 4.7: Simulated field distribution of longitude mode at 630 MHz. (a) A-A', (b) B-B', (c) C-C'.

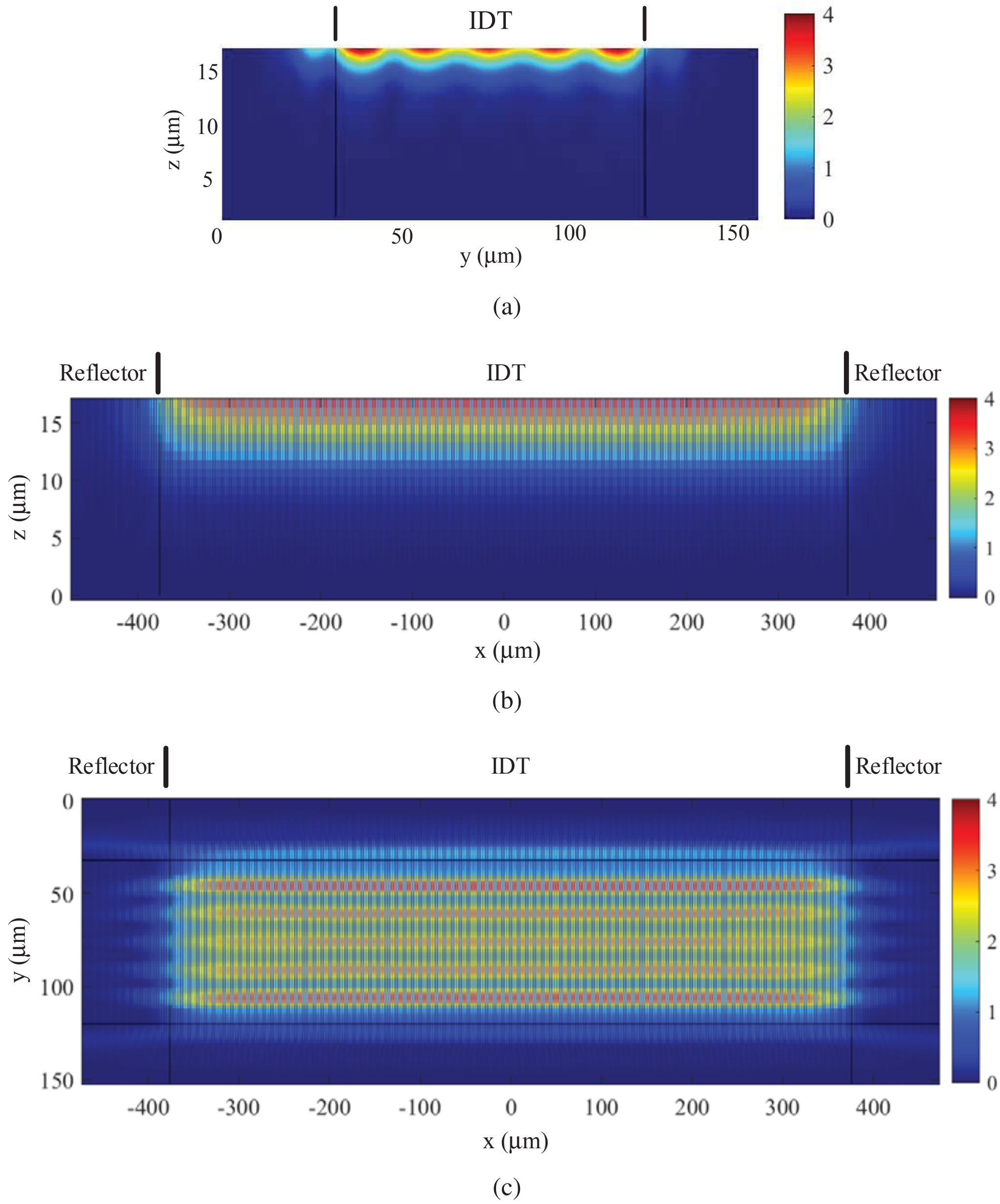

Figure 4.8: Simulated field distribution of transverse mode at 642 MHz. (a) A-A', (b) B-B', (c) C-C'.

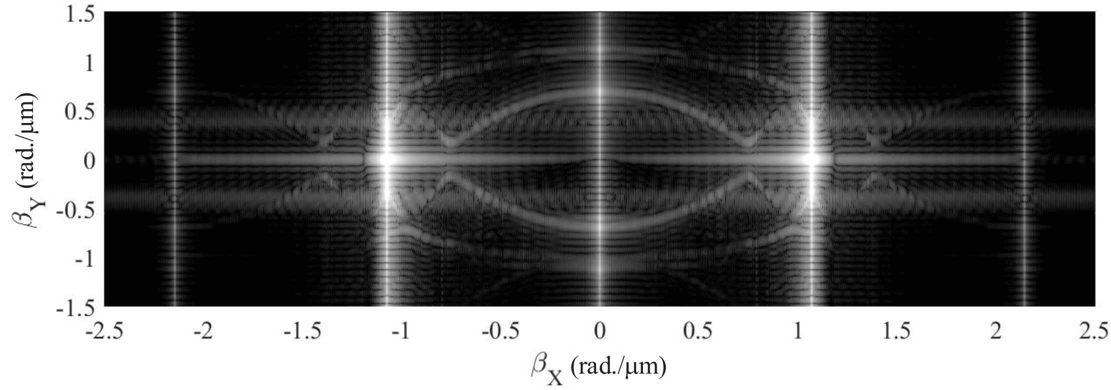

(a)

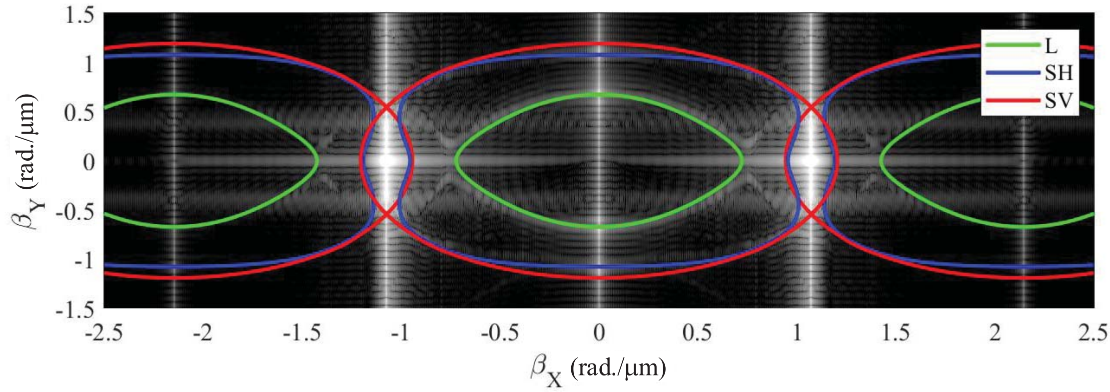

(b)

Figure 4.9: Simulated field distribution in (β_x, β_y) domain at 642 MHz. (a) Original one, (b) BAWs marked.

Next, numerical data around the inner oval are extracted, the inverse 2D FFT is applied. [113, 114] Figure 4.10 shown the result. It is clearly seen that the scattering is caused at the junctions between busbars of the IDT and those of Bragg reflectors. This scattering may be one of the remaining loss mechanisms in current high-performance SAW devices. [44]

4.4 Conclusion

This chapter demonstrated the full 3D simulation of SAW devices. Use of GPGPU allowed us to reduce the required computational time significantly, and made the full 3D

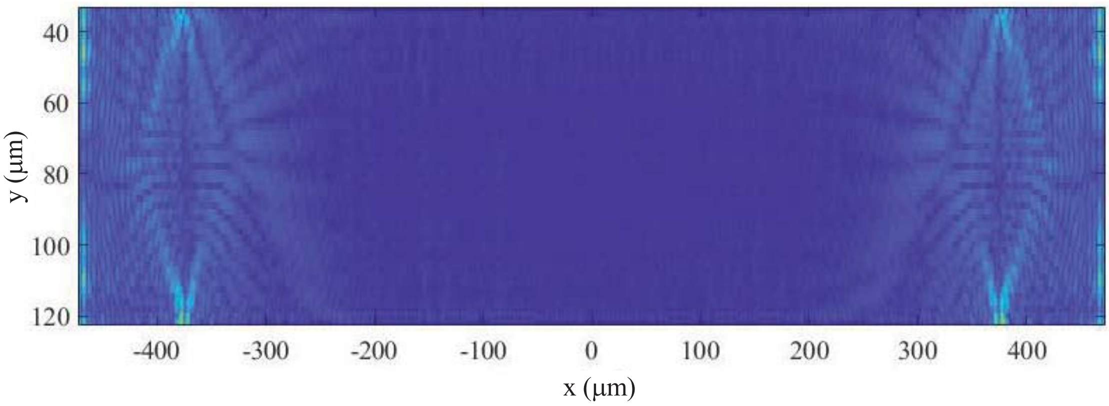

Figure 4.10: Field distribution of the inner circle after IFFT.

simulation practical. It was shown that proper design of the cascading tree is essential for accelerating the simulation speed. Fast FEM simulation was demonstrated by the use of GPGPU and HCT for a full 3D SAW resonator including 30 million DOFs. From the obtained field distribution, various information such as type and characteristics of the spurious signal and the source of energy leakage were obtained.

Chapter 5

Conclusion and Outlook

5.1 Conclusion

In this thesis, the HCT-based FEM simulation was extended, and the modification of HCT and new extended simulation models can be concluded as the following.

First, a brief introduction of SAW/BAW technologies and their current status were given in Chapter 1. It was revealed why fast and accurate simulation tools are important in SAW/BAW device design. Then, several problems in SAW/BAW FEM simulation were discussed. It was expected that HCT could solve these problems after some extension.

In chapter 2, the basics of the HCT calculation was introduced. Then, the new cascading method of mirror cascading was proposed. This cascading was at least two times faster than the original, and applicable for symmetrical structures. HCT was implemented by using Matlab and COMSOL as the platform. The experiments showed high-speed HCT-FEM simulation could be obtained easily in this way.

In chapter 3, ILDB was proposed as a new boundary condition for infinite region simulation with a better absorbing performance than PML. It was demonstrated the simulation of large TWS model could be finished in a short time when HCT and ILDB were implemented. Utilizing this accelerated TWS model, scattering behaviors at discontinuity could be easily solved for both BAWs and SAWs in a fast speed. The obtained simulation data helped us to mathematically model these problems.

In chapter 4, GPGPU was introduced to boost HCT-FEM simulation of practical 3D SAW device. More than ten times faster calculation speed was achieved. With the help of GPGPU, simulation of extremely large full 3D SAW model was quickly realized in a workstation. The obtained electrical frequency response included all kinds of effects in the SAW device. Moreover, the obtained displacement field was quite helpful in diagnosing spurious peaks and scattering in SAW devices.

5.2 Outlook

HCT is applied successfully in accelerating the FEM simulation of SAW/BAW devices in this thesis. But its application should not be limited in SAW/BAW FEM simulation. It is expected that researchers of other fields could catch this powerful technology and let HCT make a greater contribution.

As for the next step, the model will be applied for the tilted SAW device design. It is known that transverse modes can be suppressed when gratings are placed in a particular angle. However, the research about the optimal angle value is little. All behavior models we have now are not applicable to calculate the influence brings by this angle. The full 3D SAW simulation might bring some information on the impact of the tilted angle.

Besides, a new energy loss mechanisms was found in this work. Its suppression will offer further enhancement of device performances. GPGPU based HCT can be a powerful tool for analyzing and understanding its behavior, and also finding out the best solution.

References

[1] Cerwall Patrik, Jonsson Peter, and Carson Stephen. Ericsson mobility report. Technical report, Ericsson, 2015.

[2] Boyd Bangerter, Shilpa Talwar, Reza Arefi, and Ken Stewart. Networks and devices for the 5G era. *IEEE Communications Magazine*, 52(2):90–96, 2014.

[3] Mamta Agiwal, Abhishek Roy, and Navrati Saxena. Next generation 5G wireless networks: A comprehensive survey. *IEEE Communications Surveys & Tutorials*, 18(3):1617–1655, 2016.

[4] Youngsun Kwon, Duk Kyu Park, and Hongjai Rhee. Spectrum fragmentation: Causes, measures and applications. *Telecommunications Policy*, 41(5):447–459, 2017.

[5] Steven Mahon. The 5G effect on RF filter technologies. *IEEE Transactions on Semiconductor Manufacturing*, 30(4):494–499, 2017.

[6] Clemens CW Ruppel. Acoustic wave filter technology-a review. *IEEE Transactions on Ultrasonics, Ferroelectrics, and Frequency Control*, 64(9):1390–1400, 2017.

[7] Gernot Fattinger, Paul Stokes, Vishwavasu Potdar, Alexandre Volatier, Fabien Dumont, and Robert Aigner. Miniaturization of BAW devices and the impact of wafer level packaging technology. In *Proceedings of IEEE International Ultrasonics Symposium*, pages 228–231. IEEE, 2013.

[8] Lord Rayleigh. On waves propagated along the plane surface of an elastic solid. *Proceedings of the London Mathematical Society*, 1(1):4–11, 1885.

[9] RM White and FW Voltmer. Direct piezoelectric coupling to surface elastic waves. *Applied Physics Letters*, 7(12):314–316, 1965.

[10] MF Lewis, CL West, JM Deacon, and RF Humphryes. Recent developments in SAW devices. *IEE Proceedings A (Physical Science, Measurement and Instrumentation, Management and Education, Reviews)*, 131(4):186–215, 1984.

[11] Kerstin Länge, Bastian E Rapp, and Michael Rapp. Surface acoustic wave biosensors: a review. *Analytical and Bioanalytical Chemistry*, 391(5):1509–1519, 2008.

[12] Victor P Plessky and Leonhard M Reindl. Review on SAW RFID tags. *IEEE Transactions on Ultrasonics, Ferroelectrics, and Frequency Control*, 57(3):654–668, 2010.

[13] Clemens CW Ruppel, Roland Dill, Alice Fischerauer, Gerhard Fischerauer, Waldemar Gawlik, Jiirgen Machui, Folkhard Muller, Leonhard Reindl, Werner Ruile, Gerd Scholl, et al. SAW devices for consumer communication applications. *IEEE Transactions on Ultrasonics, Ferroelectrics, and Frequency Control*, 40(5):438–452, 1993.

[14] Alfred Pohl. A review of wireless SAW sensors. *IEEE Transactions on Ultrasonics, Ferroelectrics, and Frequency Control*, 47(2):317–332, 2000.

[15] Ken-ya Hashimoto, Hiroki Asano, Kenji Matsuda, Naofumi Yokoyama, Tatsuya Omori, and Masatsune Yamaguchi. Wideband Love wave filters operating in GHz range on Cu-grating/rotated-YX-$LiNbO_3$-substrate structure. In *Proceedings of IEEE International Ultrasonics Symposium*, volume 2, pages 1330–1334. IEEE, 2004.

[16] K-Y Hashimoto, Masatsune Yamaguchi, S Mineyoshi, O Kawachi, M Ueda, and G Endoh. Optimum leaky-SAW cut of $LiTaO_3$ for minimised insertion loss devices. In *Proceedings of IEEE International Ultrasonics Symposium*, volume 1, pages 245–254. IEEE, 1997.

[17] CS Lam, Chris YJ Wang, and SM Wang. A review of the recent development of temperature stable cuts of quartz for SAW applications. In *Proceedings of the Fourth International Symposium on Acoustic Wave Devices for Future Mobile Communication Systems*, pages 3–5, 2010.

[18] KM Lakin and JS Wang. UHF composite bulk wave resonators. In *Proceedings of IEEE International Ultrasonics Symposium*, pages 834–837. IEEE, 1980.

[19] Kiyoshi Nakamura, Hiromasa Sasaki, and Hiroshi Shimizu. A piezoelectric composite resonator consisting of a ZnO film on an anisotropically etched silicon substrate. *Japanese Journal of Applied Physics*, 20(S3):111, 1981.

[20] TW Grudkowski, JF Black, TM Reeder, DE Cullen, and RA Wagner. Fundamental-mode VHF/UHF minature acoustic resonators and filters on silicon. *Applied Physics Letters*, 37(11):993–995, 1980.

[21] Richard C Ruby, Paul Bradley, Yury Oshmyansky, Allen Chien, and JD Larson. Thin film bulk wave acoustic resonators (FBAR) for wireless applications. In *Proceedings of IEEE International Ultrasonics Symposium*, volume 1, pages 813–821. IEEE, 2001.

[22] Rich Ruby. Review and comparison of bulk acoustic wave FBAR, SMR technology. In *Proceedings of IEEE International Ultrasonics Symposium*, pages 1029–1040. IEEE, 2007.

[23] Rich Ruby, Martha Small, Frank Bi, Don Lee, Lori Callaghan, Reed Parker, and Steve Ortiz. Positioning FBAR technology in the frequency and timing domain. *IEEE Transactions on Ultrasonics, Ferroelectrics, and Frequency Control*, 59(3):334–345, 2012.

[24] Kenneth M Lakin, Gerald R Kline, and Kevin T McCarron. Development of miniature filters for wireless applications. *IEEE Transactions on Microwave Theory and Techniques*, 43(12):2933–2939, 1995.

[25] KM Lakin, KT McCarron, and RE Rose. Solidly mounted resonators and filters. In *Proceedings of IEEE International Ultrasonics Symposium*, volume 2, pages 905–908. IEEE, 1995.

[26] Sumy Jose, Andre BM Jansman, Raymond JE Hueting, and Jurriaan Schmitz. Optimized reflector stacks for solidly mounted bulk acoustic wave resonators. *IEEE Transactions on Ultrasonics, Ferroelectrics, and Frequency Control*, 57(12):2753–2763, 2010.

[27] Robert Aigner. MEMS in RF-filter applications: thin film bulk-acoustic-wave technology. In *Proceedings of the 13th International Conference on Solid-State Sensors, Actuators and Microsystems*, volume 1, pages 5–8. IEEE, 2005.

[28] J Kaitila. Review of wave propagation in BAW thin film devices-progress and prospects. In *Proceedings of IEEE International Ultrasonics Symposium*, pages 120–129. IEEE, 2007.

[29] Tsuyoshi Yokoyama, Yoshiki Iwazaki, Yosuke Onda, Tokihiro Nishihara, Yuichi Sasajima, and Masanori Ueda. Highly piezoelectric co-doped AlN thin films for wideband FBAR applications. *IEEE Transactions on Ultrasonics, Ferroelectrics, and Frequency Control*, 62(6):1007–1015, 2015.

[30] KM Lakin, J Belsick, JF McDonald, and KT McCarron. Improved bulk wave resonator coupling coefficient for wide bandwidth filters. In *Proceedings of IEEE International Ultrasonics Symposium*, volume 1, pages 827–831. IEEE, 2001.

[31] T Yokoyama, T Nishihara, S Taniguchi, M Iwaki, Y Satoh, M Ueda, and T Miyashita. New electrode material for low-loss and high-Q FBAR filters. In *Proceedings of IEEE International Ultrasonics Symposium*, volume 1, pages 429–432. IEEE, 2004.

[32] Ken-ya Hashimoto. Advances in RF SAW devices: What are demanded? In *Proceedings of European Frequency and Time Forum*. IEEE, 2016. DOI:10.1109/EFTF.2016.7477761.

[33] R Aigner and G Fattinger. Pushing BAW beyond 'known' Frontiers: Higher, Wider, Smaller, Cooler. In *Proceedings of the Seventh International Symposium on Acoustic Wave Devices for Future Mobile Communication Systems*, 2018.

[34] KC Wagner, T Bauer, K Morozumi, E Avci, and C Eggs. New Generation of High-Performance TC-SAW Components for Module Integration. In *Proceedings of the Sixth International Symposium on Acoustic Wave Devices for Future Mobile Communication Systems*, pages 62–66, 2015.

[35] Robert Aigner. Filter technologies for converged RF-frontend architectures: SAW, BAW and beyond. In *Proceedings of Topical Meeting on Silicon Monolithic Integrated Circuits in RF Systems*, pages 136–139. IEEE, 2010.

[36] F Rosednbaum Joel. *Bulk Acoustic Wave Theory and Devices*. Artech House, London, 1988. p.397.

[37] Jun Tsutsumi, Masafumi Iwaki, Yasuhide Iwamoto, Tsuyoshi Yokoyama, Takeshi Sakashita, Tokihiro Nishihara, Masanori Ueda, and Yoshio Satoh. A miniatuirized FBAR duplexer with reduced acoustic loss for the W-CDMA applicaion. In *Proceedings of IEEE International Ultrasonics Symposium*, volume 1, pages 93–96. IEEE, 2005.

[38] Ryoichi Ohara, Naoko Yanase, Takaaki Yasumoto, Minoru Kawase, Shingo Masuko, Tetsuya Ohno, and Kenya Sano. uppression of Acoustic Energy Leakage in FBARs with Al Bottom Electrode: FEM Simulation and Experimental Results. In *Proceedings of IEEE International Ultrasonics Symposium*, pages 1657–1660. IEEE, 2007.

[39] Ngoc Nguyen, Agne Johannessen, Stig Rooth, and Ulrik Hanke. A Design Approach for High-Q FBARs With a Dual-Step Frame. *IEEE Transactions on Ultrasonics, Ferroelectrics, and Frequency Control*, 65(9):1717–1725, 2018.

[40] Olli Holmgren, Tapani Makkonen, Jouni V Knuuttila, Mikko Kalo, Victor P Plessky, and William Steichen. Side radiation of Rayleigh waves from synchronous SAW resonators. *IEEE Transactions on Ultrasonics Ferroelectrics and Frequency Control*, 54(4):861, 2007.

[41] Shogo Inoue, Kentaro Nakamura, Hidetaro Nakazawa, Jun Tsutsumi, Masanori Ueda, and Yoshio Satoh. Analysis of Rayleigh wave radiations from leaky SAW resonators. In *Proceedings of IEEE International Ultrasonics Symposium*, pages 1953–1956. IEEE, 2013.

[42] H Nakamura, T Komatsu, H Nakanishi, T Tsurunari, and J Fujiwara. Reduction of transverse leakage for SAW resonators on $LiTaO_3$ substrate. In *Proceedings of IEEE International Ultrasonics Symposium*, pages 1248–1251. IEEE, 2012.

[43] B Abbott, R Aigner, A Chen, K Gamble, T Kook, J Kuypers, M Solal, and K Steiner. High Q TCSAW. In *Proceedings of the Sixth International Symposium on Acoustic Wave Devices for Future Mobile Communication Systems*, 2015.

[44] Tsutomu Takai, Hideki Iwamoto, Yuichi Takamine, Toshiyuki Fuyutsume, Takeshi Nakao, Masahiro Hiramoto, Takanori Toi, and Masayoshi Koshino. I.H.P. SAW technology and its application to microacoustic components. In *Proceedings of IEEE International Ultrasonics Symposium*. IEEE, 2017. DOI:10.1109/ULTSYM.2017.8091876.

[45] Ken-ya Hashimoto. *RF bulk acoustic wave filters for communications*. Artech House, 2009.

[46] Ken-ya Hashimoto. *Surface acoustic wave devices in telecommunications*. Springer, 2000.

[47] J Kaitila, M Ylilammi, Juha Ella, and R Aigner. Spurious resonance free bulk acoustic wave resonators. In *Proceedings of IEEE International Ultrasonics Symposium*, volume 1, pages 84–87. IEEE, 2003.

[48] Xinyi Li, Jingfu Bao, Yulin Huang, Benfeng Zhang, Gongbin Tang, Tatsuya Omori, and Ken-ya Hashimoto. Use of double-raised-border structure for quality factor enhancement of type II piston mode FBAR. *Microsystem Technologies*, 24(7):2991–2997, 2018.

[49] M Solal, J Gratier, R Aigner, K Gamble, B Abbott, T Kook, A Chen, and K Steiner. Transverse modes suppression and loss reduction for buried electrodes SAW devices. In *Proceedings of IEEE International Ultrasonics Symposium*, pages 624–628. IEEE, 2010.

[50] Hiroyuki Nakamura, Hidekazu Nakanishi, Rei Goto, and Ken-ya Hashimoto. Suppression of transverse-mode spurious responses for SAW resonators on SiO_2/Al/$LiNbO_3$ structure by selective removal of SiO_2. *IEEE Transactions on Ultrasonics, Ferroelectrics, and Frequency Control*, 58(10):2188–2193, 2011.

[51] Benfeng Zhang, Tao Han, Gongbin Tang, Xinyi Li, Yulin Huang, Tatsuya Omori, and Ken-ya Hashimoto. Impact of coupling between multiple SAW modes on piston mode operation of SAW resonators. *IEEE Transactions on Ultrasonics, Ferroelectrics, and Frequency Control*, 65(6):1062–1068, 2018.

[52] Ken-ya Hashimoto, Xinyi Li, Jingfu Bao, Yulin Huang, Benfeng Zhang, and Tao Han. Impact of Two Wave Coupling in Temperature Compensated Surface Acoustic Wave Devices. In *Proceedings of the Seventh International Symposium on Acoustic Wave Devices for Future Mobile Communication Systems*, 2018.

[53] SA Wilkus, CS Hartmann, and RJ Kansy. Transverse mode compensation of surface acoustic wave filters. In *Proceedings of IEEE International Ultrasonics Symposium*, pages 43–47. IEEE, 1985.

[54] R Ruby, J Larson, C Feng, and S Fazzio. The effect of perimeter geometry on FBAR resonator electrical performance. In *Proceedings of MTT-S International Microwave Symposium Digest*, pages 217–221, 2005.

[55] A Link, E Schmidhammer, H Heinze, M Mayer, M Schmiedgen, B Bader, K Wagner, and R Weigel. Suppression of spurious modes in mirror-type thin film BAW resonators using an appropriate shape of the active area. In *Proceedings of IEEE International Ultrasonics Symposium*, volume 2, pages 1179–1182. IEEE, 2005.

[56] Hideki Iwamoto, Tsutomu Takai, Yuichi Takamine, Takeshi Nakao, Toshiyuki Fuyutsume, and Masayoshi Koshino. Transverse Modes in IHP SAW Resonator and Their Suppression Method. In *Proceedings of IEEE International Ultrasonics Symposium*. IEEE, 2018. DOI:10.1109/ULTSYM.2018.8580175.

[57] Satoru Matsuda, Michio Miura, Takashi Matsuda, Masanori Ueda, Yoshio Satoh, and Ken-ya Hashimoto. Experimental studies of quality factor deterioration in shear-horizontal-type surface acoustic wave resonators caused by apodization of interdigital transducer. *Japanese Journal of Applied Physics*, 50(7S):07HD14, 2011.

[58] Victor Plessky and Julius Koskela. Coupling-of-modes analysis of SAW devices. *International Journal of High Speed Electronics and Systems*, 10(04):867–947, 2000.

[59] Ken-ya Hashimoto and H Yamaguchi. General-purpose simulator for leaky surface acoustic wave devices based on coupling-of-modes theory. In *Proceeding of IEEE International Ultrasonics Symposium*, pages 117–122, 1996.

[60] Benjamin P Abbott and Ken-ya Hashimoto. A coupling-of-modes formalism for surface transverse wave devices. In *Proceeding of IEEE International Ultrasonics Symposium*, pages 239–245, 1995.

[61] W. P. Mason. *Physical Acoustics*, volume 1A. Academic Press, 1964. pp. 335-416.

[62] Tiberiu Jamneala, Paul Bradley, Uli B Koelle, and Allen Chien. Modified Mason model for bulk acoustic wave resonators. *IEEE Transactions on Ultrasonics, Ferroelectrics, and Frequency Control*, 55(9):2025–2029, 2008.

[63] M. Koshiba and K. Ohbuchi. An analysis of Surface-Acoustic-Wave devices using coupling-of-mode theory and Finite-Element Method. *Japanese Journal of Applied Physics*, 34(Suppl. 30-1):140–142, 1991.

[64] Tapani Makkonen, Antti Holappa, and Martti M Salomaa. 3D FEM modeling of composite BAW resonators. In *Proceedings of IEEE International Ultrasonics Symposium*, volume 1, pages 893–896. IEEE, 2000.

[65] G. Endoh, K. Hashimoto, and M. Yamaguchi. SAW propagation characterisation by finite element method and spectral domain analysis. *Japanese Journal of Applied Physics*, 34(5B):2638–2641, 1995.

[66] P. Ventura, J.M. Hodé, and B. Lopez. Rigorous analysis of finite SAW devices with arbitrary electrode geometries. In *Proceeding of IEEE International Ultrasonics Symposium*, pages 257–262, 1995.

[67] T. Nakao, M. Kadota, K. Nishiyama, Y. Nakai, D. Yamamoto, Y. Ishiura, T. Komura, N. Takada, and R. Kita. Smaller surface acoustic wave duplexer for US personal communication service having good temperature characteristics. *Japanese Journal of Applied Physics*, 46:4760–4763, 2005.

[68] T. Takai, Y. Takamine, H. Yamazaki, T. Fuyutsume, H. Kyoya, T. Nakao, H. Kando, M. Hiramoto, T. Toi, M. Koshino, and N. Nakajima. High-performance SAW resonator on new multilayered substrate using $LiTaO_3$ crystal. *IEEE Transactions on Ultrasonics, Ferroelectrics, and Frequency Control*, 64(9):1382–13898, 2017.

[69] T. Kimura, Y. Kishimoto, M. Omura, and K. Hashimoto. 3.5 GHz longitudinal leaky surface acoustic wave resonator using a multilayered waveguide structure for high acoustic confinement. *Japanese Journal of Applied Physics*, 57(7S1, 07LD15), 2018.

[70] Robert K Thalhammer and John D Larson. Finite-Element Analysis of Bulk-Acoustic-Wave Devices: A Review of Model Setup and Applications. *IEEE Transactions on Ultrasonics, Ferroelectrics, and Frequency Control*, 63(10):1624–1635, 2016.

[71] Xinyi Li, Jingfu Bao, Yulin Huang, Benfeng Zhang, Tatsuya Omori, and Ken-ya Hashimoto. Traveling wave excitation for FEM simulation of RF SAW/BAW devices. In *Proceedings of IEEE International Ultrasonics Symposium*. IEEE, 2017. DOI:10.1109/ULTSYM.2017.8092845.

[72] Florian Thalmayr, Ken-ya Hashimoto, Tatsuya Omori, and Masatsune Yamaguchi. Frequency domain analysis of lamb wave scattering and application to film bulk acoustic wave resonators. *IEEE Transactions on Ultrasonics, Ferroelectrics, and Frequency Control*, 57(7):1641–1648, 2010.

[73] U Vogel, M Spindler, A Winkler, and T Gemming. Calculation of Surface Acoustic Waves on a Piezoelectric Substrate using Amazon Cloud Computing. In *Proceedings of the 2015 COMSOL Conference*, 2015.

[74] Bilel Achour, Nadia Aloui, Najla Fourati, Chouki Zerrouki, and Nourdin Yaakoubi. Modelling and simulation of SAW delay line sensors with COMSOL Multiphysics. In *Proceedings of International Conference on Multidisciplinary Sciences*, 2018.

[75] Jean-Pierre Berenger. A perfectly matched layer for the absorption of electromagnetic waves. *Journal of Computational Physics*, 114(2):185–200, 1994.

[76] Frank D Hastings, John B Schneider, and Shira L Broschat. Application of the perfectly matched layer (PML) absorbing boundary condition to elastic wave propagation. *The Journal of the Acoustical Society of America*, 100(5):3061–3069, 1996.

[77] COMSOL Inc. *COMSOL Multiphysics Reference Manual*, 2018. Version 5.3a.

[78] B A Auld. *Acoustic waves and fields in solids*. New York: Wileyand Sons, 1973.

[79] V Plessky, J Koskela, and Seong Su Hong. Leaky Wave Cuts of $LiNbO_3$ and $LiTaO_3$ with Minimized Propagation Loss Due to Thin Layer. In *Proceeding of IEEE International Ultrasonics Symposium*. IEEE, 2006. DOI:10.1109/ULTSYM.2006.382.

[80] Osamu Kawachi, Seiichi Mitobe, Motoyuki Tajima, Shogo Inoue, and Ken-ya Hashimoto. Low-loss and wide-band double-mode surface acoustic wave filters using pitch-modulated interdigital transducers and reflectors. *IEEE Transactions on Ultrasonics, Ferroelectrics, and Frequency Control*, 54(10):2159–2164, 2007.

[81] Takao Morita, Yoshitaka Watanabe, Masaki Tanaka, and Yuzo Nakazawa. Wideband low loss double mode SAW filters. In *Proceeding of IEEE International Ultrasonics Symposium*, pages 95–104. IEEE, 1992.

[82] Ken-ya Hashimoto, Tatsuya Omori, and Masatsune Yamaguchi. Operation mechanism of double-mode surface acoustic wave filters with pitch-modulated IDTs and reflectors. *IEEE Transactions on Ultrasonics, Ferroelectrics, and Frequency Control*, 54(10):2152–2158, 2007.

[83] Yasunori Sakamoto, Ken-ya Hashimoto, and Masatsune Yamaguchi. Behaviour of leaky surface acoustic wave propagation at discontinuous region of periodic grating. *Japanese Journal of Applied Physics*, 37(5S):2905, 1998.

[84] M Pereira da Cunha and Eric L Adler. Scattering of SAW at discontinuities: Some numerical experiments. *IEEE Transactions on Ultrasonics, Ferroelectrics, and Frequency Control*, 42(2):168–173, 1995.

[85] Colin K Campbell. Longitudinal-mode leaky SAW resonator filters on 64°/YX lithium niobate. *IEEE Transactions on Ultrasonics, Ferroelectrics, and Frequency Control*, 42(5):883–888, 1995.

[86] J Koskela, P Maniadis, BA Willemsen, PJ Turner, RB Hammond, NO Fenzi, and V Plessky. Hierarchical cascading in 2D FEM simulation of finite SAW devices with periodic block structure. In *Proceedings of IEEE International Ultrasonics Symposium*. IEEE, 2016. DOI:10.1109/ULTSYM.2016.7728574.

[87] Manfred Hofer, Norman Finger, Gunter Kovacs, Joachim Schoberl, Sabine Zaglmayr, Ulrich Langer, and Reinhard Lerch. Finite-element simulation of wave propagation in periodic piezoelectric SAW structures. *IEEE Transactions on Ultrasonics, Ferroelectrics, and Frequency Control*, 53(6):1192–1201, 2006.

[88] Julius Koskela, Victor Plessky, Balam Willemsen, Patrick Turner, Bob Hammond, and Neal Fenzi. Hierarchical Cascading Algorithm for 2-D FEM Simulation of Finite SAW Devices. *IEEE Transactions on Ultrasonics, Ferroelectrics, and Frequency Control*, 65(10):1933–1942, 2018.

[89] J Koskela, V Plessky, P Maniadis, P Turner, and B Willemsen. Rapid 2D FEM simulation of advanced SAW devices. In *Procedings of IEEE MTT-S International Microwave Symposium*, pages 1484–1486. IEEE, 2017.

[90] Marc Solal, Mark Gallagher, and Alireza Tajic. Full 3D simulation of SAW resonators using hierarchical cascading FEM. In *Proceedings of IEEE International Ultrasonics Symposium*. IEEE, 2017. DOI:10.1109/ULTSYM.2017.8092166.

[91] Julius Koskela, Victor Plessky, Balam Willemsen, Patrick Turner, Bob Hammond, and Neal Fenzi. Hierarchical cascading algorithm for 2D FEM simulation of finite SAW devices. *IEEE Transactions on Ultrasonics, Ferroelectrics, and Frequency Control*, 2018. DOI:10.1109/TUFFC.2018.2852603.

[92] Aleksey Shimko and Victor Plessky. Fast SAW Device Simulation in COMSOL Using the Hierarchical Cascading Method. In *Proceeding of IEEE IEEE International Ultrasonics Symposium*. IEEE, 2018. DOI:10.1109/ULTSYM.2018.8579814.

[93] Victor Plessky, Julius Koskela, BA Willemsen, PJ Turner, RB Hammond, and NO Fenzi. Acoustic radiation from ends of IDT in synchronous LSAW resonators. In *Proceeding of IEEE IEEE International Ultrasonics Symposium*. IEEE, 2017. DOI:10.1109/ULTSYM.2017.8091800.

[94] Oleg V Sinkin, Ronald Holzlohner, John Zweck, and Curtis R Menyuk. Optimization of the split-step Fourier method in modeling optical-fiber communications systems. *Journal of Lightwave Technology*, 21(1):61–68, 2003.

[95] Jørgen Arendt Jensen and I Nikolov. Fast simulation of ultrasound images. In *Proceedings of IEEE International Ultrasonics Symposium*, volume 2, pages 1721–1724. IEEE, 2000.

[96] F Liu, I Turner, and M Bialkowski. A finite-Difference Time-Domain Simulation of Power Density Distribution in a Dieletric Loaded Microwave Cavity. *Journal of Microwave Power and Electromagnetic Energy*, 29(3):138–148, 1994.

[97] Gilbert Strang and George J Fix. *An analysis of the finite element method*, volume 212. Prentice-hall Englewood Cliffs, NJ, 1973.

[98] Olgierd Cecil Zienkiewicz, Robert Leroy Taylor, Olgierd Cecil Zienkiewicz, and Robert Lee Taylor. *The finite element method*, volume 36. McGraw-hill London, 1977.

[99] William BJ Zimmerman. *Multiphysics modeling with finite element methods*, volume 18. World Scientific Publishing Company, 2006.

[100] Fuzhen Zhang. *The Schur complement and its applications*, volume 4. Springer Science & Business Media, 2006.

[101] Peter Benner, Pablo Ezzatti, Enrique S Quintana-Ortí, and Alfredo Remón. Matrix inversion on CPU–GPU platforms with applications in control theory. *Concurrency and Computation: Practice and Experience*, 25(8):1170–1182, 2013.

[102] Xinyi Li, Jingfu Bao, Yulin Huang, Benfeng Zhang, Tatsuya Omori, and Ken-ya Hashimoto. Application of hierarchical cascading technique to finite element method simulation in bulk acoustic wave devices. *Japanese Journal of Applied Physics*, 57(7S1):07LC08, 2018.

[103] COMSOL Inc. *COMSOL Multiphysics LiveLink for Matlab User's Guides*, 2018. Version 5.3a.

[104] Florian Thalmayr, Ken-ya Hashimoto, Tatsuya Omori, and Masatsune Yamaguchi. Power deduction from surface fields in multilayer waveguides. *IEEE Transactions on Ultrasonics, Ferroelectrics, and Frequency Control*, 57(2):405–411, 2010.

[105] Ventsislav Yantchev, PJ Turner, S McHugh, F Iliev, T Sato, K-W Lee, and C-H Lee. Parametric study of resonant TC-SAW piston-mode configurations. In *Proceedings of IEEE International Ultrasonics Symposium*. IEEE, 2017. DOI:10.1109/ULTSYM.2017.8091695.

[106] Marc Solal, J. Gratier, R. Aigner, K. Gamble, Benjamin Abbott, T. Kook, Alan Chen, and A. Steiner. A method to reduce losses in buried electrodes RF SAW resonators. In *Proceeding of IEEE International Ultrasonics Symposium*, pages 324–332, 2011.

[107] B. Abbott, A. Chen, T. Daniel, K. Gamble, T. Kook, M. Solal, K. Steiner, R. Aigner, S. Malocha, C. Hella, M. Galiagher, and J. Kuypers. Temperature compensated SAW with high quality factor. In *Proceeding of IEEE International Ultrasonics Symposium*, 2017. DOI:10.1109/ULTSYM.2017.8092294.

[108] Ken-ya Hashimoto, Xinyi Li, Jingfu Bao, Yulin Huang, Benfeng Zhang, and Tao Han. Transverse modes in temperature compensated surface acoustic wave devices. In *Proceeding of IEEE International Ultrasonics Symposium*, 2018. DOI:10.1109/ULTSYM.2018.8580001.

[109] Gongbin Tang, Tao Han, Jin Chen, Benfeng Zhang, Tatsuya Omori, and Ken-ya Hashimoto. Model parameter extraction for obliquely propagating surface acoustic waves in infinitely long grating structures. *Japanese Journal of Applied Physics*, 55(7S1, 07KD08), 2016.

[110] Ken-ya Hashimoto. *Surface Acoustic Wave Devices in Telecommunications*. Springer Verlag, 2000. 7.1.2 COM Theory for SAW Devices.

[111] Yulin Huang, Jingfu Bao, Xinyi Li, Benfeng Zhang, Luyan Qiu, Tatsuya Omori, and Ken-Ya Hashimoto. Analysis of SAW Scattering at Discontinuity Between Periodic Gratings Using Travelling Wave Excitation and Hierarchical Cascading Technique. In *Proceeding of IEEE International Ultrasonics Symposium*. IEEE, 2018. 10.1109/ULTSYM.2018.8580141.

[112] Julius Koskela, Jouni V Knuuttila, Tapani Makkonen, Victor P Plessky, and Martti M Salomaa. Acoustic loss mechanisms in leaky SAW resonators on lithium tantalate. *IEEE Transactions on Ultrasonics, Ferroelectrics, and Frequency Control*, 48(6):1517–1526, 2001.

[113] Ken-ya Hashimoto, Hiroshi Kamizuma, Masashi Watanabe, Tatsuya Omori, and Masatsune Yamaguchi. Wavenumber domain analysis of two-dimensional SAW images captured by phase-sensitive laser probe system. *IEEE Transactions on Ultrasonics, Ferroelectrics, and Frequency Control*, 54(5):1072–1075, 2007.

[114] Ken-ya Hashimoto, Shuntaro Kawachi, Akira Takahashi, Shinya Sakamoto, and Tatsuya Omori. Laser probe system for 5 GHz SAW/BAW devices. In *Proceedings of IEEE International Frequency Control Symposium*. IEEE, 2014. DOI:10.1109/FCS.2014.6859929.

List of Publications

Scientific journals - first author

1. **Xinyi Li**, Jingfu Bao, Yulin Huang, Yuan Ling, Yingbin Zheng and Yijia Du, "A 9.45 MHz micromechanical disk resonator with movable electrodes for gap reduction", Sensors and Actuators A: Physical, 2016, 243: 66-70.

2. **Xinyi Li**, Yulin Huang, Yijia Du, Zhipeng Li, Feihong Bao and Jingfu Bao, "Study of a 10 MHz MEMS oscillator with a TPoS resonator", Sensors and Actuators A: Physical, 2017, 258: 59-67.

3. **Xinyi Li**, Jingfu Bao, Yulin Huang, Benfeng Zhang, Tatsuya Omori and Ken-ya Hashimoto, "Application of hierarchical cascading technique to finite element method simulation in bulk acoustic wave devices", Japanese Journal of Applied Physics, 2018, 57(7S1): 07LC08.

4. **Xinyi Li**, Jingfu Bao, Yulin Huang, Benfeng Zhang, Gongbin Tang, Tatsuya Omori and Ken-ya Hashimoto, "Use of double-raised-border structure for quality factor enhancement of type II piston mode FBAR", Microsystem Technologies, 2018, 24(7): 2991-2997.

5. **Xinyi Li**, Jingfu Bao, Yulin Huang, Benfeng Zhang, Tatsuya Omori and Ken-ya Hashimoto, "Traveling Wave Excitation Sources for FEM Analysis of Scattering in Acoustic Waveguide", Microsystem Technologies, 2019, [DOI:10.1007/s00542-018-4169-7].

6. **Xinyi Li**, Jingfu Bao, Luyan Qiu, Naoto Matsuoka, Tatsuya Omori and Ken-ya Hashimoto, "3D FEM Simulation of SAW Resonators Using Hierarchical Cascading Technique and General-Purpose Graphic Processing Unit", Japanese Journal of Applied Physics, 2019, 58(SG): SGGC05.

7. **Xinyi Li**, Jingfu Bao, Yulin Huang, Benfeng Zhang, Tatsuya Omori and Ken-ya Hashimoto, "Use of Hierarchical Cascading Technique for FEM Analysis of Transverse Mode Behaviors in Surface Acoustic Wave Devices", IEEE Transactions on Ultrasonics, Ferroelectrics, and Frequency Control, 2019, [under review].

Scientific journals - co-author

1. Yulin Huang, **Xinyi Li**, Jingfu Bao, Di Deng, Yiling Wang and Yijia Du, "A 1.7-2.7-GHz 4-bit Phase shifter based on packaged RF MEMS switches", Journal of ElEctromagnEtic WavEs and applications, 2016, 30(5): 553-565.

2. Yulin Huang, **Xinyi Li**, Jingfu Bao, Xinghai Zhao, Yingbin Zheng, Yijia Du and Yiling Wang, "A WR-3 dual-band bandpass filter based on parallel coupling structure", Microsystem Technologies, 2017, 23(7): 2553-2559.

3. Yulin Huang, Jingfu Bao, **Xinyi Li**, Benfeng Zhang, Gongbin Tang, Tatsuya Omori and Ken-ya Hashimoto, "Influence of Coupling between Rayleigh and SH SAWs on Rotated Y-cut $LiNbO_3$ to Their Propagations", IEEE Transactions on Ultrasonics, Ferroelectrics, and Frequency Control, 2018, 65: 1905-1913.

4. Benfeng Zhang, Tao Han, **Xinyi Li**, Yulin Huang, Tatsuya Omori and Ken-ya Hashimoto, "Model parameter extraction of lateral propagating surface acoustic waves with coupling on SiO_2/grating/$LiNbO_3$ structure", Japanese Journal of Applied Physics, 2018, 57(7S1): 07LD04.

5. Yulin Huang, Jingfu Bao, **Xinyi Li**, Benfeng Zhang, Tatsuya Omori and Ken-ya Hashimoto, "Parameter extraction of coupling-of-modes equations including coupling between two surface acoustic waves on SiO_2/Cu/$LiNbO_3$ structures", Japanese Journal of Applied Physics, 2018, 57(7S1): 07LD13.

6. Feihong Bao, Leilei Bao, **Xinyi Li**, Muhammad Ammar Khan, Huaye Wu, Feng Qin, Ting Zhang, Yi Zhang, Jingfu Bao and Xiaosheng Zhang, "Multi-stage phononic crystal structure for anchor-loss reduction of thin-film piezoelectric-on-silicon microelectromechanical-system resonator", Applied Physics Express, 2018, 11(6): 067201.

7. Qiuping Wang, Jingfu Bao, Yuan Ling annd **Xinyi Li**, "Design of a novel RF MEMS square resonator", Microsystem Technologies, 2015, 21(8): 1805-1810.

8. Benfeng Zhang, Tao Han, Gongbin Tang, **Xinyi Li**, Yulin Huang, Tatsuya Omori and Ken-ya Hashimoto, "Impact of Coupling Between Multiple SAW Modes on Piston Mode Operation of SAW Resonators", IEEE transactions on ultrasonics, ferroelectrics, and frequency control, 2018, 65(6): 1062-1068.

9. Feihong Bao, Leilei Bao, Xiaosheng Zhang, Chao, Zhang, **Xinyi Li** and Jingfu Bao, "Frame structure for thin-film piezoelectric-on-silicon resonator to greatly enhance quality factor and suppress spurious modes", Sensors and Actuators A: Physical, 2018, 274: 101-108.

10. Luyan Qiu, **Xinyi Li**, Tatsuya Omori and Ken-ya Hashimoto, "Impact of Transverse Mode Resonances on Second Harmonic (H2) Generation in RF BAW Structures", Japanese Journal of Applied Physics, 2019, [to be published].

11. Naoto Matsuoka, Luyan Qiu, **Xinyi Li**, Tatsuya Omori and Ken-ya Hashimoto, "Applicability of Single Precision GPU for Fast 2D FEM Simulation of SAW Devices Using Hierarchical Cascading Technique", Japanese Journal of Applied Physics, 2019, [to be published].

12. Yulin Huang, Jingfu Bao, **Xinyi Li**, Benfeng Zhang, Luyan Qiu, Tatsuya Omori and Ken-ya Hashimoto, "Analysis of SAW Scattering with Discontinuous Periodic Gratings Using Travelling Wave Excitation and Hierarchical Cascading Technique", Transactions on Ultrasonics, Ferroelectrics, and Frequency Control, 2019, [DOI:10.1109/TUFFC.2019.2911133].

Conference proceedings - first author

1. **Xinyi Li**, Jingfu Bao and Feihong Bao, "A design of TPoS resonator with narrow tether", 11th Annual International Conference on Nano/Micro Engineered and Molecular System (NEMS), 2016, pp.446-449.

2. **Xinyi Li**, Jingfu Bao, Benfeng Zhang, Gongbin Tang, Tatsuya Omori and Ken-ya Hashimoto, "Use of Double-Raised-Border Structure for Quality Factor Enhancement of Type II Piston Mode FBAR", 2017 Joint Conference of the European Frequency Control Symposium and IEEE International Frequency Control Symposium (EFTF/IFCS), 2017, pp.547-550.

3. **Xinyi Li**, Jingfu Bao, Yulin Huang, Benfeng Zhang, Gonbin Tang, Tatsuya Omori and Ken-ya Hashimoto, "Use of Double-Raised-Border Structure for Quality Factor Enhancement of Type II Piston Mode FBAR", The 149th Technical Report of the 150th committee of the JSPS, 2017, pp.19-22.

4. **Xinyi Li**, Jingfu Bao, Yulin Huang, Benfeng Zhang, Tatsuya Omori and Ken-ya Hashimoto, "Traveling Wave Excitation for FEM Simulation of RF SAW/BAW Devices", 2017 IEEE International Ultrasonics Symposium (IUS), 2017,

   [DOI:10.1109/ULTSYM.2017.8092845],

5. **Xinyi Li**, Jingfu Bao, Yulin Huang, Benfeng Zhang, Tatsuya Omori and Ken-ya Hashimoto, "Application of Hierarchical Cascading Technique to FEM Simulation in BAW Devices to FEM Simulation in BAW Devices", Proceedings 38th Symposium on Ultrasonics Electronics, 2017, 2E2-2.

6. **Xinyi Li**, Jingfu Bao and Ken-ya Hashimoto, "Application of Hierarchical Cascading Technique to FEM Simulation of SAW/BAW Devices", The 151th Technical Report of the 150th committee of the JSPS, 2018, pp.1-5.

7. **Xinyi Li**, Jingfu Bao and Ken-ya Hashimoto, "Application of Hierarchical Cascading Technique to FEM Simulation of SAW/BAW Devices", "圧電材料デバイスシンポジウム, 2018, pp.53-56.

8. **Xinyi Li**, Jingfu Bao, Tatsuya Omori and Ken-ya Hashimoto, "Application of Hierarchical Cascading Technique to FEM Simulation of SAW/BAW Devices", Seventh International Symposium on Acoustic Wave Devices for Future Mobile Communication Systems, 2018, pp.47-51.

9. **Xinyi Li**, Jingfu Bao, Yulin Huang, Benfeng Zhang, Tatsuya Omori and Ken-ya Hashimoto, "Use of Hierarchical Cascading Technique for FEM Analysis of Transverse Mode Behaviors in Surface Acoustic Wave Devices", 2018 IEEE International Ultrasonics Symposium (IUS), 2018, (**Student paper competition finalist**) [DOI:10.1109/ULTSYM.2018.8580048].

10. **Xinyi Li**, Jingfu Bao and Ken-ya Hashimoto, "Use of Hierarchical Cascading Technique for FEM Analysis of Transverse Mode Behaviors in SAW Devices", The 154th Technical Report of the 150th committee of the JSPS, 2018, pp.23-26.

11. **Xinyi Li**, Jingfu Bao, Luyan Qiu, Naoto Matsuoka, Tatsuya Omori and Ken-ya Hashimoto, "GPGPU Based 3D FEM Simulation of SAW Resonators Using Hierarchical Cascading Technique", Proceedings 39th Symposium on Ultrasonics Electronics, 2018, 2E2-2 (**Young Scientist Award**).

12. **Xinyi Li**, Jingfu Bao, Luyan Qiu, Naoto Matsuoka, Tatsuya Omori and Ken-ya Hashimoto, "GPGPU Based 3D FEM Simulation of SAW Resonators Using Hierarchical Cascading Technique", The 155th Technical Report of the 150th committee of the JSPS, 2019, pp.27-30.

Conference proceedings - co-author

1. Ken-ya Hashimoto, **Xinyi Li** and Jingfu Bao, "Perturbation analysis of nonlinear signal generation in radio frequency bulk acoustic wave resonators", 2017 Joint Conference of the European Frequency Control Symposium and IEEE International Frequency Control Symposium (EFTF/IFCS), 2017, pp.538-541.

2. Ken-ya Hashimoto, **Xinyi Li** and Jingfu Bao, "Perturbation Analysis of Nonlinear Signal Generation in Radio Frequency Bulk Acoustic Wave Resonators", The 149th Technical Report of the 150th committee of the JSPS, 2017, pp.23-26.

3. Ken-ya Hashimoto, **Xinyi Li**, Jingfu Bao, Yulin Huang, Benfeng Zhang and Tao Han, "Transverse Modes in Temperature Compensated Surface Acoustic Wave Devices", 2018 IEEE International Ultrasonics Symposium (IUS), 2018,

   [DOI:10.1109/ULTSYM.2018.8580001].

4. Ken-ya Hashimoto, **Xinyi Li**, Jingfu Bao, Yulin Huang, Benfeng Zhang and Tao Han, "SAW/BAWデバイスの波動論的解析に関する最近の話題", 圧電材料デバイスシンポジウム, 2018, pp.61-64.

5. Luyan Qiu, **Xinyi Li**, Tatsuya Omori and Ken-ya Hashimoto, "Impact of Transverse Mode Resonances on Second Harmonic (H2) Generation in RF BAW Structures", Proceedings 39th Symposium on Ultrasonics Electronics, 2018, 3P3-9.

6. Ken-ya Hashimoto, **Xinyi Li**, Luyan Qiu and Tatsuya Omori, "質量ばねモデルによる厚み共振子の非線形特性解析", , The 155th Technical Report of the 150th committee of the JSPS, 2019, pp.31-36.

7. Ken-ya Hashimoto, **Xinyi Li**, Luyan Qiu and Tatsuya Omori, "Perturbation Analysis of Nonlinearity in Thickness Resonators Using Mass-Spring Model", 圧電材料デバイスシンポジウム, 2019, pp.59-64.

8. Yulin Huang, Jingfu Bao, **Xinyi Li**, Yiling Wang and Yijia Du, "A 4-bit switched-line phase shifter based on MEMS switches", 10th Annual International Conference on Nano/Micro Egnineered and Molecular System (NEMS), 2015, pp.405-408.

9. Yulin Huang, Jingfu Bao, **Xinyi Li**, Benfeng Zhang, Gongbin Tang, Tatsuya Omori and Ken-ya Hashimoto, "Influence of Coupling Between Rayleigh and SH SAWs on Rotated Y-Cut $LiNbO_3$ to Their Electromechanical Coupling Factor", 2017 IEEE International Ultrasonics Symposium (IUS), 2017,

   [DOI:10.1109/ULTSYM.2017.8092561].

10. Benfeng Zhang, Tao Han, **Xinyi Li**, Yulin Huang, Tatsuya Omori and Ken-ya Hashimoto, "Model Parameter Extraction of Lateral Propagating SAWs with Mode Coupling on TC-SAW Resonators", Proceedings 38th Symposium on Ultrasonics Electronics, 2017, 1P3-3.

11. Yulin Huang, Jingfu Bao, **Xinyi Li**, Benfeng Zhang, Tatsuya Omori and Ken-ya Hashimoto, "Parameter Extraction of COM Equations Including Two SAW Coupling for TC-SAW Structures", Proceedings 38th Symposium on Ultrasonics Electronics, 2017, 1P3-4.

12. Yi Zhang, Jingfu Bao, **Xinyi Li**, Feng Qin, Muhammad Ammar Khan, Ken-ya Hashimoto and Xiaosheng Zhang, "A 6-Degree-of-Freedom Piezoelectric Vibration Microstage with Reduced Cross-Axis Coupling", 2018 IEEE International Ultrasonics Symposium (IUS), 2018, [DOI:10.1109/ULTSYM.2018.8579975].

13. Yulin Huang, Jingfu Bao **Xinyi Li**, Benfeng Zhang, Luyan Qiu, Tatsuya Omori and Ken-ya Hashimoto, "Analysis of SAW Scattering at Discontinuity Between Periodic Gratings Using Travelling Wave Excitation and Hierarchical Cascading Technique", 2018 IEEE International Ultrasonics Symposium (IUS), 2018,

    [DOI:10.1109/ULTSYM.2018.8580141].

14. Naoto Matsuoka, Luyan Qiu, **Xinyi Li**, Tatsuya Omori and Ken-ya Hashimoto, "Applicability of Single Precision GPU for Fast 2D FEM Simulation of SAW Devices Using Hierarchical Cascading Technique", Proceedings 39th Symposium on Ultrasonics Electronics, 2018, 3P3-10.

15. Benfeng Zhang, Tao Han, **Xinyi Li**, Yulin Huang, Tatsuya Omori and Ken-ya Hashimoto, "FEM-Based Estimation of SAW Power Flow Angle in Periodic Gratings", 2018 IEEE International Ultrasonics Symposium (IUS), 2018, [DOI:10.1109/ULTSYM.2018.8579965].

16. Feihong Bao, Mohammed Awad, **Xinyi Li**, Zhaohui Wu, Jingfu Bao, Xiaosheng Zhang and Leilei Bao, "Suspended Frame Structure with Phononic Crystals for Anchor Loss Reduction of MEMS Resonator", 2018 IEEE International Frequency Control Symposium (IFCS), 2018, [DOI:10.1109/FCS.2018.8597503].

17. Benfeng Zhang, Tao Han, Gongbin Tang, **Xinyi Li**, Yulin Huang, Tatsuya Omori and Ken-ya Hashimoto, "Impact of Coupling Between Multiple SAW Modes on Piston Mode Operation of SAW Resonators", 2017 IEEE International Ultrasonics Symposium (IUS), 2017, [DOI:10.1109/ULTSYM.2017.8092109].

18. Feihong Bao, Leilei Bao, Xin Zhou, **Xinyi Li**, Jingfu Bao and Xiaosheng Zhang, "High-Q Multiple-frequency Ring-shaped thin-film Piezoelectric-on-silicon Resonators", 2018 International Conference on Microwave and Millimeter Wave Technology (ICMMT), 2018, [DOI:10.1109/ICMMT.2018.8563655].

19. Ken-ya Hashimoto, Benfeng Zhang, Tao Han, Yulin Huang, **Xinyi Li**, Jingfu Bao and Tatsuya Omori, "Impact of Two SAW Coupling in Temperature Compensated SAW Structure", Seventh International Symposium on Acoustic Wave Devices for Future Mobile Communication Systems, 2018, pp.52-57.

20. Feihong Bao, Jingfu Bao, **Xinyi Li**, Xin Zhou, Yamei Song and Xiaosheng Zhang, "Reflective Strategy Based on Tether-Integrated Phononic Crystals for 10 MHz MEMS Resonator", 2019 Joint Conference of the European Frequency Control Symposium and IEEE International Frequency Control Symposium (EFTF/IFCS), 2019 (accepted).